KTH Information and
Communication Technology

Pulse Shape Adaptation and Channel Estimation in Generalised Frequency Division Multiplexing Systems

JINFENG DU

Licentiate Thesis in
Electronics and Computer Systems
Stockholm, Sweden 2008

TRITA-ICT-COS-0803
ISSN 1653-6347
ISRN KTH/COS/R--08/03--SE
ISBN 978-91-7415-187-9

KTH School of Information and
Communication Technology
SE-164 40 Stockholm
SWEDEN

Akademisk avhandling som med tillstånd av Kungl Tekniska högskolan framlägges till offentlig granskning för avläggande av teknologie Licentiatexamen i Elektronik och Datorsystem torsdagen den 11 December 2008 klockan 13.00 i sal E, Forum IT-Universitetet, Kungl Tekniska Högskolan, Isajordsgatan 39, Kista.

Tryck: Universitetsservice US AB

Abstract

Orthogonal Frequency Division Multiplexing (OFDM) is well known as an efficient technology for wireless communications and is widely used in many of the current and upcoming wireless and wireline communication standards. However, it has some intrinsic drawbacks, e.g., sensitivity to the inter-carrier interference (ICI) and high peak-to-average power ratio (PAPR). Additionally, the cyclic prefix (CP) is not spectrum efficient and fails when the channel delay spread exceeds the length of CP, which will result in inter-symbol interference (ISI). In order to combat or alleviate these drawbacks various techniques have been proposed, which can be categorised into two main classes: techniques that keep the structure of OFDM and meanwhile increase the system robustness or re-organise the symbol streams on each sub-carrier, and techniques that increase the ISI/ICI immunity by adopting well designed pulse shapes and/or resorting to general system lattices. The latter class are coined as Generalised FDM (GFDM) throughout this thesis to distinguish with the former class.

To enable seamless handover and efficient usage of spectrum and energy, GFDM is expected to dynamically adopt pulse shapes that are optimal in doubly (time and frequency) dispersive fading channels. This is however not an easy task as the method of optimal pulse shape adaptation is still unclear, let alone efficient implementation methods. Besides, performance of GFDM highly depends on the channel estimation quality, which is not straightforward in GFDM systems.

This thesis addresses, among many other aspects of GFDM systems, measures of the time frequency localisation (TFL) property, pulse shape adaptation strategy, performance evaluation and channel estimation. We first provide a comparative study of state-of-the-art GFDM technologies and a brief overview of the TFL functions and parameters which will be used frequently in later analysis and discussion. A framework for GFDM pulse shape optimisation is formulated targeting at minimising the combined ISI/ICI over doubly dispersive channels. We also propose a practical adaptation strategy utilising the extended Gaussian functions (EGF) and discuss the trade-off between performance and complexity. One realisation under the umbrella of GFDM, namely OFDM/OQAM, is intensively studied and an efficient implementation method by direct discretisation of the continuous time model has been proposed. Besides, a theoretical framework for a novel preamble-based channel estimation method has been presented and a new preamble sequence with higher gain is identified. Under the framework, an optimal pulse shape dependent preamble structure together with a suboptimal but pulse shape independent preamble structure have been proposed and evaluated in the context of OFDM/OQAM.

Keywords: OFDM, GFDM, OQAM, pulse shaping, adaptation, channel estimation.

Acknowledgments

The work presented in this thesis was conducted during my Ph.D. study at Department of Electronic, Computer, and Software Systems and Department of Communication Systems in the School of Information and Communication Technology at the Royal Institute of Technology (KTH), Sweden during the years 2006–2008. I would like to take this opportunity to acknowledge all the people who have supported me.

First and foremost, I would like to express my sincere gratitude to my main supervisor Docent Svante Signell, for giving me a chance to be a graduate student and leading me into this interesting and challenging research topic, for his supervision, guidance and continuous encouragement. I greatly appreciate his generosity in sharing his expertise and time in our frequent discussions which always help to clarify my thoughts and inspire me with new ideas. I owe many thanks to my co-supervisor Prof. Ben Slimane for the inspiring discussions through the courses and seminars, and for his great efforts on the quality check of this thesis.

I would also like to thank all my current and former colleagues at CoS and ECS for the pleasant and warm atmosphere. It has been great to be working here. I really appreciate the Friday seminars at RST group which have given me a unique opportunity to deepen my understanding and broaden my perspective of research. Especially, I want to express my appreciation to PhD student Jinliang Huang for all the inspiring discussions and suggestions in the work. Thanks to all the administrators and the systems group for their excellent work, with special thanks to Ulla-Lena Eriksson and Irina Radulescu for their kindness and amazing efficiency.

Many thanks to Wireless@KTH for supporting me through the small projects NGFDM and DSAER.

I'm indebted to all my Chinese colleagues at KTH and friends in Sweden, without them, life would not be as colourful as what it is today.

My parents and my girl friend Feifan, who have given me unconditional support and endless love, deserve the warmest thanks.

Last but not the least, I want to thank Prof. Arne Svensson who acts as the opponent on this thesis.

List of Abbreviations

ACM	Association for Computing Machinery
AWGN	Additive White Gaussian Noise
BER	Bit Error Rate
BPSK	Binary Phase Shift Keying
CP	Cyclic Prefix
CSI	Channel State Information
DAB	Digital Audio Broadcasting
DFT	Discrete Fourier Transform
DVB-T	Digital Video Broadcasting - Terrestrial
DVB-H	Digital Video Broadcasting - Handheld
EGF	Extended Gaussian Functions
FDE	Frequency Domain Equaliser
FDM	Frequency Division Multiplexing
FFT	Fast Fourier Transform
GFDM	Generalised FDM
IAM	Interference Approximation Method
IDFT	Inverse Discrete Fourier Transform
IEEE	Institute of electrical and Electronics Engineers
IFFT	Inverse Fast Fourier Transform
i.i.d	Independent and Identically Distributed
ISI	Inter-Symbol Interference
ICI	Inter-Carrier Interference
IOTA	Isotropic Orthogonal Transfer Algorithm
LTE	Long Term Evolution
MAP	Maximum a Posteriori
MIMO	Multiple-Input Multiple-Output
ML	Maximum Likelihood
MMSE	Minimum Mean Square Error
M-QAM	M-ary Quadrature Amplitude Modulation
OFDM	Orthogonal Frequency Division Multiplexing
OQAM	Offset Quadrature Amplitude Modulation
PAPR	Peak to Average Power Ratio
PLC	Power Line Communication

RMS	Root Mean Square
RRC	Root Raised Cosine
SER	Symbol Error Rate
SNR	Signal to Noise Ratio
TFL	Time Frequency Localization
UWB	Ultra Wideband
VDSL	Very high-rate Digital Subscriber Line
WCDMA	Wideband Code Division Multiple Access
WiMAX	Worldwide Interoperability for Microwave Access
WLAN	Wireless Local Area Network
WRAN	Wireless Regional Area Network
WSSUS	Wide Sense Stationary Uncorrelated Scattering

List of Figures

Contents

Chapter 1

Introduction

1.1 Background

Motivation

The fast development in wireless communications for the past two decades has been driven by service demands for higher and higher data rates. For instance, the required peak data rate for IMT-advanced, will reach 100Mbit/s for high mobility applications and 1Gbit/s for low mobility applications. Stringent requirement has been put on spectral efficiency and the problem is further aggravated by scarce bandwidth. On the other hand, it is becoming more and more necessary to provide "ubiquitous" connectivity to end users so that they can always get connected via heterogeneous access techniques. Therefore, it is desirable to develop technologies with affordable complexity that facilitates seamless handover among different standards in various radio environments: indoor or outdoor, in urban- sub-urban or rural areas. In this thesis we study essential parts of a system that have the potential to fulfill these requirements.

As a key technology, Orthogonal Frequency Division Multiplexing (OFDM) has been shown to be very efficient in wireless and wireline communication over broadband channels. By partitioning the wideband channel into a large number of parallel narrow band sub-channels, the task of high data rate transmission over a frequency selective channel has been transformed into number of parallel low data rate transmissions which do not require complicated equalization techniques. The efficient OFDM implementation method based on FFT and the rapid evolution in the silicon industry has promoted OFDM to be adopted in many current applications and upcoming standards, e.g., VDSL, power-line communication (PLC), DAB, DVB-T/H, WLAN (IEEE 802.11a/g), WRAN (IEEE 802.22), WiMAX (IEEE 802.16), 3G LTE and others as well as the 4G wireless standards, since next generation wireless systems will be fully or partially OFDM-based.

By using a cyclic prefix (CP), OFDM is very robust against inter-symbol interference (ISI) which is caused by the multipath propagation. With a varying

channel characteristic, however, this approach is not optimal. For example the CP approach is effective only for channels with smaller delay spread than the duration of CP. When delay spread exceeds the length of the CP, considerable ISI will be introduced. Actually, the classic FFT-based OFDM receiver can be treated as a matched filter bank, matched to the transmitter waveforms derived from the IFFT, which in the frequency domain is a sinc function ($\sin(x)/x$). The sinc function, however, is only optimal in AWGN channels and therefore makes OFDM very sensitive to inter-carrier interference (ICI) which mainly arises from frequency dispersion. Besides, the high peak-to-average power ratio (PAPR) OFDM signal demands high linearity of the power amplifier and therefore causes an increase of the hardware cost and power consumption. An extra cost in power and spectrum is incurred by using the CP. Therefore new schemes which can inherit the advantage of OFDM but avoid the inherent drawbacks will be of great interest.

The joint ISI/ICI interference within an FDM system over dispersive channels depends on two factors:

A Decay property of out-of-band energy for signal pulses

B Distance between adjacent symbols in time and frequency

Here a lattice point (m, n) on the time-frequency plane indicates a place where a data symbol is transmitted on the mth frequency carrier during the nth time slot. Signal pulses with faster decay of out-of-band energy means smaller side lobe amplitude and hence smaller power/interference leakage. Larger distance among neighbouring time-frequency lattice points also means smaller interference from and to adjacent symbols. A natural solution is therefore to utilise well designed pulse shapes will fast decay property and advanced lattice structure to increase the distance among adjacent lattice points, as we will see later.

Previous work

On one hand, some improvements for OFDM have been reported to combat frequency dispersion sensitivity by exploiting ICI self-cancellation methods [1] or to explore space and time diversity in dispersive channels through fractional sampling [2]. And numerous research efforts have been spent on PAPR reduction techniques[1]. The usage of CP, however, is retained to combat ISI in such techniques which aim to enhance OFDM. All the above techniques will be categorised as CP-OFDM in the following.

On the other hand, Various pulse shapes [3–8] well localised in the time frequency plane have been studied in the past few years. A frame work of orthogonalization methods has been proposed to construct orthogonal functions based on the Gaussian function [5, 6] and a combination of Hermite functions [8], respectively.

[1] Too many contributions on PAPR reduction to be listed here

Such orthogonalised pulse shapes, with a smaller lattice density ($\sigma = \frac{1}{TF} < 1$), ensure orthogonality among analysis basis and among synthesis basis and therefore enable simple signal detection and optimal in AWGN channel. As the orthogonality among different pair of analysis-synthesis basis is sufficient for perfect reconstruction in AWGN channels, more degrees of freedom in pulse shapes design have been introduced by using different analysis and synthesis prototype functions, as reported in) [9–11]. OFDM with offset QAM (OFDM/OQAM) [12, 13] which transmits real symbols with double lattice density has shown some advantages over OFDM, but faces difficulties of channel estimation and equalization. General system lattice grids rather than the rectangular one used in OFDM have also been proposed [14], which increases the distance between neighbouring lattice points without reducing the lattice density. Further improvements [15], at the cost of detection complexity, can be achieved by using Gaussian pulses and a hexagonal lattice which is composed by superposition of two rectangular lattices.

The class of the aforementioned multi-carrier techniques which utilise well designed pulse shapes and/or general time-frequency lattice, are coined with all other alike methods as Generalised FDM (GFDM) in the remaining part of this thesis to distinguish with techniques that support or enhance CP-OFDM.

GFDM and pulse shape adaptation

GFDM is of great interest as it has shown promising advantages over CP-OFDM on robustness to both time and frequency dispersion. The CP is avoided in GFDM by using optimally time-frequency localised (TFL) pulse shapes, and hence a theoretically higher power and spectrum efficiency can be achieved. Techniques designed for enhancing CP-OFDM can also be extended to GFDM without difficulties. Furthermore, it is advantageous to design a multiple access technology based on GFDM technology since GFDMA would be able to support heterogeneous access networks that are OFDM-based, e.g. 3G-LTE, WRAN, WiMAX, etc., due to the similarities between GFDM and OFDM.

Unlike OFDM that uses rectangular pulse shapes, which is only optimal with respect to an AWGN channel, GFDM is expected to dynamically adopt channel-dependent pulse shapes that are optimal in doubly dispersive fading channels. The idea of the optimal pulse-shaping is to tailor the well designed signal waveforms for transmitter and receiver to fit the current channel condition. For example, in indoor situations where time dispersion is usually small, a vertically stretched time-frequency pulse is suitable and where the frequency dispersion is small, a horizontally stretched pulse is suitable. This enables a very efficient packing of time-frequency symbols maximizing e.g. the throughput or the interference robustness in the communication link.

Adapting the transmitter and receiver pulse shapes dynamically to the current channel conditions and interference environments will consequently provide the possibility to move seamlessly between different channels like indoor, outdoor,

rural, suburban, urban, etc. It also achieves a higher spectral efficiency with lower transmit power by avoiding CP. In addition, the reduced out-of-band energy (i.e., lower side lobes) promotes higher ICI robustness and allows a larger number of subcarriers to be used while still respecting a prescribed spectral mask. **This lower side lobe in GFDM also allows a more efficient usage of the spectrum compared with OFDM, which usually needs a 10% guard band to meet the spectrum mask [16].** Besides, the high PAPR problem in OFDM can also be alleviated to some extend in GFDM systems. These advantages of GFDM implies the potential to utilise energy and spectrum in a more efficient way.

However, there are only a few research activities in the area of GFDM up to now. Most of the aforementioned work just emphasize the extreme of one requirement while ignoring all the others, which undermines their claimed benefits and usually sets themselves far away from practical implementation. Therefore it is necessary to find a balanced solution. Channel estimation, which is assumed to be perfect at least on the receiver side in most of the previous work, turns to be not an easy task in some GFDM systems [9, 13, 15] where intrinsic interference was introduced to allow more design freedom. The goal of this thesis project is to design energy and spectrum efficient GFDM systems with better interference immunity at the cost of small additional complexity. We believe that new progress in GFDM technologies will be an enabler for "intelligent" systems [17] and a potential contribution to the evolution of the next generation wireless communication technologies.

1.2 Contributions and outline

This thesis addresses, among many other aspects of GFDM systems, the measures of time frequency localisation (TFL) property, pulse shape adaptation strategy, performance evaluation and channel estimation. Our research results have been reported in several (published and submitted) conference papers, non-reviewed conference papers, a technical report, as well as invited presentations in a few places. A journal paper is being prepared for submission. This dissertation is divided into six chapters, with detailed description of contributions in each chapter listed as follows.

Chapter 2

In this chapter we first present the baseband signal models as well as the channel models for both OFDM and GFDM systems. Then a comprehensive review of OFDM and a comparative study of state-of-the-art GFDM technologies is carried out, followed by a brief overview of the TFL functions and parameters which will be used frequently in later analysis and discussion. Various prototype functions, such as rectangular, half cosine, root raised cosine (RRC), Isotropic Orthogonal Transfer Algorithm (IOTA) function and Extended Gaussian Functions (EGF) are discussed and simulation results are provided to illustrate the TFL properties by the ambiguity function and the interference function.

Part of the material was summarised in

> Jinfeng Du and Svante Signell, "Classic OFDM Systems and Pulse Shaping OFDM/OQAM Systems," *Technical Report of the NGFDM Project*, Royal Institute of Technology, Stockholm, Sweden, February 2007.

Chapter 3

This chapter formulates a general framework for pulse shape optimisation targeting at minimising the combined ISI/ICI over doubly dispersive channels. A practical adaptation strategy with focus on the EGF function, which is shown to have very nice TFL properties suitable for pulse shape adaptation has been proposed and the trade-off between performance and complexity has been discussed.

The results on pulse shape adaptation in OFDM/OQAM systems was published in

> Jinfeng Du and Svante Signell, "Pulse Shape Adaptivity in OFDM/OQAM Systems over Dispersive Channels," in Proc. of *ACM International Conference on Advanced Infocom Technology (ICAIT)*, Shenzhen, China, July 2008.

The nice TFL property of EGF functions was summarised in

> Jinfeng Du and Svante Signell, "Time Frequency Localisation Properties of the Extended Gaussian Functions," *manuscript*, in preparation for submission as a short letter.

Chapter 4

In this chapter an intensive study of OFDM/OQAM is presented and efficient implementation of OFDM/OQAM with aforementioned pulse shapes are done in the Matlab/Octave simulation workbench for software defined radio (SDR-WB) [18,19] by direct discretisation of the continuous time model, which achieves near perfect reconstruction in the absence of a channel for well designed pulse shapes.

The contribution on efficient implementation and reconstruction evaluation was published in

> Jinfeng Du and Svante Signell, "Time Frequency Localization of Pulse Shaping Filters in OFDM/OQAM Systems," in Proc. of *IEEE International Conference on Information, Communications and Signal Processing (ICICS)*, Singapore, December 2007.

The comparison of CP-OFDM and OFDM/OQAM performance in dispersive channels, by investigating the signal reconstruction perfectness, time and frequency dispersion robustness, and sensitivity to frequency offset, was published in

> Jinfeng Du and Svante Signell, "Comparison of CP-OFDM and OFDM/OQAM in Doubly Dispersive Channels," in Proc. of *IEEE Future Generation Communication and Networking (FGCN)*, volume 2, Jeju Island, Korea, December 2007.

Chapter 5

Based on previous work, a theoretical framework for novel preamble-based channel estimation methods has been presented in this chapter and a new preamble sequence with higher gain has been proposed based on this framework. Most of the contributions were submitted to

> Jinfeng Du and Svante Signell, "Novel Preamble-Based Channel Estimation for OFDM/OQAM Systems," submitted to IEEE International Conference on Communication (ICC) 2009.

Under the framework, an optimal pulse shape dependent preamble structure has been derived and a suboptimal but pulse shape independent preamble structure has been proposed and evaluated. Contributions in this chapter were summarised in

> Jinfeng Du and Svante Signell, "Optimal Preamble Design for Channel Estimation in OFDM/OQAM Systems," *manuscript*, in preparation for submission to a journal.

Chapter 6

The concluding chapter summarises this dissertation and points out several open topics for future work.

1.3 Notations

Throughout this thesis the following notational conventions are used:

x	lowercase letters denote random variables.
X	uppercase letters denote matrices.
x_n	The nth realization of the random variable x.
$x_{m,n}$, $x(m,n)$	The $(i,\ j)$th element of the matrix X.
j	j = sqrt(-1).
E_b	energy per bit.
E_s	energy per symbol.
N_0	mono-lateral noise density.
$h(\tau,t)$	channel impulse response at time slot t.
$H(f,t)$	channel frequency response at time slot t.
$H(\tau,\nu)$	channel Doppler spectrum.
$S_h(\tau,\nu)$	channel scattering function.
T_d	channel delay spread.
τ_{RMS}	channel RMS delay spread.
B_d	channel Doppler spread.
f_D	maximum Doppler shift.

ξ	Heisenberg parameter.
κ	Direction parameter.
F_s	sampling frequency.
T_s	sampling interval ($T_s = 1/F_s$).
F	OFDM sub-carrier frequency separation.
T	OFDM symbol duration without CP.
T_{cp}	duration of CP.
$\mathrm{E}[x]$	the expected value of random variable x.
$\Re(\cdot)$	take the real part of a complex number.
$\Im(\cdot)$	take the imaginary part of a complex number.
$\delta(\cdot)$	the Dirac delta function.
$\log(\cdot)$	the log operator.
$\log_2(\cdot)$	the log operator with base 2.
$\sin(\cdot)$	the sine function.
$\cos(\cdot)$	the cosine function.
$\tan(\cdot)$	the tangent function.
$\cot(\cdot)$	the cotangent function.
$\mathrm{atan}(\cdot)$	the inverse tangent function.
$\mathrm{acot}(\cdot)$	the inverse cotangent function.

Chapter 2

Overview of GFDM and Time Frequency Localization

2.1 System- and channel model

In FDM systems, as shown in Fig. 2.1, the information bit stream (bit rate $R_b = \frac{1}{T_b}$) is first modulated in baseband using M-QAM modulation (with symbol duration $T_s = T_b \log_2 M$) and then divided into N parallel symbol streams which are multiplied by a pulse shape function $g_{m,n}(t)$. These N parallel signals are then summed up and transmitted. On the receiver side, the received signal is first passed through N parallel correlator demodulators (multiplication, integration and sampling) and merged together via parallel-to-serial converter followed by a detector and decoder.

The equivalent lowpass representation of the transmitted signal can be written in the following analytic form

$$s(t) = \sum_{m=0}^{N-1} \sum_{n=-\infty}^{\infty} a_{m,n} g_{m,n}(t) \tag{2.1}$$

where $a_{m,n} (m = 0, 1, ..., N-1, n \in \mathbb{Z})$ denotes the baseband modulated information symbol conveyed by the sub-carrier of index m during the symbol time of index n, and $g_{m,n}(t)$ represents the pulse shape of index (m, n) in the synthesis basis which is derived by the time-frequency translated version of the prototype function $g(t)$ in the way defined by different FDM schemes.

After passing through a doubly dispersive channel, the received signal can be written as

$$r(t) = \int h(\tau, t) s(t - \tau) d\tau + w(t) \tag{2.2}$$

where $h(\tau, t)$ is the impulse response of the linear time-variant channel, and $w(t)$ is noise which in the rest of this thesis is assumed to be additive white Gaussian

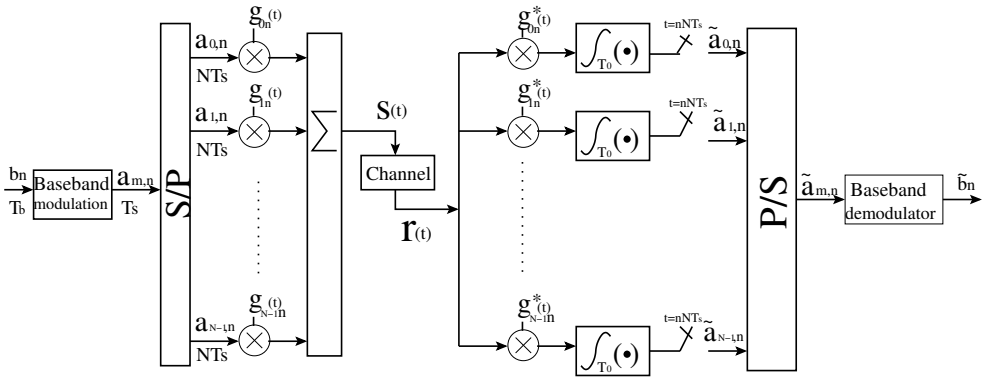

Figure 2.1: Block diagram of an FDM system (equivalent lowpass).

noise (AWGN) with mono-lateral noise density N_0. Note that the wireless channel can also be modeled as a linear device [20] whose input-output relation is defined by

$$r(t) = \int \hbar(\tau, t)s(\tau)d\tau + w(t) \tag{2.3}$$

By comparing (2.2) with (2.3), one can easily figure out that $h(\tau, t) = \hbar(t - \tau, t)$. From a physical point of view $\hbar(\tau, t)$ is the channel response at time t to a unit impulse input at time τ, and $h(\tau, t)$ on the other hand can be interpreted as the response at time t to a unit impulse response which arrives τ seconds earlier. [1]

By taking the Fourier transform of $h(\tau, t)$ with respect to t, we can get

$$H(\tau, \nu) \triangleq \int h(\tau, t)e^{-j2\pi\nu t}dt \quad \text{and} \quad h(\tau, t) = \int H(\tau, \nu)e^{j2\pi\nu t}d\nu \tag{2.4}$$

where $j = \sqrt{-1}$. Then (2.2) can be rewritten as

$$\begin{aligned} r(t) &= \iint H(\tau, \nu)s(t - \tau)e^{j2\pi\nu t}d\nu d\tau + w(t) \\ &= \sum_{m=0}^{N-1} \sum_{n=-\infty}^{\infty} \iint H(\tau, \nu)a_{m,n}g_{m,n}(t - \tau)e^{j2\pi\nu t}d\nu d\tau + w(t) \end{aligned} \tag{2.5}$$

The doubly dispersive channel is assumed to be wide sense stationary uncorrelated scattering (WSSUS) and therefore can be implemented by a tapped-delay-line Monte Carlo-based WSSUS channel model [21] with generic channel parameters. Apart from $h(\tau, t)$ itself and its Fourier transform $H(\tau, \nu)$, two other functions of

[1] For a more detailed discussion, please refer to [20].

the channel will be frequently used in our analysis and therefore listed in below. Following the similar notations as in [22], the two dimensional auto-correlation function of the impulse response (with respect to τ and ν) is defined as

$$\phi_h(\tau_1, \tau_2, t_1, t_2) \triangleq \mathrm{E}[h(\tau_1, t_1)h^*(\tau_2, t_2)] = \phi_h(\tau_1, t_1 - t_2)\delta(\tau_1 - \tau_2) \tag{2.6}$$

where $\delta(x)$ is the Dirac delta function and the the second equality comes from the property of the WSSUS channel: *wide sense stationary* ensures the auto-correlation is stationary (only depends on the time difference $t_1 - t_2$) and *uncorrelated scattering* indicates that one of the components of the received signal with delay τ_1 is uncorrelated with all other signal components with different delays (bring in the term $\delta(\tau_1 - \tau_2)$). By taking the Fourier transform of $\phi_h(\tau, \Delta t)$ with respect to Δt, we can get the famous *scattering function*

$$S_h(\tau, \nu) \triangleq \int \phi_h(\tau, \Delta t) e^{-j2\pi\nu\Delta t} d\Delta t \tag{2.7}$$

One important observation of the relationship between $H(\tau, \nu)$ and $S_h(\tau, \nu)$ shall be highlighted here. By taking the two dimensional autocorrelation function of $H(\tau, \nu)$, we get

$$\mathrm{E}[H(\tau_1, \nu_1)H^*(\tau_2, \nu_2)] = S_h(\tau_1, \nu_1)\delta(\tau_1 - \tau_2)\delta(\nu_1 - \nu_2) \tag{2.8}$$

The proof can be found in Appendix 2.6 A.

One of the most used WSSUS doubly dispersive channel, in which an exponential delay power profile and a U-shaped Doppler power spectrum [23] is assumed and therefore denoted exp-U in the following, is defined by its scattering function in the following way

$$S_h(\tau, \nu) = \frac{e^{-\frac{|\tau|}{\tau_{\mathrm{RMS}}}}}{\tau_{\mathrm{RMS}}} \frac{1}{\pi f_D \sqrt{1 - (\frac{\nu}{f_D})^2}} \quad \begin{matrix} \tau \in [0, T_d] \\ \nu \in [-f_D, f_D] \end{matrix} \tag{2.9}$$

where τ_{RMS} is the RMS delay spread and f_D is the maximum Doppler shift. In this case it can be confirmed that the RMS Doppler spread $f_{\mathrm{RMS}} = \frac{\sqrt{2}}{2} f_D$, see Appendix 2.6 B.

2.2 Overview of OFDM

The main idea behind OFDM is to partition the frequency selective fading channel (delay spread T_d is larger than symbol duration T_s) into a large number (say N) of parallel and mutually orthogonal sub-channels which are flat fading ($T_d << NT_s$) and thereafter transform a very high data rate ($\frac{1}{T_s}$) transmission into a set of parallel transmissions with very low data rates ($\frac{1}{NT_s}$). With this structure the

problem of high data rate transmission over frequency selective channels has been transformed into a set of simple problems which do not require complicated time domain equalization. Therefore OFDM plays an important role in modern wireless communication where high data rate transmission is commonly required.

Principles

In OFDM systems, $a_{m,n}(m = 0, 1, ..., N-1, n \in \mathbb{Z})$ denotes the complex-valued baseband modulated information symbol conveyed by the sub-carrier of index m during the symbol time of index n, and $g_{m,n}(t)$ represents the pulse shape of index (m, n) in the synthesis basis which is derived by the time-frequency translated version of the prototype function $g(t)$ in the following way

$$g_{m,n}(t) \triangleq e^{j2\pi mFt} g(t - nT) \tag{2.10}$$

where F represents the inter-carrier frequency spacing and T is the OFDM symbol duration. Therefore $g_{m,n}(t)$ forms an infinite set of time shifted pulses spaced at multiples of T and frequency modulated by multiples of F. Consequently the density of an OFDM system lattice is

$$\sigma = \frac{1}{TF} \tag{2.11}$$

In an OFDM system, the frequency spacing F and the time shift T are choose as follows to satisfy the orthogonality requirement

$$F = \frac{1}{NT_s} \qquad T = NT_s \tag{2.12}$$

The prototype function $g(t)$ is defined as follows

$$g(t) = \begin{cases} \frac{1}{\sqrt{T}}, & 0 \le t < T \\ 0, & \text{elsewhere} \end{cases} \tag{2.13}$$

Orthogonality of the synthesis basis can be demonstrated from the inner product between different elements

$$\begin{aligned} \langle g_{m,n}, g_{m',n'} \rangle &= \int_R g^*_{m,n}(t) g_{m',n'}(t) dt \\ &= \int_R e^{j2\pi(m'-m)Ft} g^*(t - nT) g(t - n'T) dt \\ &= \frac{1}{\sqrt{T}} \int_{nT}^{(n+1)T} e^{j2\pi(m'-m)Ft} g(t - n'T) dt \\ &= \delta_{m,m'} \delta_{n,n'} \end{aligned} \tag{2.14}$$

where the last equality comes from the fact that $TF = 1$ which is a requirement in OFDM system, and $\delta_{m,n}$ is the Kronecker delta function defined by

$$\delta_{m,n} = \begin{cases} 1, & m = n \\ 0, & \text{otherwise} \end{cases}$$

At the receiver side, the received signal $r(t)$ can be written as

$$r(t) = h * s(t) + n(t) = \sum_{n=-\infty}^{+\infty} \sum_{m=0}^{N-1} h_{m,n} a_{m,n} g_{m,n}(t) + w(t) \tag{2.15}$$

where h is the wireless channel impulse response, $h_{m,n}$ represents the complex-valued channel realization at the lattice point (mF, nT) which is assumed to be known by the receiver, and $w(t)$ is the AWGN noise. Passing $r(t)$ through N parallel correlator demodulators with analysis basis which is identical[2] with the synthesis basis defined by (2.10), the output of the l_{th} branch during time interval $nT \leq t < (n+1)T$ is

$$\begin{aligned} \tilde{a}_n(l) = \langle g_{l,n}, r \rangle &= \sum_{k=-\infty}^{+\infty} \sum_{m=0}^{N-1} h_{m,k} a_{m,k} \langle g_{l,n}, g_{m,k} \rangle + \langle g_{l,n}, w \rangle \\ &= \sum_{k=-\infty}^{+\infty} \sum_{m=0}^{N-1} h_{m,k} a_{m,k} \delta_{l,m} \delta_{n,k} + w_n(l) \\ &= \sum_{m=0}^{N-1} h_{m,n} a_{m,n} \delta_{l,m} + w_n(l) \\ &= h_{l,n} a_{l,n} + w_n(l) \end{aligned} \tag{2.16}$$

In the detector this output is multiplied by a factor $\dfrac{1}{h_{l,n}}$ (nothing but channel inversion) and therefore the transmitted symbol is recovered after demodulation with only presence of AWGN noise.

The spectral efficiency η in this OFDM system can be expressed as

$$\eta = \sigma \log_2 M = \frac{\log_2 M}{TF} = \log_2 M \text{ [bit/s/Hz]} \tag{2.17}$$

where $\log_2 M$ is the number of bits per symbol and $\sigma = \dfrac{1}{TF} = 1$ is the lattice density of OFDM system.

[2] not necessary, see OFDM with cyclic prefix in Sec. 2.2

Implementation

If we sample the transmitted signal $s(t)$ at rate $1/T_s$ during time interval $nT \leq t < (n+1)T$ and normalize it by $\sqrt{T}$, we obtain

$$\begin{aligned} s_n(k) \triangleq s(nT + kT_s) &= \sum_{m=0}^{N-1} a_{m,n} e^{j2\pi mFkT_s} \\ /\text{apply (2.12)}/ &= \sum_{m=0}^{N-1} a_{m,n} e^{j2\pi \frac{mk}{N}} \end{aligned} \quad , \begin{array}{l} k = 0, 1, ..., N-1 \\ n \in \mathbb{Z} \end{array} \tag{2.18}$$

This sampled transmitted signal $s_n(k)(n \in \mathbb{Z}, k = 0, 1, ..., N-1)$ is the Inverse Discrete Fourier Transform (IDFT)[3] of the modulated baseband symbols $a_{m,n}(n \in \mathbb{Z}, m = 0, 1, ..., N-1)$ during the same time interval. Therefore the OFDM modulator at the transmitter side can be replaced by an IDFT block.

Equivalently, at the receiver side, we sample the received signal $r(t)$ at the same sampling rate $1/T_s$, normalize it by factor $\sqrt{T}$, and rewrite (2.16) as follows

$$\begin{aligned} \tilde{a}_{m,n} = \langle g_{m,n}, r \rangle &= \int_{nT}^{(n+1)T} g^*_{m,n}(t) r(t) dt \\ \simeq \sum_{k=0}^{N-1} r(nT + kT_s) e^{-j2\pi \frac{mk}{N}} &= \sum_{k=0}^{N-1} r_n(k) e^{-j2\pi \frac{mk}{N}} \end{aligned}$$

The demodulated symbol $\tilde{a}_{m,n}(m = 0, 1, ..., N-1), n \in \mathbb{Z}$ is the Discrete Fourier Transform (DFT) of the received signal $r_n(k)(k = 0, 1, ..., N-1, n \in \mathbb{Z})$.

Let $\boldsymbol{s}_n = [s_n(0), s_n(1), ..., s_n(N-1)]^T$, $\boldsymbol{a}_n = [a_{0,n}, a_{1,n}, ..., a_{N-1,n}]^T$, $\boldsymbol{r}_n = [r_n(0), r_n(1), ..., r_n(N-1)]^T$, then

$$\begin{aligned} \boldsymbol{s}_n &= \text{IDFT}(\boldsymbol{a}_n) \\ \boldsymbol{r}_n &= \boldsymbol{H}\boldsymbol{s}_n + \boldsymbol{w}_n \\ \tilde{\boldsymbol{a}}_n &= \text{DFT}(\boldsymbol{r}_n) \end{aligned}$$

where $\boldsymbol{H}$ is the channel matrix and $\boldsymbol{w}_n$ is the noise components. Consequently, the whole system of OFDM can be efficiently implemented by the FFT/IFFT module and this makes OFDM an attractive option in high data rate applications.

Guard interval and cyclic prefix

When there is multipath propagation, subsequent OFDM symbols overlap with each other and hence cause serve ISI which degrades the performance of OFDM system by introducing an error floor for the Bit Error Rate (BER). That is, the BER will converge to a constant value with increasing SNR. A simple and straightforward

[3] except for a scaling factor N

approach which is standardized in OFDM applications is to add a guard interval [4] into the prototype function for synthesis basis and meanwhile keeps the prototype function for analysis basis unchanged. When the duration of the guard interval T_g is longer than the time dispersion T_d, ISI can be totally removed. With a guard interval added, the prototype function

$$q(t) = \begin{cases} \frac{1}{\sqrt{T}}, & -T_g \leq t < T \\ 0, & \text{elsewhere} \end{cases} \tag{2.19}$$

is used at the transmitter side and the synthesis basis (2.10) becomes

$$q_{m,n}(t) = e^{j2\pi mFt} q(t - nT_0) \tag{2.20}$$

where $T_0 = T_g + T$. On the receiver side the analysis basis prototype function remains the same as defined in (2.13) with time shift T_0 and integration region $nT_0 \leq t < nT_0 + T$. The orthogonality condition (2.14) between synthesis basis and analysis basis therefore becomes

$$\begin{aligned} &\langle g_{m,n}, q_{m',n'} \rangle = \textstyle\int_R e^{j2\pi(m'-m)Ft} g^*(t - nT_0) q(t - n'T_0) dt \\ &= \tfrac{1}{\sqrt{F}} \textstyle\int_{nT_0}^{nT_0+T} e^{j2\pi(m'-m)Ft} q(t - n'T_0) dt = \begin{cases} 1, & m = m' \text{ and } n = n' \\ 0, & \text{otherwise} \end{cases} \end{aligned} \tag{2.21}$$

Now, assuming that the guard interval $T_g = GT_s, G \in \mathbb{N}$, if we sample the signal $s(t)$ at the same sampling rate $1/T_s$ during the time interval $nT_0 - T_g \leq t < nT_0 + T$ and normalize it by $\sqrt{T}$

$$c_n(k) \triangleq s(nT_0 + kT_s) = \sum_{m=0}^{N-1} a_{m,n} e^{j2\pi \frac{mk}{N}}, \quad \begin{matrix} k = -G, -G+1, ..., 0, ..., N-1 \\ n \in \mathbb{Z} \end{matrix} \tag{2.22}$$

Rewriting the above expression in vector format, we get

$$\begin{aligned} \boldsymbol{c}_n &= [s_n(-G), s_n(1-G), ..., s_n(-1), s_n(0), ..., s_n(N-1)]^T \\ &= [\underbrace{s_n(N-G), s_n(N-G+1), ..., s_n(N-1)}_{\text{the LAST } G \text{ elements of } \boldsymbol{s}_n}, \underbrace{s_n(0), ..., s_n(N-1)}_{\boldsymbol{s}_n}]^T \end{aligned} \tag{2.23}$$

where the second equality comes from the periodic property of DFT function and the first G elements are referred as the *Cyclic Prefix* (CP). That is, to add a guard interval into the pulse shape prototype function is equivalent to add a cyclic prefix into the transmitted stream after OFDM modulation (IFFT). At the receiver side, the first G samples which contain ISI are just ignored. The system diagram of OFDM with cyclic prefix is shown in Fig. 2.2.

[4] There is another term "guard space" used in the early stage of OFDM development [27] which means to add zeros at the transmitter side. The "guard interval" used in this thesis means the usage of signals defined in the way in (2.19).

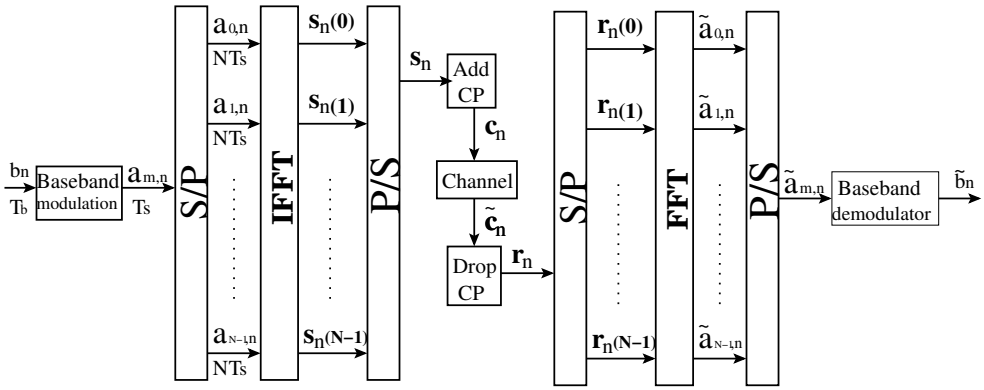

Figure 2.2: OFDM system with cyclic prefix.

After adding cyclic prefix, the spectral efficiency η in (2.17) becomes

$$\eta = \frac{\log_2 M}{T_0 F} = \frac{T}{T_0}\log_2 M = \frac{T_0 - T_g}{T_0}\log_2 M = (1 - \frac{T_g}{T_0})\log_2 M \text{ [bit/s/Hz]} \quad (2.24)$$

that is, the cyclic prefix costs a loss of spectral efficiency by $\frac{T_g}{T_0}$.

Summary

OFDM is now well known as an efficient technology for wireless communications. However, it takes about 30 years before OFDM being accepted as the candidate solution for high data rate transmission through wireless channels. Dr. Robert Wu-lin Chang first demonstrated in his 1966 paper [25] the principle of free ISI/ICI parallel data transmission over linear band-limit channel, which forms the concept we today call OFDM. In 1967, B.R. Saltzberg [26] evaluated the performance and pointed out the key factor is to reduce crosstalk between sub-channels (ICI). Implementation of OFDM via DFT/IDFT was proposed by Weinstein and Ebert [27] in 1971, where the "guard space" (zeros) in time domain was introduced to remove ISI but cost a loss of orthogonality. Until 1980 the concept of *cyclic prefix* was introduced by Peled and Ruiz [28], which brought the theoretical development of OFDM to a new stage. However, OFDM is lack of interest until the middle of 1990s when the fast development of digital signal processor chips makes FFT based OFDM implementation practical.

If there is no frequency dispersion present, ISI/ICI can be fully eliminated by adding a sufficiently long CP. The wireless channel, however, often contains both time and frequency dispersion which eventually destroys the orthogonality between the perturbed synthesis basis functions and the analysis basis functions. Furthermore, CP is not for free: It costs increased power consumption and reduces spectral efficiency.

One way to solve this problem is to adopt a proper pulse shape prototype filter (rather than the rectangular function) which is well localized in time and frequency domain so that the combined ISI/ICI can be combated efficiently without utilizing any CP. Unfortunately, the Balian-Low theorem [24] implies that the construction of a well time-frequency localized orthogonal basis is impossible for unitary time frequency density ($\sigma = \frac{1}{TF} = 1$). Therefore orthogonal basis and well localised pulse shapes cannot be achieved simultaneously for OFDM unless extra symbol duration (e.g. guard interval) or extra frequency bandwidth is introduced. On the other hand, orthogonality which ensures low demodulation complexity, cannot be simply given up as it plays an important role in the cost calculation. This dilemma brings GFDM into sight.

2.3 Overview of GFDM

GFDM is of great interest as it has shown promising advantages over OFDM on robustness to both time and frequency dispersion. The CP is avoided in GFDM at the price of a more complicated design of well localised pulse shapes [3]- [8], where orthogonality over ideal channels is ensured with a smaller lattice density ($\sigma < 1$). The optimally localised Gaussian function is used for pulse shaping in [15] where a powerful detector is used to combat its non-orthogonality. A frame work of orthogonalisation, named as Isotropic Orthogonal Transform Algorithm (IOTA), has been proposed in [5] to orthogonalise the Gaussian function. The IOTA method turns out to be identical with the orthogonalisation method used in [14] for certain pulses. As a generalisation of the IOTA method, a closed-form expression for the class of the resulting functions has been proposed in [6]. As the resulting functions inherit the localisation property of the Gaussian function, they are named Extended Gaussian Functions (EGF). In [29] it is shown that EGF functions can also be derived based on the Zak Transform. Motivated by the fact that the Gaussian function is just the first Hermite function, a linear combination of several Hermite functions whose frequency transforms are the same as themselves is proposed in [8] to form a new mother function which is subject to optimisation. Some alternative approaches are proposed to find prototype functions that only extend to one OFDM symbol duration, which will cause smaller detection delay and lower complexity. In [12] the half-cosine function is proposed as the pulse shape prototype and its dual function square root raised cosine (RRC) function and its self-multiplied versions are proposed in [7]. Optimisation methods aiming at maximising the time frequency localisation measures of the truncated EGF functions are proposed in [30, 31], and the resulting functions are therefore named by TFL1.

More degrees of freedom in pulse shape design are introduced by using different prototype functions at the transmitter and receiver side, as reported in [9]- [11], and therefore yields stronger immunity to channel dispersion. OFDM with offset QAM (OFDM/OQAM) [12, 13] which transmits real symbols with double lattice density has shown advantages over CP-OFDM by stronger channel dispersion im-

munity and higher spectrum efficiency, but faces difficulties of channel estimation and equalization. All the aforementioned contributions demonstrate "zero tolerance" to ISI/ICI in AWGN channels and therefore ensure perfect reconstruction in absence of a channel. In the doubly dispersive wireless channels, however, *perfect reconstruction* is destroyed and considerable ISI/ICI is introduced. Hence the key focus should be put on the maximisation of spectral efficiency and meanwhile keep the level of ISI/ICI to a certain level tolerated by the system requirements. For example, general system lattice grids rather than the rectangular one used in OFDM have also been proposed [14] and optimal system parameters are proposed for channels with a uniform distributed scattering function to minimise the joint ISI/ICI. In [15] it is shown that further improvements can be achieved by using Gaussian pulses and a hexagonal lattice which is composed by superposition of two rectangular lattices. The price to pay is higher complexity and longer detection delay introduced by the sequential detector based on minimum mean-square-error (MMSE) criterion. When the number of sub-carriers is very large, say $N = 2048$ as proposed in WRAN standard, the detection delay can be extremely large and therefore hinders its application in wireless communications such as mobile telephony and live streaming.

On the other hand, some enhancement techniques for OFDM can also be extended to GFDM without difficulties as GFDM inherits most of the properties of OFDM due to the similarities between GFDM and OFDM in terms of using subcarriers. It is advantageous to design a multiple access technology based on GFDM technology to support heterogeneous access networks that are OFDM-based, i.e. 3G-LTE, 802.16, 802.22, etc.

System model

A general system model for GFDM systems with different system lattices is formulated in the following way.

Signal basis with rectangular lattice

Given a rectangular lattice $\Lambda = \begin{bmatrix} \tau_0 & 0 \\ 0 & \nu_0 \end{bmatrix}$, the transmitted signal basis with prototype $g(t)$ can be written as

$$g_{m,n} = g(t - n\tau_0)e^{j2\pi m\nu_0 t}$$

and the signal basis at the receiver side with prototype $q(t)$ can be written as

$$q_{m,n} = q(t - n\tau_0)e^{j2\pi m\nu_0 t}$$

where τ_0 serves as the time separation and ν_0 as the frequency separation. The analysis-synthesis pair is called orthogonal or bi-orthogonal if $< g_{m,n}, q_{m',n'} >= \delta_{mm',nn'}$ is ensured with the prototype functions $g(t)$ and $q(t)$ identical or different,

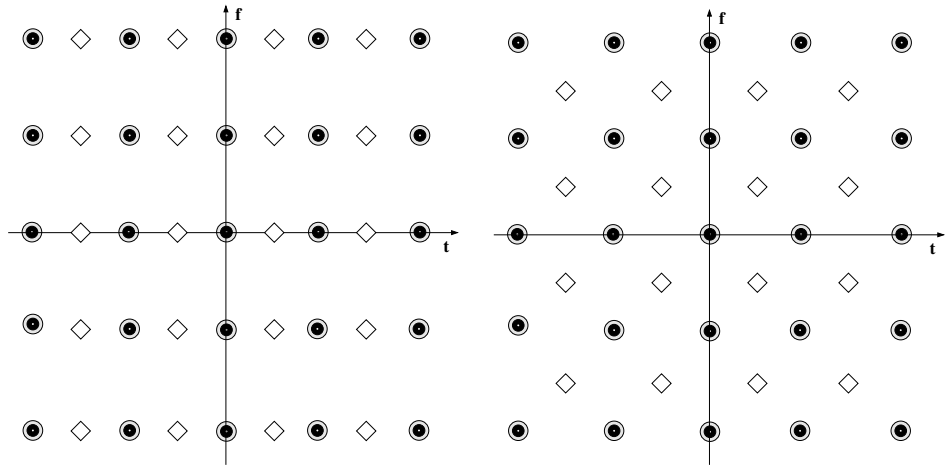

(a) (b)

Figure 2.3: Symbol positions at the time frequency plan for (a) rectangular and (b) hexagonal system lattice.

respectively.

Signal basis with hexagonal lattice

Given a hexagonal lattice $\Lambda = \begin{bmatrix} \tau_0 & p\tau_0 \\ 0 & \nu_0 \end{bmatrix}$ or $\Lambda = \begin{bmatrix} \tau_0 & 0 \\ p\nu_0 & \nu_0 \end{bmatrix}$, $p > 0$,
the transmitted signal basis with prototype $g(t)$ can be written as

$$g_{m,n} = g(t - (n + pm)\tau_0)e^{j2\pi m\nu_0 t} \text{ or } g_{m,n} = g(t - n\tau_0)e^{j2\pi(m+pn)\nu_0 t}$$

respectively and the signal basis at receiver side can be formulated accordingly.

Notice that all the lattices mentioned above have the same density for any value of p

$$\sigma = 1/\det(\Lambda) = \frac{1}{\tau_0\nu_0}$$

Symbol positions at the time-frequency plan are shown in Fig. 2.3 for the rectangular lattice (a) and the hexagonal lattice (b, with $p = 1/2$). Clearly, the hexagonal lattice can be formulated by superposition of two rectangular lattices: (b) can be generated by shifting all the lattice points indicated by white square in (a) along the frequency axis by $0.5\nu_0$ and keeping all the other lattice points unchanged. Define the normalised minimum time-frequency distance between neighbouring lattice points as

$$d_\Lambda = \sqrt{(\frac{\delta t}{\tau_0})^2 + (\frac{\delta f}{\nu_0})^2}$$

where δt and δf is the minimum distance in time and in frequency, respectively. For the rectangular lattice shown in Fig. 2.3 a, we have

$$d_\Lambda = \sqrt{(\frac{\tau_0}{\tau_0})^2 + 0} = \sqrt{0 + (\frac{\nu_0}{\nu_0})^2} = 1$$

For the hexagonal lattice shown in in Fig. 2.3 b, we have

$$d_\Lambda = \sqrt{(\frac{\tau_0}{\tau_0})^2 + (\frac{0.5\nu_0}{\nu_0})^2} = \sqrt{1.25} \approx 1.12$$

Therefore with the same lattice density, the hexagonal lattice provides larger normalised minimum time-frequency distance than the rectangular lattice.

Principle of GFDM design

Pulse shapes design

The ideal pulse shape for wireless communication in a designer's dream is expected to have the following properties: it attenuates very sharply both in time and frequency domain so that there will be no overlap with adjacent symbols and therefore no ISI/ICI is introduced. Unfortunately such pulse shapes does not exist and a compromise between attenuation property in time and frequency domain has to be sought dependent on the channel characteristics. The idea of pulse shapes design is to find an efficient transmitter and a corresponding receiver waveform for the current channel condition [7, 10], so that the resulting ISI/ICI will be minimized. Specifically, a *good* signal waveform should be compactly supported and well localized in time and in frequency with the same time-frequency scale as the channel itself:

$$\frac{\Delta t}{\Delta \tau} \approx \frac{\Delta f}{\Delta \nu} \tag{2.25}$$

where Δt and Δf are the time and frequency scale of the pulse shape itself and $\Delta \tau$ and $\Delta \nu$ are the delay and frequency dispersion measure of the wireless channel. $\Delta \tau$ and $\Delta \nu$ can be the root-mean-square (RMS) delay spread and frequency (Doppler) spread, respectively, for continuous time channel model, or the maximum delay and Doppler spread when a discrete time channel model is used. For example, in indoor situations the time dispersion is usually small, see Fig 2.4, a vertically stretched time-frequency pulse is suitable and where the frequency dispersion is small, a horizontally stretched pulse is suitable. This enables a very efficient packing [14] of time-frequency symbols and hence maximises the throughput or the interference robustness in the communication link.

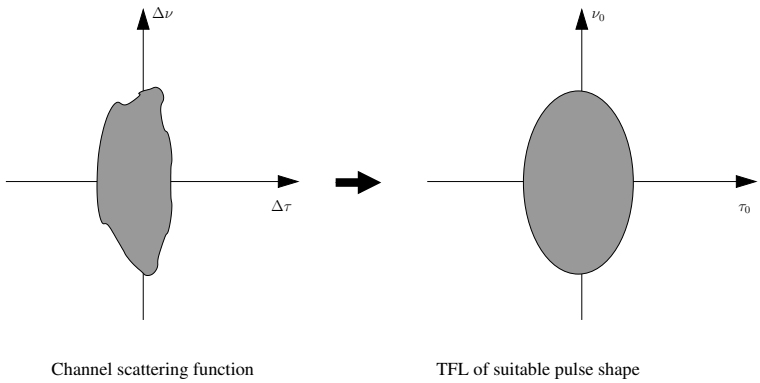

Figure 2.4: Channel scattering function and corresponding pulse shape.

General system lattice

According to Graph theory, the regular[5] hexagonal lattice structure (its elementary hexagon regular) is optimal in two dimensional space in the sense that it can achieves the largest distances among lattice points and meanwhile maintains the same lattice density. Compared with a rectangular lattice structure, a regular hexagonal lattice with the same lattice density will increase the distance among different lattice points and therefore decrease the joint ISI/ICI. However, as shown in the pulse shape design part, the pulse shape itself may have different scale along the time and frequency axes and therefore a regular hexagonal lattice will be impossible to achieve. Hence irregular hexagonal lattices which can be achieved by superposition of two rectangular lattices are frequently used instead.

Joint optimisation of pulse shape and system lattice

A joint optimisation of the pulse shape and the system lattice should take all the related parameters (τ_0, ν_0, p, Δt, Δf) into consideration and find the optimal parameters so that a given object function will be maximised/minimised. However, it is a very complicated task and the closed-form analytical solutions only exist for very special cases. We will discuss this in detail in Chapter 3.

2.4 Time Frequency Localization (TFL)

The time-frequency translated versions of the prototype function, as shown in equations (2.10) and (2.20), form a lattice in the time-frequency plane, as shown in Fig. 2.3. If the prototype function, which is assumed to be centered around the origin, has nearly compact support along the time-frequency axes, the transmitted

[5] A hexagon with all sides and all angles equal is called a regular hexagon, otherwise irregular.

signal composed by these basis functions will place a copy of the prototype function on each lattice point in the time-frequency plane. This illustrates how the signal from different carriers and different symbols are combined in the lattice. The lower power the prototype function spreads to the neighboring lattice region, the better reconstruction of the transmitted signal can be retrieved after demodulation.

TFL functions

Several TFL functions, the instantaneous correlation function, the ambiguity function and the interference function, are commonly used to demonstrate the TFL property and are therefore discussed below.

Instantaneous correlation function

Two kinds of instantaneous[6] correlation functions are usually used: the instantaneous cross-correlation function and the instantaneous autocorrelation function. The instantaneous cross-correlation function between synthesis prototype function $q(t)$ and analysis prototype function $g(t)$ is defined as

$$\gamma_{g,q}(\tau,t) = g(t+\tau/2)q^*(t-\tau/2) = \gamma^*_{g,q}(-\tau,t) \tag{2.26}$$

and the instantaneous auto-correlation function is as follows

$$\gamma_g(\tau,t) \triangleq \gamma_{g,g}(\tau,t) = g(t+\tau/2)g^*(t-\tau/2) = \gamma^*_g(-\tau,t) \tag{2.27}$$

When $g(t)$ is even, we get

$$\gamma^*_g(\tau,-t) = g^*(-t+\tau/2)g(-t-\tau/2) = g^*(t-\tau/2)g(t+\tau/2) = \gamma_g(\tau,t) \tag{2.28}$$

which states that $\gamma_g(\tau,t)$ is even conjugate both with respect to τ and t.

Ambiguity function

The corresponding cross-ambiguity function of $g(t)$ and $q(t)$ is defined[7] as the Fourier transform of the cross-instantaneous correlation function along the time axis t, i.e.,

$$\begin{aligned} A_{g,q}(\tau,\nu) &\triangleq \int_{\mathbb{R}} \gamma_{g,q}(\tau,t)e^{-j2\pi\nu t}dt = \int_{\mathbb{R}} g(t+\tau/2)q^*(t-\tau/2)e^{-j2\pi\nu t}dt \\ &= e^{-j\pi\tau\nu}\int_{\mathbb{R}} g(t+\tau)q^*(t)e^{-j2\pi\nu t}dt = e^{-j\pi\tau\nu} < q(t)e^{j2\pi\nu t}, g(t+\tau) > \end{aligned} \tag{2.29}$$

[6] "Instantaneous" is used here to indicate that no expectation is taken compared to the common correlation function.

[7] There is another definition for the ambiguity function, which differs by a phase shift.

where the second equality comes from variable substitution. Similarly, the auto-ambiguity function can be regarded as a special case of the cross-ambiguity function when $g(t) = q(t)$

$$A_g(\tau,\nu) \triangleq \int_{\mathbb{R}} \gamma_g(\tau,t) e^{-j2\pi\nu t} dt = e^{-j\pi\tau\nu} < g(t) e^{j2\pi\nu t}, g(t+\tau) > \tag{2.30}$$

As long as the prototype function is normalized (i.e. unity energy), the maximum of the auto-ambiguity function is

$$\max_{\tau,\nu} |A_g(\tau,\nu)| = A_g(0,0) = 1$$

On the other hand, the maximum value of the cross-ambiguity function $|A_{g,q}(\tau,\nu)|$ depends on the matching between $g(t)$ and $q(t)$ and hence is equal to or less than unity. The ambiguity function can therefore be used as an indicator of the orthogonality/similarity between the prototype function and its time and frequency translated version (e.g. $|A_g(\tau,\nu)| = 0$ means *orthogonal* and $|A_g(\tau,\nu)| = 1$ means *identical*), or to show to what an extent the analysis basis is matched to the corresponding synthesis basis (the larger $|A_{g,q}(\tau,\nu)|$ is, the better the demodulator works).

Several important features of the ambiguity function need to be highlighted:

- It is a two dimensional (auto-)correlation function in the time-frequency plane.
- It is real valued in the case of an even prototype function, i.e. $g(-t) = g(t)$.
- It illustrates the sensitivity to delay and frequency offset.
- It gives an intuitive demonstration of ICI/ISI robustness.

Interference function

To obtain a more clear image of how much interference (power) has been induced to other symbols on the time frequency lattice, a so called interference function has been introduced

$$I(\tau,\nu) = 1 - |A(\tau,\nu)|^2 \tag{2.31}$$

where $A(\tau,\nu) = A_g(\tau,\nu)$ for the auto-ambiguity function case. In the case of cross-ambiguity function, $A(\tau,\nu) = A_{g,q}(\tau,\nu)$ has to be normalized so that $I(\tau,\nu) = 0$ when there is no interference.

TFL parameters

Heisenberg parameter ξ

The Heisenberg parameter ξ [5, 12] is frequently used to measure the TFL properties of a given function $x(t)$ and its Fourier transform $X(f)$. According to the

Heisenberg Uncertainty Principle [24], the Heisenberg parameter is given by

$$\xi = \frac{1}{4\pi\Delta t\Delta f} \leq 1 \tag{2.32}$$

where Δt is the mass moment of inertia of the prototype function in time and Δf in frequency, which shows how the energy (mass) of the prototype function spreads over the time and frequency plane. The larger Δt (Δf), the more spread there is concerning the time (frequency) support of the prototype function. These two parameters can be calculated via the following set of equations

$$\begin{cases} \Delta t^2 = K \int_{\mathbb{R}} (t-\bar{t})^2 |x(t)|^2 dt \\ \Delta f^2 = K \int_{\mathbb{R}} (f-\bar{f})^2 |X(f)|^2 df \\ \bar{t} = K \int_{\mathbb{R}} t|x(t)|^2 dt \\ \bar{f} = K \int_{\mathbb{R}} f|X(f)|^2 df \\ K^{-1} = \int_{\mathbb{R}} |x(t)|^2 dt = \int_{\mathbb{R}} |X(f)|^2 df \end{cases} \tag{2.33}$$

where $E = K^{-1}$ is the energy of the prototype function, $\bar{t}$ and $\bar{f}$ are the center value (center of gravity) of the time and frequency energy distribution and corresponding to the coordinates of its lattice point in the time-frequency plane, i.e., for $x(t) = g_{m,n}(t)$, it is easy to prove that $\bar{t} = n\tau_0$ and $\bar{f} = m\nu_0$. Therefore, $(\bar{t}, \bar{f})$ indicates the center position in the time-frequency plane of the prototype function and $(\Delta t, \Delta f)$ describes how large area it occupies to accommodate most of its energy.

According to the Heisenberg uncertainty inequality, $0 \leq \xi \leq 1$, where the upper bound $\xi = 1$ is achieved by the Gaussian function and the lower band $\xi = 0$ is achieved by the rectangular function whose Δf is infinite. The larger ξ is, the better joint time-frequency localization the prototype function has (or alternatively speaking, the less area it occupies). Although the Gaussian function enjoys he minimum joint time-frequency localization (highest Heisenberg parameter), it is always positive and therefore can not be orthogonal as stated before.

Direction parameter κ

In order to show quantitatively how the pulse shape spreads over the T-F plane, we define the Direction parameter

$$\kappa = \frac{\Delta t}{\Delta f}.$$

κ can be any value between $[0, \infty)$ where the minimum is achieved by the rectangular function whose $\Delta f = \infty$. $\kappa = 1$ (e.g. the Gaussian function) means that

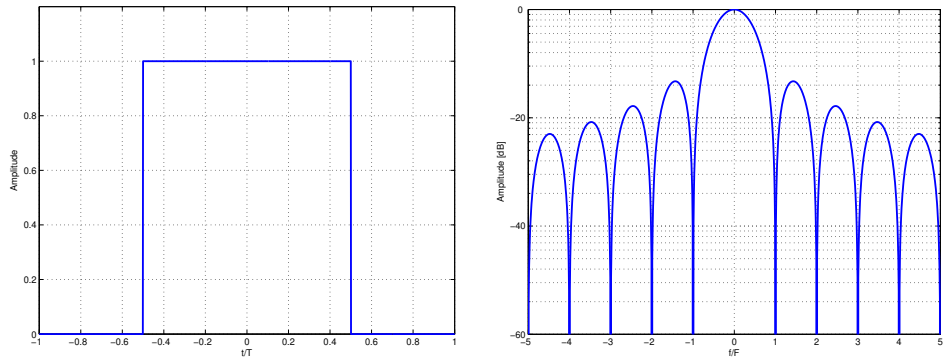

(a) Rectangular function (b) Its frequency response

Figure 2.5: Rectangular function $g(t)$ and its Fourier transform, the sinc function.

the pulse shape has the same time and frequency scale in the time-frequency plane. The larger κ is, the more stretched along the time axis the pulse shape is.

2.5 Pulse shape prototype functions and their TFL properties

In this section, several different types of pulse shape functions are presented, namely the rectangular function, the half cosine function, the Gaussian function, the IOTA function, the EFG function, and the TFL1 function. All figures in this section are drawn with normalised time and frequency axes by τ_0 and ν_0, respectively.

Rectangular function for OFDM

The rectangular prototype function is a possible choice and can be a benchmark for comparison. A time shift has to be applied to ensure the even function property, as shown in (2.34).

$$g(t) = \begin{cases} \frac{1}{\sqrt{\tau_0}}, & |t| \leq \frac{\tau_0}{2} \\ 0, & \text{elsewhere} \end{cases} \quad \text{and } G(f) = \frac{\sin(\pi\tau_0 f)}{\pi f\sqrt{\tau_0}} \tag{2.34}$$

The Fourier transform $G(f)$ is nothing but a sinc function[8] which has the first side lobe of -13dB and decades very slowly along the frequency axis, as shown in Fig. 2.5 b.

[8]It is sometimes called the sampling interpolation function in some literature.

By interchanging time and frequency axes, the dual of the rectangular function becomes a natural extension, which is defined in the frequency domain as follows

$$G(f) = \begin{cases} \frac{1}{\sqrt{\nu_0}}, & |f| \leq \frac{\nu_0}{2} \\ 0, & \text{elsewhere} \end{cases} \quad \text{and } g(t) = \frac{\sin(\pi\nu_0 t)}{\pi t\sqrt{\nu_0}} \tag{2.35}$$

Its obvious advantage over rectangular function is that there is no overlapping in the frequency domain and therefore causes less interference. On the other hand, with a longer duration in the time domain, the implementation and equalization complexity is considerable even after proper truncation.

For OFDM without CP, auto-correlation function (2.27), auto-ambiguity function (2.30) are used to get the TFL figures. Plots for there interference function are obtained via (2.31) with attention paid to proper normalization for the cyclic prefix case.

For the rectangular functions

$$g(t) = \begin{cases} \frac{1}{\sqrt{T}}, & |t| \leq \frac{T}{2} \\ 0, & \text{elsewhere} \end{cases} \quad \text{and } q(t) = \begin{cases} \frac{1}{\sqrt{T}}, & |t| \leq \frac{T_0}{2} \\ 0, & \text{elsewhere} \end{cases}$$

where $T_0 = T + T_g$ is the duration of the pulse shape with CP added, as shown in Appendix 2.6 C, the cross-ambiguity function (2.29) becomes

$$A_{g,q}(\tau,\nu) = \begin{cases} e^{j\pi\nu\tau}\dfrac{\sin\pi\nu T}{\pi\nu T}, & |\tau| \leq \dfrac{T_0 - T}{2} \\ e^{j\pi\nu(T_0-T)/2}\dfrac{\sin\left[\pi\nu(\frac{T+T_0}{2} - \tau)\right]}{\pi\nu T}, & \dfrac{T_0 - T}{2} < \tau < \dfrac{T_0 + T}{2} \\ e^{j\pi\nu(T-T_0)/2}\dfrac{\sin\left[\pi\nu(\frac{T+T_0}{2} + \tau)\right]}{\pi\nu T}, & -\dfrac{T_0 + T}{2} < \tau < -\dfrac{T_0 - T}{2} \\ 0, & |\tau| \geq \dfrac{T_0 + T}{2} \end{cases} \tag{2.36}$$

and the auto-ambiguity function (2.30) becomes

$$A_g(\tau,\nu) = \begin{cases} \dfrac{\sin\left[\pi\nu T\left(1 - \frac{|\tau|}{T}\right)\right]}{\pi\nu T} & , |\tau| < T \\ 0 & , |\tau| \geq T \end{cases} \tag{2.37}$$

Obviously $A_g(\tau,\nu)$ in (2.37) is a sinc function along the frequency axis with its amplitude $(1 - \frac{|\tau|}{T})$ decays symmetrically with increasing τ along the time axis. Therefore when CP is added, as shown in (2.36), the amplitude of sinc function keeps constant as long as $|\tau| \leq \frac{T_0 - T}{2}$ where $T_g = T_0 - T$ is the length of the CP. Note that both the prototype function $g(t)$ and $q(t)$ are time shifted here. Without the time shift, the expression for the ambiguity function will still be the sinc function with some time and phase shift.

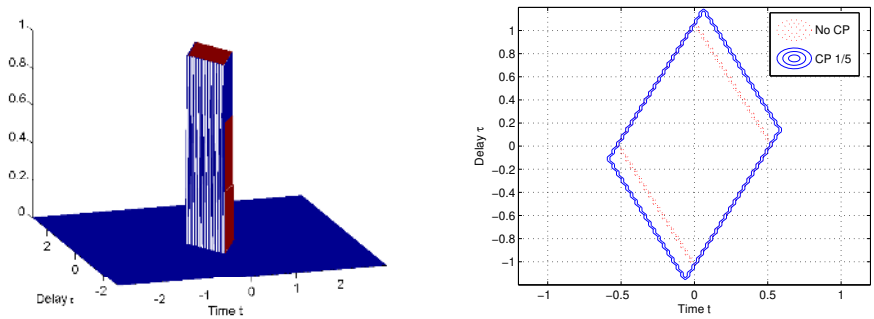

(a) correlation function (b) contour plots

Figure 2.6: Correlation function of rectangular prototype for no-CP (dotted) and CP (solid, $\frac{T_g}{T_0} = \frac{1}{5}$).

Fig. 2.6 shows how the correlation function of rectangular prototype function looks like and demonstrates the difference for OFDM systems with and without CP. The Sharp edge of the correlation function comes from the time limitation of the rectangular function. Compared to the no-CP case, CP enlarges the coverage of the correlation function and reduces the sensitivity to time spread. This "extra" coverage can easily be found at the upper-right border and lower-left border of the contour plots shown in Fig. 2.6(b).

Fig. 2.7 displays the ambiguity function which demonstrates how the mismatch in time and frequency between the analysis basis and the corresponding synthesis basis will affect the demodulation, or equivalently, how large the power leakage of the prototype function is between neighboring lattice points after time and frequency dispersion being added by the channel, where the role the cyclic prefix plays is clearly shown. In no-CP case shown in Fig. 2.7(a), the demodulation gain will fall sharply even with a minor time or frequency mismatch. After cyclic prefix is added, as shown in Fig. 2.7(b) where the phase of $A_{g,q}$ is omitted, the demodulation gain will remain the same as long as the time mismatch is within the length of cyclic prefix duration. This property is shown more clearly by their contour plots in Fig. 2.7(c, d).

The sensitivity of OFDM system to time and frequency spread and the effect of cyclic prefix have been intuitively demonstrated by the interference function plotted in Fig. 2.8. The width of the flat bottom of the interference function for cyclic prefix corresponds to the length of the cyclic prefix added into the synthesis basis functions.

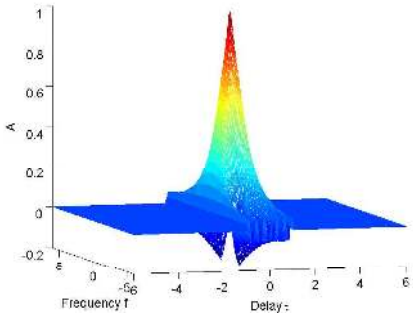

(a) No cyclic prefix

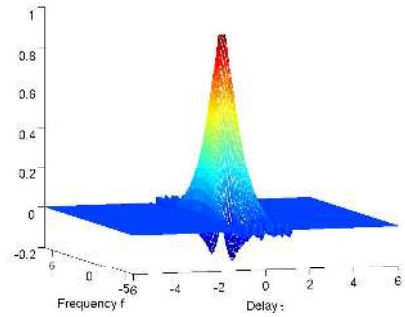

(b) Cyclic prefix $\frac{T_g}{T_0} = \frac{1}{5}$

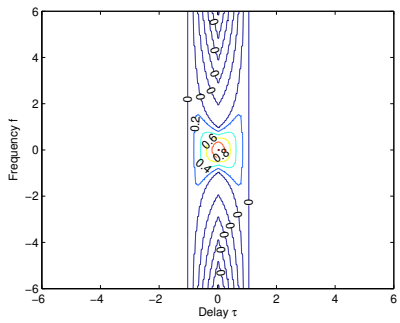

(c) No CP, contour plot

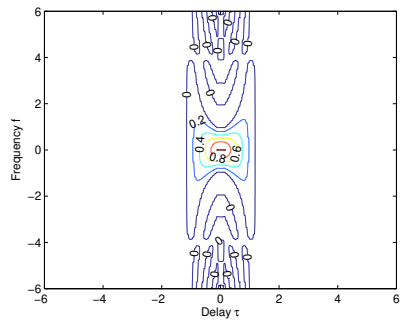

(d) CP, contour plot

Figure 2.7: Ambiguity function of rectangular prototype.

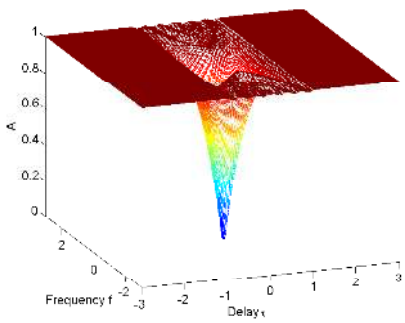

(a) No cyclic prefix

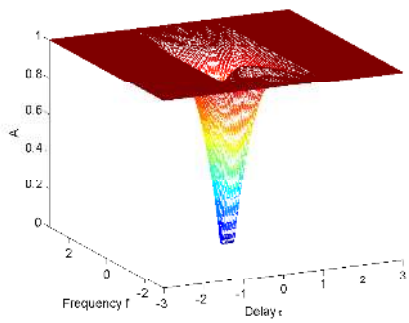

(b) Cyclic prefix $\frac{T_g}{T_0} = \frac{1}{5}$

Figure 2.8: Interference function of rectangular prototype.

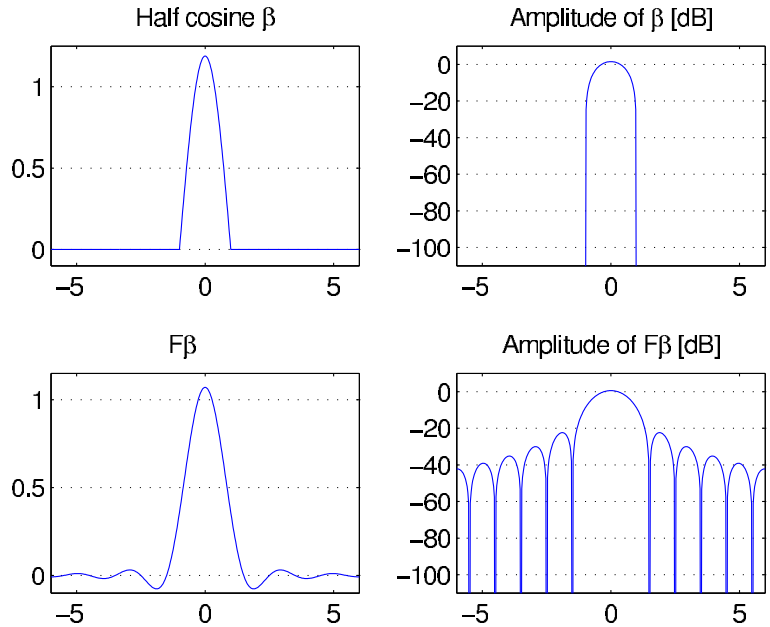

Figure 2.9: Half cosine function and its Fourier transform.

Half-cosine function

The half cosine function is defined by

$$g(t) = \begin{cases} \frac{1}{\sqrt{\tau_0}} \cos \frac{\pi t}{2\tau_0}, & |t| \leq \tau_0 \\ 0, & \text{elsewhere} \end{cases} \tag{2.38}$$

It has a compact support[9] in the time domain and meanwhile a fast decay in the frequency domain, as shown in Fig. 2.9, and therefore serves as a good prototype function. Its ambiguity function, as shown in Appendix 2.6 C, is

$$A_g(\tau,\nu) = \begin{cases} \frac{\sin \pi(1-2\tau_0\nu)(1-\frac{|\tau|}{2\tau_0})}{2\pi(1-2\tau_0\nu)} + \frac{\sin \pi(1+2\tau_0\nu)(1-\frac{|\tau|}{2\tau_0})}{2\pi(1+2\tau_0\nu)} + \frac{\cos \frac{\pi\tau}{2\tau_0} \sin 2\pi\tau_0\nu(1-\frac{|\tau|}{2\tau_0})}{2\pi\tau_0\nu} & , |\tau| < 2\tau_0 \\ 0 & , |\tau| \geq 2\tau_0 \end{cases}$$

Therefore it is the superposition of three sinc functions with their amplitude dependent on τ.

[9] A function $x(t)$ is said to be compact support if there exists a constant $\varepsilon > 0$ so that $x(t) = 0$ for all $|x| > \varepsilon$.

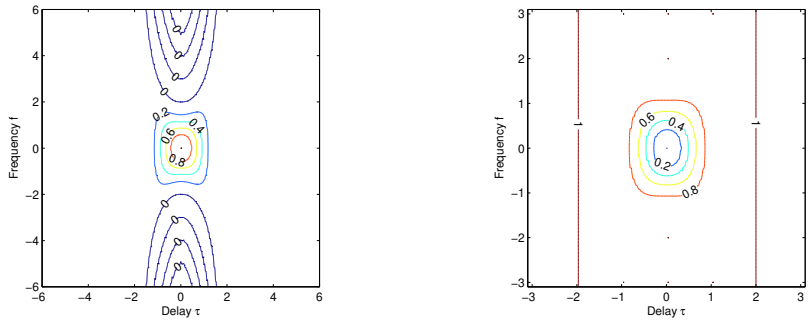

(a) Auto-ambiguity function (b) Interference function

Figure 2.10: Half cosine prototype (contour, step=0.2).

Similarly, its dual form is instead defined by its Fourier transform as

$$G(f) = \begin{cases} \frac{1}{\sqrt{\nu_0}} \cos \frac{\pi f}{2\nu_0}, & |f| \leq \nu_0 \\ 0, & \text{elsewhere} \end{cases} \tag{2.39}$$

Actually (2.39) is a special case of the square-root raised-cosine pulse in the frequency domain with the roll-off factor $\rho = 1$. Therefore it will be referred as RRC from now on. This prototype function can be extended to any real even function whose Fourier transform $G(f)$ satisfies the following conditions:

$$\begin{cases} |G(f)|^2 + |G(f-\nu_0)|^2 = 1/\nu_0 & |f| \leq \nu_0 \\ G(f) = 0 & \text{otherwise} \end{cases} \tag{2.40}$$

which corresponds to a half-Nyquist filter [12, 32].

As half cosine prototype function and its dual form has the same orthogonality and TFL property but has the time and frequency axes shifted, only the half cosine function in the time domain described in (2.38) is treated here. The contour plots which can provide a clearer image of the quantity aspects are used here for comparison between different schemes. It has a smaller power leakage along the time axis than the frequency axis, as shown in Fig. 2.10. Its dual form will of course have the opposite property as only the axes are interchanged.

Gaussian function

Gaussian function is very famous for that its Fourier transform has the same shape as itself except for an axis scaling factor. For a Gaussian function

$$g_\alpha(t) = (2\alpha)^{1/4} e^{-\pi \alpha t^2}, \ \alpha > 0 \tag{2.41}$$

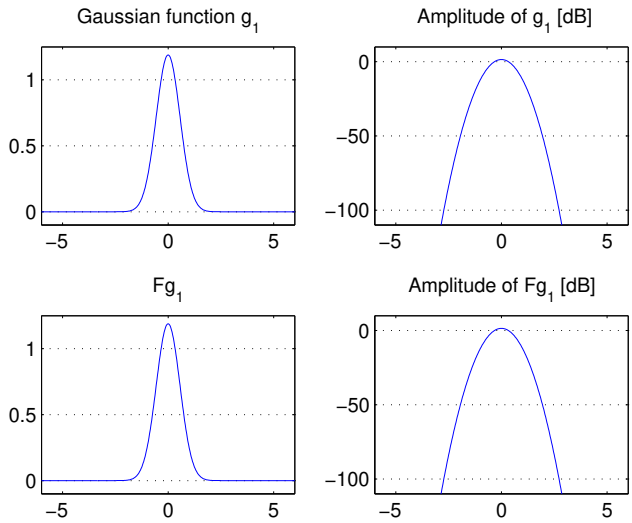

Figure 2.11: Gaussian function with $\alpha = 1$ and its Fourier transform.

its Fourier transform is

$$\begin{aligned}\mathcal{F}g_\alpha(t) &= (2\alpha)^{1/4}\int_{-\infty}^{\infty} e^{-\pi\alpha t^2} e^{-j2\pi ft} dt = (2\alpha)^{1/4}\sqrt{\frac{\pi}{\pi\alpha}} e^{(-j\pi f)^2/(\pi\alpha)} \\ &= (2/\alpha)^{1/4} e^{-\pi f^2/\alpha} = g_{1/\alpha}(f).\end{aligned} \tag{2.42}$$

Here the second equality comes from the fact that [33]

$$\int_{-\infty}^{\infty} e^{2bt-at^2} dt = \sqrt{\frac{\pi}{a}} e^{b^2/a} \ (a > 0) \tag{2.43}$$

The ambiguity function for the Gaussian prototype, as shown in Appendix 2.6 C, is

$$A_{g_\alpha}(\tau, \nu) = e^{-\frac{\pi}{2}(\alpha\tau^2 + \frac{1}{\alpha}\nu^2)}$$

which means it decays at the second order of τ and ν simultaneously. As the Gaussian prototype function is perfectly isotropic (invariant under rotation) and has fast decay both in time and frequency domain, as shown in Fig. 2.11, it seems to be an attractive candidate for pulse shaping prototype function. On the other hand, the signal basis generated by Gaussian prototype function is in no way orthogonal as $g_\alpha(t) > 0$ holds on the whole real axis, and it expends over several symbol duration in the time domain and frequency sub-bands in the frequency domain and therefore cause intrinsic ISI/ICI, as shown in Fig. 2.12. It is not a trivial task to combat these distortions.

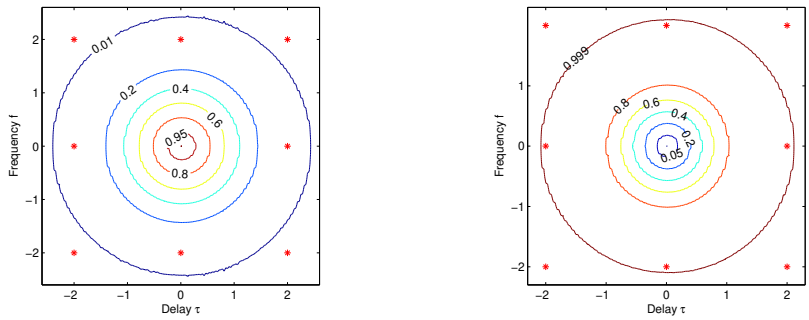

(a) Auto-ambiguity function (b) Interference function

Figure 2.12: Gaussian prototype with $\alpha = 1$, and $*$ indicate the position of the neighboring lattice points.

Isotropic Orthogonal Transform Algorithm (IOTA) function

Orthogonality between basis functions is normally obtained by using either a time or frequency limitation of the prototype function, for example, the rectangular function and the half cosine function. A different approach, called Isotropic Orthogonal Transform Algorithm (IOTA), is presented in [5, 12] and summarized below.

Define $\mathcal{O}_a$ as the orthogonalization operator on function $x(t)$ according to the following relation

$$\mathcal{O}_a x(t) = \frac{x(t)}{\sqrt{a \sum_{k=-\infty}^{\infty} |x(t-ka)|^2}}, \ a > 0 \tag{2.44}$$

The effect of the operator $\mathcal{O}_a$ is to orthogonalise the function $x(t)$ along the frequency axis, which can be seen directly on the ambiguity function

$$A_y\left(0, \frac{m}{a}\right) = 0, \ \forall m \neq 0 \text{ and } A_y(0,0) = 1 \tag{2.45}$$

where $y(t) = \mathcal{O}_a x(t)$. That is, the resulting function $y(t)$ and its frequency shifted versions construct an orthonormal set of functions. The proof can be found in Appendix 2.6 D.

Similarly, in order to orthogonalise $x(t)$ along the time axis, one can turn to frequency domain and apply this orthogonalization operator to $X(f)$, which is the Fourier transform of $x(t)$. To carry out this operation on $x(t)$, one has first to transfer it into frequency domain by Fourier transform $\mathcal{F}$, then apply to the orthogonalization operation $\mathcal{O}_a$, and then go back to the time domain by inverse Fourier transform $\mathcal{F}^{-1}$. For $y(t) = \mathcal{F}^{-1}\mathcal{O}_a\mathcal{F}x(t)$, we have

$$A_y\left(\frac{n}{a}, 0\right) = 0, \ \forall n \neq 0 \text{ and } A_y(0,0) = 1 \tag{2.46}$$

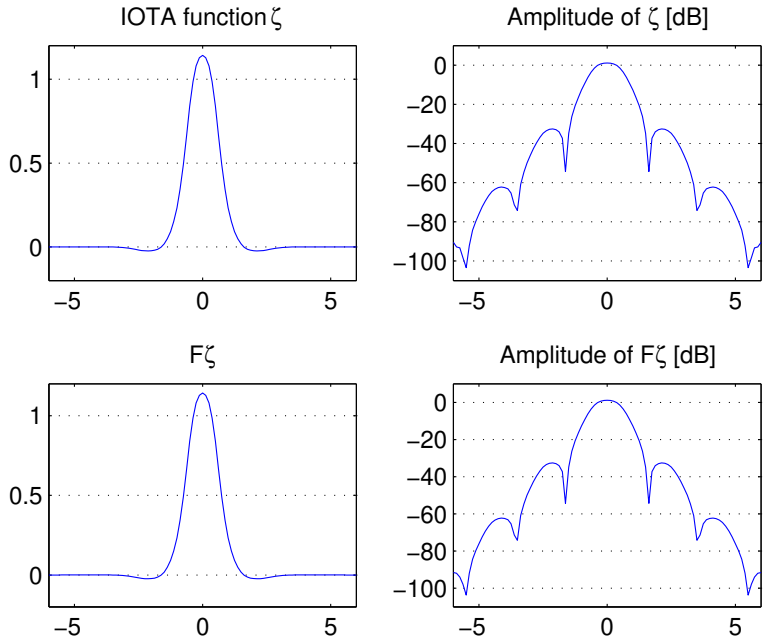

Figure 2.13: IOTA function and its Fourier transform.

Hence the resulting function and its time delayed forms are orthonormal.

Starting from the Gaussian function $g_\alpha(t)$, by applying $\mathcal{O}_{\tau_0}$ we get $y_\alpha(t) = \mathcal{O}_{\tau_0} g_\alpha(t)$ and

$$A_y\left(0, \frac{m}{\tau_0}\right) = 0, \ \forall m \neq 0, \text{ and } A_y(0,0) = 1$$

which comes from (2.45) and shows that y_α is orthogonal to its frequency shifted copies at multiples of $\frac{m}{\tau_0}$. Then apply $\mathcal{F}^{-1}\mathcal{O}_\nu\mathcal{F}$ to $y_\alpha(t)$, we get

$$z_{\alpha,\nu_0,\tau_0}(t) = \mathcal{F}^{-1}\mathcal{O}_{\nu_0}\mathcal{F}y_\alpha(t) = \mathcal{F}^{-1}\mathcal{O}_{\nu_0}\mathcal{F}\mathcal{O}_{\tau_0}g_\alpha(t) \overset{[5]}{=} \mathcal{O}_{\tau_0}\mathcal{F}^{-1}\mathcal{O}_{\nu_0}\mathcal{F}g_\alpha(t) \quad (2.47)$$

and

$$A_z\left(\frac{n}{\nu_0}, \frac{m}{\tau_0}\right) = A_z(2n\tau_0, 2m\nu_0) = 0, \ (m,n) \neq (0,0) \quad (2.48)$$

where the first equality comes from the fact that $\tau_0\nu_0 = \frac{1}{2}$ and the second equality is the straightforward result of time and frequency orthogonalization.

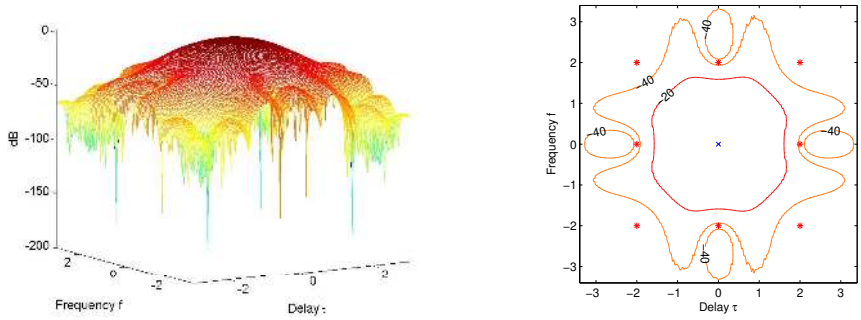

(a) Amplitude [dB] (b) Contour plot [dB]

Figure 2.14: Ambiguity function of IOTA prototype [dB], $\times$ indicates 0 dB and $*$ is approximately $-\infty$ dB or 0 in linear scale.

As $y_\alpha = \mathcal{O}_{\tau_0} g_\alpha$ is even, $\mathcal{F} y_\alpha = \mathcal{F}^{-1} y_\alpha$. Recall the Fourier transform invariant property of Gaussian displayed in (2.42), and apply it to z_{α,ν_0,τ_0}

$$\begin{aligned} \mathcal{F} z_{\alpha,\nu_0,\tau_0} &= \mathcal{F}\mathcal{F}^{-1}\mathcal{O}_{\nu_0}\mathcal{F} y_\alpha = \mathcal{O}_{\nu_0}\mathcal{F} y_\alpha = \mathcal{O}_{\nu_0}\mathcal{F}^{-1} y_\alpha \\ &= \mathcal{O}_{\nu_0}\mathcal{F}^{-1}\mathcal{O}_{\tau_0} g_\alpha = \mathcal{O}_{\nu_0}\mathcal{F}^{-1}\mathcal{O}_{\tau_0}\mathcal{F} g_{1/\alpha} = z_{1/\alpha,\tau_0,\nu_0} \end{aligned} \tag{2.49}$$

Let $\alpha = 1$, $\tau_0 = \nu_0 = \frac{1}{\sqrt{2}}$ and define $\zeta(t) = z_{1,\frac{1}{\sqrt{2}},\frac{1}{\sqrt{2}}}(t)$, then we have

$$\mathcal{F}\zeta = \mathcal{F} z_{1,\frac{1}{\sqrt{2}},\frac{1}{\sqrt{2}}} = z_{1,\frac{1}{\sqrt{2}},\frac{1}{\sqrt{2}}} = \zeta \tag{2.50}$$

Thus ζ is identical to its Fourier transform, as shown in Fig. 2.13, and has nearly isotropic support over the whole time-frequency plane, as shown in Fig. 2.14. This is the reason why it is named IOTA function.

Extended Gaussian Function (EGF)

It is shown [5, 6] that the function z_{α,ν_0,τ_0} which is generated by the algorithmic approach described in (2.47) has a closed-form analytical expression[10]

$$z_{\alpha,\nu_0,\tau_0}(t) = \frac{1}{2}\left[\sum_{k=0}^{\infty} d_{k,\alpha,\nu_0}\left[g_\alpha(t+\frac{k}{\nu_0}) + g_\alpha(t-\frac{k}{\nu_0})\right]\right]\sum_{l=0}^{\infty} d_{l,1/\alpha,\tau_0}\cos\left(2\pi l\frac{t}{\tau_0}\right) \tag{2.51}$$

where $\tau_0\nu_0 = \frac{1}{2}$, $0.528\nu_0^2 \leq \alpha \leq 7.568\nu_0^2$, g_α is the Gaussian function, and the coefficients d_{k,α,ν_0} are real valued and can be computed via the rules described in [5,

[10] A general expression with $\tau_0\nu_0 = \frac{1}{2n}$, $n \in \mathbb{N}$ is omitted since $n > 1$ is not interesting for practical usage due to high lattice density requirement.

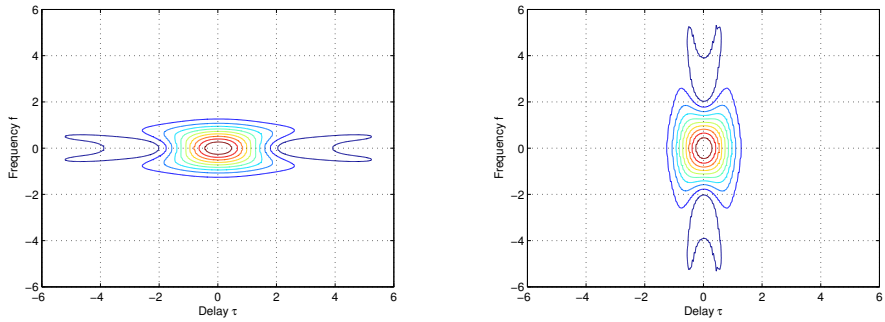

(a) $\alpha = 0.5$ (b) $\alpha = 2$

Figure 2.15: Ambiguity function of EGF prototype, contour plot.

6], which are summarised in Appendix 2.6 E. This family of functions are named as Extended Gaussian Function (EGF) as they are derived from the Gaussian function. The IOTA function ζ is therefore a special case of EGF and its properties such as orthogonality and good time frequency localization are shared with EGF functions. The contour plots for the ambiguity function of EGF prototypes with Gaussian parameter $\alpha = 0.5$ and $\alpha = 2$ are shown in Fig. 2.15.

In practice, as reported in [5], the infinite summation in EGF can be truncated to fifty or even fewer terms while keeping excellent orthogonality and TFL. An approximation of EGF with a few terms is also possible while the trade-off between localization and orthogonality has to be sought.

TFL1

EGF and IOTA functions, which have good TFL properties, spread their pulse shapes over several symbol durations even after truncation. This costs modulation/demodulation delay and complexity. In order to find prototype functions that have limited time duration, say only one symbol long, and meanwhile have satisfactory TFL property, EGF functions are truncated into only one symbol long and used as a basis function for optimisation [30, 31], as shown in Fig. 2.16. Since the optimisation is carried out to maximise the TFL property and the resulting prototype function has only 1 symbol duration and therefore 1-tap coefficient on each sub-carrier in filterbank implementation, it is referred as TFL1 from here on.

TFL parameters ξ and κ

To compare the localization property of different pulses and have a quantitative idea about it, the Heisenberg parameter ξ and the direction parameter κ for each pulse is calculated. The following parameters are used for calculation: 12 time and frequency shifts, i.e., $t \in [-6\tau_0, 6\tau_0]$ and $f \in [-6\nu_0, 6\nu_0]$, with 32 samples per time

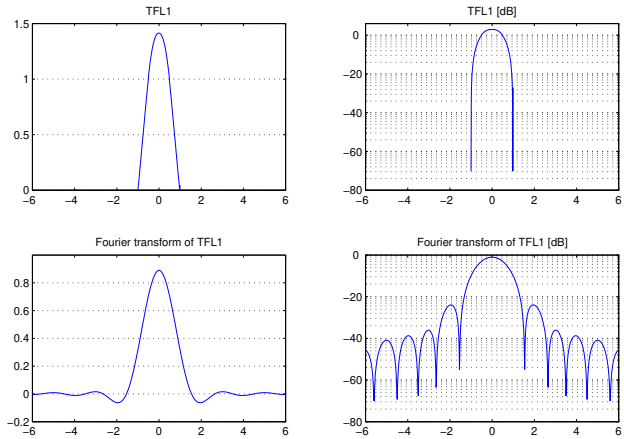

Figure 2.16: TFL1 function and its Fourier transform.

and frequency shift.

	Rect	cosine	IOTA	Gauss	EGF($\alpha = 2$)	TFL1
ξ	0.346	0.886	0.977	1.00	0.874	0.908
κ	0.245	0.728	1.00	1.00	0.572	0.744

Note that for the rectangular pulse, $\Delta f^2 = \int \sin^2(wf)df = \infty$ and therefore $\xi = 0$ and $\kappa = 0$ in theory. For EGF pulse, $\xi(\alpha) = \xi(1/\alpha)$ and it will steadily increase to its maximum as α approaches 1 from either direction [5]. The Gauss pulse achieves the maximum of ξ and therefore has the best TFL property. The IOTA pulse shows good localization which is the maximum of ξ among the EGF functions.

2.6 Appendix

A. Relation between $H(\tau,\nu)$ and $S_h(\tau,\nu)$

By taking the two dimensional autocorrelation function of $H(\tau,\nu)$, we get

$$\begin{aligned}
\mathrm{E}[H(\tau_1,\nu_1)H^*(\tau_2,\nu_2)] &= \mathrm{E}[\int h(\tau_1,t_1)e^{-j2\pi\nu_1 t_1}dt_1 \int h^*(\tau_2,t_2)e^{j2\pi\nu_2 t_2}dt_2] \\
&= \iint \mathrm{E}[h(\tau_1,t_1)h^*(\tau_2,t_2)]e^{-j2\pi(\nu_1 t_1-\nu_2 t_2)}dt_1dt_2 \\
/\text{apply (2.6)}/ &= \iint \phi_h(\tau_1,t_1-t_2)\delta(\tau_1-\tau_2)e^{-j2\pi(\nu_1 t_1-\nu_2 t_2)}dt_1dt_2 \\
/\text{Set } \Delta t = t_1-t_2/ &= \iint \phi_h(\tau_1,\Delta t)\delta(\tau_1-\tau_2)e^{-j2\pi\nu_1\Delta t}d\Delta t\, e^{-j2\pi(\nu_1-\nu_2)t_2}dt_2 \\
/\text{apply (2.7)}/ &= S_h(\tau_1,\nu_1)\delta(\tau_1-\tau_2)\int e^{-j2\pi(\nu_1-\nu_2)t_2}dt_2 \\
&= S_h(\tau_1,\nu_1)\delta(\tau_1-\tau_2)\delta(\nu_1-\nu_2)
\end{aligned}$$

where the last equality from the definition of $\delta(x)$.

B. RMS Doppler spread under the exp-U channel model

According to (2.9), the Doppler power spectrum can be written as

$$P_d(f) = \frac{1}{\pi f_D\sqrt{1-(\frac{f}{f_D})^2}}, \quad |f| \le f_D \tag{2.52}$$

As $P_d(f)$ is an even function, it is easy to find that

$$\bar{f}_d = \frac{\int_{-f_D}^{f_D} fP_d(f)df}{\int_{-f_D}^{f_D} P_d(f)df} = 0 \tag{2.53}$$

Therefore the RMS Doppler spread

$$\begin{aligned}
f_{\text{RMS}} &= \sqrt{\frac{\int_{-f_D}^{f_D}(f-\bar{f}_d)^2P_d(f)df}{\int_{-f_D}^{f_D}P_d(f)df}} = \sqrt{\frac{\int_{-f_D}^{f_D}f^2P_d(f)df}{\int_{-f_D}^{f_D}P_d(f)df}} \\
&= \sqrt{\frac{\int_{-f_D}^{f_D} f^2/\sqrt{1-(\frac{f}{f_D})^2}df}{\int_{-f_D}^{f_D} 1/\sqrt{1-(\frac{f}{f_D})^2}df}} = f_D\sqrt{\frac{\int_0^{\pi/2}\frac{\sin^2\theta}{\cos\theta}d\sin\theta}{\int_0^{\pi/2}\frac{1}{\cos\theta}d\sin\theta}} \\
&= f_D\sqrt{\frac{\int_0^{\pi/2}\sin^2\theta d\theta}{\pi/2}} = \frac{\sqrt{2}}{2}f_D
\end{aligned} \tag{2.54}$$

where the fourth equality comes from variable substitution by $\sin\theta = f/f_D$ and the last equality comes from the fact that $\int_0^{\pi/2}\sin^2\theta d\theta = \pi/4$.

C. Ambiguity function for rectangular, halfcosine and Gaussian

The cross-ambiguity function for $g(t)$ and $q(t)$ can be written as

$$A_{g,q}(\tau,\nu)=\int_{\mathbb{R}} g(t+\tau/2)q^*(t-\tau/2)e^{-j2\pi\nu t}dt=\begin{cases}\int_{\Omega_\tau} e^{-j2\pi\nu t}dt & ,|\tau|<\frac{T_0+T}{2}\\ 0 & ,|\tau|\geq\frac{T_0+T}{2}\end{cases} \quad (2.55)$$

where

$$\Omega_\tau=\{t|-\frac{T}{2}\leq t+\frac{\tau}{2}\leq\frac{T}{2},\ -\frac{T_0}{2}\leq t-\frac{\tau}{2}\leq\frac{T_0}{2},\ |\tau|<\frac{T_0+T}{2}\}$$

is the intergartion interval dependent on the value of τ. After careful arrangement, the above equation can be written as

$$\Omega_\tau=\begin{cases}\{t|-\frac{T}{2}-\frac{\tau}{2}\leq t\leq\frac{T}{2}-\frac{\tau}{2}\},|\tau|\leq\frac{T_0-T}{2}\\ \{t|-\frac{T_0}{2}+\frac{\tau}{2}\leq t\leq\frac{T}{2}-\frac{\tau}{2}\},\frac{T_0-T}{2}<\tau<\frac{T_0+T}{2}\\ \{t|-\frac{T}{2}-\frac{\tau}{2}\leq t\leq\frac{T_0}{2}+\frac{\tau}{2}\},-\frac{T_0+T}{2}<\tau<-\frac{T_0-T}{2}\end{cases} \quad (2.56)$$

On the other hand, we have

$$\int_a^b e^{-j2\pi\nu t}dt=\frac{e^{-j2\pi\nu a}-e^{-j2\pi\nu b}}{j2\pi\nu}=e^{-j\pi\nu(a+b)}\frac{\sin\pi\nu(b-a)}{\pi\nu} \quad (2.57)$$

By applying (2.57) and (2.56) into (2.55), we get

$$A_{g,q}(\tau,\nu)=\begin{cases}e^{j\pi\nu\tau}\frac{\sin\pi\nu T}{\pi\nu T}, & |\tau|\leq\frac{T_0-T}{2}\\ e^{j\pi\nu(T_0-T)/2}\frac{\sin\left[\pi\nu(\frac{T+T_0}{2}-\tau)\right]}{\pi\nu T}, & \frac{T_0-T}{2}<\tau<\frac{T_0+T}{2}\\ e^{j\pi\nu(T-T_0)/2}\frac{\sin\left[\pi\nu(\frac{T+T_0}{2}+\tau)\right]}{\pi\nu T}, & -\frac{T_0+T}{2}<\tau<-\frac{T_0-T}{2}\\ 0, & |\tau|\geq\frac{T_0+T}{2}\end{cases} \quad (2.58)$$

By replacing q with q and T_0 with T in (2.58), we get

$$A_g(\tau,\nu)=\begin{cases}\frac{\sin\left[\pi\nu T\left(1-\frac{|\tau|}{T}\right)\right]}{\pi\nu T} & ,|\tau|<T\\ 0 & ,|\tau|\geq T\end{cases}$$

For the halfcosine function defined in (2.38), following the same method we have

$$A_g(\tau,\nu)=\begin{cases}\int_{-\tau_0+\frac{|\tau|}{2}}^{\tau_0-\frac{|\tau|}{2}}\cos\frac{\pi(t-\tau/2)}{2\tau_0}\cos\frac{\pi(t+\tau/2)}{2\tau_0}e^{-j2\pi\nu t}dt, & |\tau|<2\tau_0\\ 0, & |\tau|\geq 2\tau_0\end{cases} \quad (2.59)$$

The integration in the above equation can be written as

$$\begin{aligned}
&\int_a^b \cos\frac{\pi(t+\tau/2)}{2\tau_0} e^{-j2\pi\nu t}dt = \frac{1}{2}\int_a^b \left[\cos\frac{\pi t}{\tau_0} + \cos\frac{\pi\tau}{2\tau_0}\right] e^{-j2\pi\nu t}dt \\
&= \frac{1}{4}\int_a^b \left[e^{j\frac{\pi t}{\tau_0}} + e^{-j\frac{\pi t}{\tau_0}}\right] e^{-j2\pi\nu t}dt + \frac{1}{2}\int_a^b \cos\frac{\pi\tau}{2\tau_0} e^{-j2\pi\nu t}dt \\
&= \frac{1}{4}\int_a^b e^{-j2\pi(\nu-\frac{1}{2\tau_0})}dt + \frac{1}{4}\int_a^b e^{-j2\pi(\nu+\frac{1}{2\tau_0})}dt + \frac{1}{2}\int_a^b \cos\frac{\pi\tau}{2\tau_0} e^{-j2\pi\nu t}dt
\end{aligned} \tag{2.60}$$

By applying (2.57) and (2.60) into (2.59), we have

$$A_g(\tau,\nu) = \begin{cases} \dfrac{\sin\pi(1-2\tau_0\nu)(1-\frac{|\tau|}{2\tau_0})}{2\pi(1-2\tau_0\nu)} + \dfrac{\sin\pi(1+2\tau_0\nu)(1-\frac{|\tau|}{2\tau_0})}{2\pi(1+2\tau_0\nu)} \\ \qquad + \dfrac{\cos\frac{\pi\tau}{2\tau_0}\sin 2\pi\tau_0\nu(1-\frac{|\tau|}{2\tau_0})}{2\pi\tau_0\nu}, & |\tau| < 2\tau_0 \\ 0, & |\tau| \geq 2\tau_0 \end{cases}$$

For Gaussian prototype, we have

$$\begin{aligned}
A_{g_\alpha}(\tau,\nu) &= \sqrt{2\alpha}\int_{-\infty}^{\infty} e^{-\pi\alpha(t-\tau/2)^2} e^{-\pi\alpha(t+\tau/2)^2} e^{-j2\pi\nu t}dt \\
&= \sqrt{2\alpha}\int_{-\infty}^{\infty} e^{-\pi\alpha(2t^2+\tau^2/2)-j2\pi\nu t}dt \\
&= \sqrt{2\alpha}e^{-\frac{\pi}{2}\alpha\tau^2}\int_{-\infty}^{\infty} e^{-2\pi\alpha t^2-j2\pi\nu t}dt \\
&= \sqrt{2\alpha}e^{-\frac{\pi}{2}\alpha\tau^2}\frac{1}{\sqrt{2\alpha}}e^{-\frac{\pi}{2}\frac{\nu^2}{\alpha}} \\
&= e^{-\frac{\pi}{2}(\alpha\tau^2+\frac{1}{\alpha}\nu^2)}
\end{aligned} \tag{2.61}$$

where the fourth equality comes from (2.43).

D. Proof of orthogonalization operator $\mathcal{O}_a$

Apply the Fourier transform operator $\mathcal{F}$ to (2.30) and set the time parameter $\tau = 0$, we get

$$A_y(0,\nu) = \mathcal{F}\{\gamma_y(0,t)\} = \mathcal{F}\left\{|y(t)|^2\right\}. \tag{2.62}$$

Construct an infinite summation regarding $y(t) = \mathcal{O}_a x(t)$ that is given by (2.44), we get

$$\begin{aligned}\sum_{m=-\infty}^{\infty} a\gamma_y(0, t-ma) &= a\sum_{m=-\infty}^{\infty} |y(t-ma)|^2 \\ &= \sum_{m=-\infty}^{\infty} \frac{|x(t-ma)|^2}{\sqrt{\sum_{k=-\infty}^{\infty} |x(t-ka-ma)|^2 \sum_{l=-\infty}^{\infty} |x(t-la-ma)|^2}}\end{aligned} \tag{2.63}$$

where

$$\sum_{k=-\infty}^{\infty} |x(t-ka-ma)|^2 = \sum_{l=-\infty}^{\infty} |x(t-la-ma)|^2 = \sum_{p=-\infty}^{\infty} |x(t-pa)|^2 \tag{2.64}$$

whose value is only depending on the function x, time instance t and the positive factor a, and therefore has nothing to do with the summation index (no matter whether m, or k, l, etc. is used). This simplifies (2.63) and the summation now becomes

$$\sum_{m=-\infty}^{\infty} a\gamma_y(0, t-ma) = \sum_{m=-\infty}^{\infty} \frac{|x(t-ma)|^2}{\sum_{p=-\infty}^{\infty} |x(t-pa)|^2} = \frac{\sum_{m=-\infty}^{\infty} |x(t-ma)|^2}{\sum_{p=-\infty}^{\infty} |x(t-pa)|^2} = 1 \tag{2.65}$$

By introducing the Dirac's delta function $\delta(t)$ and the convolution operator $*$, (2.65) can be rewritten as

$$\sum_{m=-\infty}^{\infty} a\gamma_y(0, t-ma) = \sum_{m=-\infty}^{\infty} a\delta(t-ma) * \gamma_y(0, t) = 1 \tag{2.66}$$

Apply the Fourier transform on both sides and notice that [33]

$$\begin{aligned}\mathcal{F}\left\{\sum_{m=-\infty}^{\infty} \delta(t-ma)\right\} &= \frac{1}{a}\sum_{m=-\infty}^{\infty} \delta\left(\nu - \frac{m}{a}\right),\ a > 0 \\ \mathcal{F}\{1\} &= \delta(\nu) \\ \mathcal{F}\{x(t) * y(t)\} &= X(\nu)Y(\nu)\end{aligned} \tag{2.67}$$

we get

$$\sum_{m=-\infty}^{\infty} \delta\left(\nu - \frac{m}{a}\right) A_y(0, \nu) = \delta(\nu) \tag{2.68}$$

which gives out straightforward $A_y(0,0) = 1$ and $A_y(0, \frac{m}{a}) = 0\ \forall m \neq 0$. Q.E.D.

E. Calculation of EGF coefficients

According to [5], the coefficients d_{k,α,ν_0} can be expressed as

$$\begin{aligned} d_{k,\alpha,\nu_0} &= \sum_{l=0}^{\infty} a_{k,l}\, e^{-\frac{\alpha\pi l}{2\nu_0^2}},\ 0 \le k \le \infty \\ &\approx \sum_{j=0}^{j_l} b_{k,j}\, e^{-\frac{\alpha\pi}{2\nu_0^2}(2j+k)},\ 0 \le k \le K \end{aligned} \tag{2.69}$$

where $j_l = \lfloor (K-k)/2 \rfloor$ and K is a positive integer which insure an accuracy of $e^{-\frac{\pi\alpha K}{2\nu_0^2}}$ for the approximation due to truncation of the infinite summation. A list of coefficients $b_{k,j}$ corresponding to $K = 14$, which leads to an accuracy of 10^{-19} for $\alpha = 1$, is present in the following table.

b	j (0 to 7)							
k 0 to 14	1	$\frac{3}{4}$	$\frac{105}{64}$	$\frac{675}{256}$	$\frac{76233}{16384}$	$\frac{457107}{65536}$	$\frac{12097169}{1048576}$	$\frac{13774755}{4194304}$
	-1	$-\frac{15}{8}$	$-\frac{219}{64}$	$-\frac{6055}{1024}$	$-\frac{161925}{16384}$	$-\frac{2067909}{131072}$	$-\frac{26060847}{1048576}$	
	$\frac{3}{4}$	$\frac{19}{16}$	$\frac{1545}{512}$	$\frac{9765}{2048}$	$\frac{596277}{65536}$	$\frac{3679941}{262144}$	$-\frac{105421227}{16777216}$	
	$-\frac{5}{8}$	$-\frac{123}{128}$	$-\frac{2289}{1024}$	$-\frac{34871}{8192}$	$-\frac{969375}{131072}$	$-\frac{51182445}{4194304}$		
	$\frac{35}{64}$	$\frac{213}{256}$	$\frac{7797}{4096}$	$\frac{56163}{16384}$	$\frac{13861065}{2097152}$	$-\frac{139896345}{8388608}$		
	$-\frac{63}{128}$	$-\frac{763}{1024}$	$-\frac{13875}{8192}$	$-\frac{790815}{262144}$	$-\frac{23600537}{4194304}$			
	$\frac{231}{512}$	$\frac{1395}{2048}$	$\frac{202281}{131072}$	$\frac{1434705}{524288}$	$-\frac{142044345}{16777216}$			
	$-\frac{429}{1024}$	$-\frac{20691}{32768}$	$-\frac{374325}{262144}$	$-\frac{5297445}{2097152}$				
	$\frac{6435}{16384}$	$\frac{38753}{65536}$	$\frac{1400487}{1048576}$	$-\frac{1458219}{4194304}$				
	$-\frac{12155}{32768}$	$-\frac{146289}{262144}$	$-\frac{2641197}{2097152}$					
	$\frac{46189}{131072}$	$\frac{277797}{524288}$	$\frac{20050485}{16777216}$					
	$-\frac{88179}{262144}$	$-\frac{2120495}{4194304}$						
	$\frac{676039}{2097152}$	$\frac{4063017}{8388608}$						
	$-\frac{1300075}{4194304}$							
	$\frac{5014575}{16777216}$							

As for coefficients $d_{k,1/\alpha,\tau_0}$, the dual form of d_{k,α,ν_0}, it is easy to calculate them just by replacing the corresponding items and following the procedure above.

Chapter 3

Pulse Shape Adaptation for GFDM Systems

3.1 Introduction

Adaptation is crucial to realise high data rate transmission in multicarrier communication systems over dispersive channels. Apart from rate/power adaptation enabled by OFDM, GFDM systems provide possibility to adjust pulse shapes depending on the channel characteristics. Among other famous pulse functions, the EGF function is well known for its localisation variation in the time-frequency plane. Therefore it plays a vital role in pulse shape adaptation in the following discussion. Besides, adjustment of other parameters, such as sampling frequency, sub-carrier separation bandwidth, etc., will also change the overall performance largely. The purpose of this chapter is to investigate pulse shape adaptivity in GFDM systems to see how it can affect the performance over doubly dispersive channels.

3.2 Previous work

In [4,9,10] it was proposed that the pulse shape should be well localized in time and in frequency with the same time-frequency scale as the channel itself so that the resulting ISI/ICI will be minimized. If a uniformly distributed or an elliptical scattering function is assumed for the channel, the optimal pulse shape should satisfy the condition stated in (2.25). In [14] it was pointed out that the orthogonalised Gaussian functions are good candidates for pulse shape adaptation based on the above rule. For more general scattering functions, various optimisation methods have been proposed based on different objective function formulations. For example, maximising the desired signal energy is proposed in [9], and minimising the joint ISI/ICI power is proposed in [34] for pulse shaped multicarrier systems and in [15] for hexagonal multicarrier systems. Maximising the signal to interference ratio is also considered in [34]. However, as pointed in [35], the problem of max-

imising the desired signal energy, and therefore also the problem of minimising the joint ISI/ICI power, is in general non-convex. Only for very special scattering functions this problem have closed form solutions. For example for channels with a Gaussian scattering function, the optimal pulse shape is also Gaussian. With the aid of power series expansion with proper truncation, one can find analytically some sub-optimal solutions. Therefore proper numerical solutions have to be found to enable efficient pulse shape adaptation.

3.3 Practical adaptation strategies

Recall the block diagram of an FDM system shown in Fig. 2.1, the equivalent lowpass channel transfer function between the k_{th} sub-channel at the transmitter side and the l_{th} sub-channel at the receiver side can be written as

$$\tilde{H}_{l,k}(f) = G(f-kF)H(f)G^*(f+lF) = \begin{cases} H(f)|G(f)|^2, & k=l \\ H(f)G(f-kF)G^*(f+lF), & \text{otherwise} \end{cases}$$

where $G(f)$ is the Fourier transform of the pulse shape prototype $g(t)$. To preserve the transmitted signal as good as possible, the pulse shape whose overall power spectrum $|G(f)|^2$ has a narrow main lobe with flat top and low side lobe with fast decay property will be optimal to minimize the interference from neighboring sub-channels. Unfortunately it is not realistic as such a band limited function will have a large spread in time domain, which means a considerably long filter or large truncation error. Fig. 3.1 shows the spectrum amplitude $|G(f)|$ for the rectangular function, the half cosine function and its dual RRC ($\rho = 1$ is used here), and EGF functions with $\alpha = 1$ and $\alpha = 2$. The frequency response of the EGF functions can be easily adjusted by changing the Gaussian parameter α and therefore it plays an important role in our following discussion.

In this section we will first review the TFL property of EGF functions and then formulate some objective functions for optimisation. Practical adaptation strategies as well as performance and complexity trade-offs will be discussed.

TFL property of EGF pulse shapes

Among other famous pulse functions, the EGF [6] is well known for its localisation variation in the time-frequency plane. Therefore it plays a vital role in pulse shape adaptation in the following discussion.

For EGF functions with $\frac{\tau_0}{T} = \sqrt{\frac{1}{2\lambda}}$ and $\frac{\nu_0}{F} = \sqrt{\frac{\lambda}{2}}$, where $\lambda > 0$ is a constant scaling factor, it can be proved that (see the Appendix 3.4 A.)

$$\xi(\alpha) = \xi(\frac{\lambda^2}{\alpha}),\ \kappa(\alpha)\kappa(\frac{\lambda^2}{\alpha}) = \frac{1}{\lambda^2} \tag{3.1}$$

The variation of ξ and κ with respect to α for EGF functions with $\lambda = 1$ ($\frac{\tau_0}{T} = \frac{\nu_0}{F} = \frac{\sqrt{2}}{2}$) and $\lambda = 2$ ($\frac{\tau_0}{T} = \frac{1}{2}$, $\frac{\nu_0}{F} = 1$) is shown in Fig. 3.2, in which τ_0 and ν_0

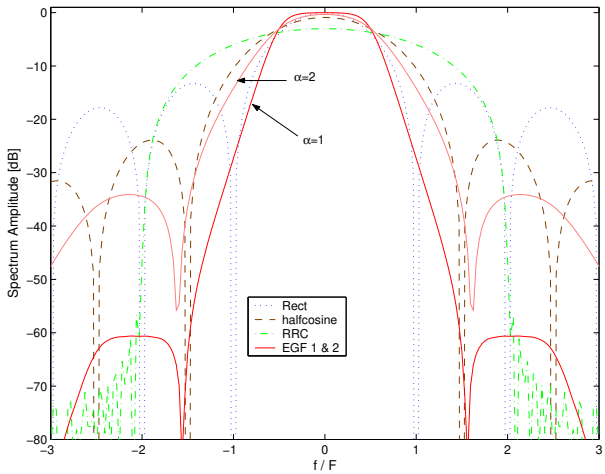

Figure 3.1: Pulse shape spectrum.

are normalised by T and F, respectively for convenience. By just increasing the Gaussian parameter, the time-frequency scale (the value of κ) changes continuously: from a mostly time-axis stretched pulse to a mostly frequency-axis stretched pulse. Compared to the case with $\frac{\tau_0}{T} = \frac{\nu_0}{F} = \frac{\sqrt{2}}{2}$, the EGF function with $\frac{\tau_0}{T} = \frac{1}{2}$ have larger variation of κ and better stability of ξ, which makes it more suitable for pulse shape adaptation. The Gaussian function, however, will not be taken into consideration since it will introduce large intrinsic distortion after reconstruction and therefore cause difficulty in demodulation.

If the value of κ is calculated with normalised τ_0 and ν_0 (by T and F respectively) as in Fig. 3.2, the adaptation rule for rectangular lattice stated in (2.25) can be rewritten as

$$\kappa(\alpha) = \frac{\Delta t}{\Delta f} \propto \frac{\tau_{\mathrm{RMS}}/T}{f_D/F} = \frac{\tau_{\mathrm{RMS}}}{f_D}(\frac{F_s}{N})^2 \tag{3.2}$$

where τ_{RMS} is the RMS delay spread and f_D is the maximum Doppler shift, and the last equality comes from the fact that $F = 1/T = F_s/N$. Therefore, for each specific channel realisation (i.e. $\frac{\tau_{\mathrm{RMS}}}{f_D}$ is determined), the performance against delay and Doppler dispersion depends on the bandwidth F and the direction parameter κ. We can adjust these two parameters to improve the system performance. When the sampling frequency F_s is fixed in some instance, the FFT size N will be subject to adaptation since $F = \frac{F_s}{N}$. The relationship stated in (3.1) can therefore be used in pulse shape adaptation to help select the proper α.

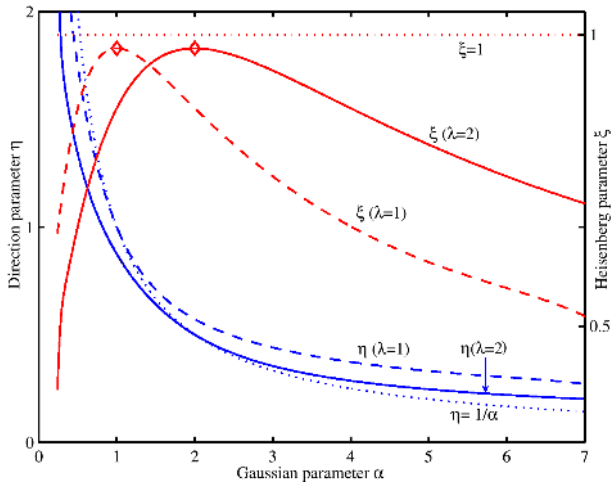

Figure 3.2: TFL parameters (ξ,κ) for EGF with $\lambda = 1$ (dashed line), $\lambda = 2$ (solid line). TFL for the Gaussian function (dotted line) is plotted as reference.

Objective function formulation

Following the system model defined in Chapter 2 and without loss of generality, we assume symbol $a_{0,0}$ is to be detected,

$$\begin{aligned} \hat{a}_{0,0} &=< r(t), g_{0,0}(t) >= \int r(t) g_{0,0}^{*}(t) dt \\ &= \iiint H(\nu,\tau) \sum_{m,n} a_{m,n} g_{m,n}(t-\tau) g_{0,0}^{*}(t) e^{j2\pi\nu t} dt d\nu d\tau \end{aligned} \tag{3.3}$$

where $r(t)$ is the same as defined in (2.5) but with with the noise component omitted for simplicity.

For a GFDM system with a rectangular lattice $\Lambda = \begin{bmatrix} \tau_0 & 0 \\ 0 & \nu_0 \end{bmatrix}$, assume the signal basis is formulated from a prototype function $g(t)$ in the way

$$g_{m,n}(t) = g(t - n\tau_0) e^{j2\pi m\nu_0 t}$$

the inner product of the two signal bases in (3.3) can be written as

$$\begin{aligned}
&\int g_{m,n}(t-\tau)g^*_{0,0}(t)e^{j2\pi\nu t}dt = \int g(t-n\tau_0-\tau)g^*(t)e^{j2\pi[m\nu_0(t-\tau)+\nu t]}dt \\
&= e^{-j2\pi m\nu_0\tau}\int g(t-n\tau_0-\tau)g^*(t)e^{j2\pi(m\nu_0+\nu)t}dt \\
&= e^{-j2\pi m\nu_0\tau}\int g(t'-\frac{n\tau_0+\tau}{2})g^*(t'+\frac{n\tau_0+\tau}{2})e^{j2\pi(m\nu_0+\nu)t'}e^{j\pi(m\nu_0+\nu)(n\tau_0+\tau)}dt' \\
&= e^{-j2\pi m\nu_0\tau}e^{j\pi(m\nu_0+\nu)(n\tau_0+\tau)}A^*_g(n\tau_0+\tau,m\nu_0+\nu) \\
&= e^{j\pi mn\nu_0\tau_0}e^{j\pi(n\tau_0\nu-m\nu_0\tau+\nu\tau)}A^*_g(n\tau_0+\tau,m\nu_0+\nu)
\end{aligned} \tag{3.4}$$

where the third equality comes from variable substitution by $t = t' + \frac{n\tau_0+\tau}{2}$ and the fourth equality comes from the definition of $A_g(\tau,\nu)$ which is defined in (2.30). Substitute (3.4) into (3.3), we get

$$\begin{aligned}
\hat{a}_{0,0} &= \sum_{m,n} a_{m,n}e^{j\pi mn\nu_0\tau_0}\iint H(\tau,\nu)A^*_g(n\tau_0+\tau,m\nu_0+\nu)e^{j\pi(n\tau_0\nu-m\nu_0\tau+\nu\tau)}d\nu d\tau \\
&= S_{0,0} + I_{0,0}
\end{aligned} \tag{3.5}$$

where $S_{0,0}$ is the desired signal part with expression

$$S_{0,0} = a_{0,0}\iint H(\tau,\nu)A^*_g(\tau,\nu)e^{j\pi\tau\nu}d\nu d\tau \tag{3.6}$$

and $I_{0,0}$ is the joint ISI/ICI part introduced both by the channel dispersion and the imperfectness of the reconstruction, which can be written as

$$I_{0,0} = \sum_{(m,n)\neq(0,0)} a_{m,n}e^{j\pi mn\nu_0\tau_0}\iint H(\tau,\nu)A^*_g(n\tau_0+\tau,m\nu_0+\nu)e^{j\pi(n\tau_0\nu-m\nu_0\tau+\nu\tau)}d\nu d\tau \tag{3.7}$$

Assume all the transmitted symbols are independent with uniform energy, i.e.,

$$\mathrm{E}\{a_{m,n}a^*_{m',n'}\} = \delta_{mm'}\delta_{nn'} = \begin{cases} 1, & m=m' \text{and n=n'} \\ 0, & \text{otherwise} \end{cases} \tag{3.8}$$

the energy of the desired signal part $S_{0,0}$ after passing through a WSSUS channel can be written as

$$\begin{aligned}
E_S = \mathrm{E}\{S_{0,0}S^*_{0,0}\} &= \mathrm{E}\{\iiiint H(\tau,\nu)H^*(\nu,\tau)A_g(\tau,\nu)A^*_g(\tau,\nu)e^{j\pi(\tau\nu-\tau'\nu')}d\nu d\tau d\nu' d\tau'\} \\
&= \iiiint \mathrm{E}\{H(\nu,\tau)H^*(\tau,\nu)\}|A_g(\tau,\nu)|^2e^{j\pi(\tau\nu-\tau'\nu')}d\nu d\tau d\nu' d\tau' \\
&= \iiiint S_h(\tau,\nu)\delta(\tau-\tau')\delta(\nu-\nu')|A_g(\tau,\nu)|^2e^{j\pi(\tau\nu-\tau'\nu')}d\nu d\tau d\nu' d\tau' \\
&= \iint S_h(\tau,\nu)|A_g(\tau,\nu)|^2d\nu d\tau
\end{aligned} \tag{3.9}$$

where the second last equality comes from the property stated in (2.8). Following the same process and using the assumption in (3.8), the energy of the interference part $I_{0,0}$ in can be written as

$$E_I = \mathrm{E}\{I_{0,0} I_{0,0}^*\} = \sum_{(m,n)\neq(0,0)} \iint S_h(\tau,\nu)|A_g(n\tau_0+\tau, m\nu_0+\nu)|^2 d\nu d\tau \quad (3.10)$$

When a hexagonal lattice $\Lambda = \begin{bmatrix} \tau_0 & p\tau_0 \\ 0 & \nu_0 \end{bmatrix}$, $0 < p < 1$ is used instead with

$$g_{m,n} = g(t-(n+pm)\tau_0)e^{j2\pi m\nu_0 t}$$

the inner product of $g_{m,n}$ and $g_{0,0}$ in (3.4) becomes

$$\begin{aligned} &\int g_{m,n}(t-\tau)g_{0,0}^*(t)e^{j2\pi\nu t}dt = \int g[t-(n+pm)\tau_0-\tau]g^*(t)e^{j2\pi[m\nu_0(t-\tau)+\nu t]}dt \\ &= e^{j\pi m(n+pm)\nu_0\tau_0}e^{j\pi[(n+pm)\tau_0\nu - m\nu_0\tau+\nu\tau]}A_g^*((n+pm)\tau_0+\tau, m\nu_0+\nu) \end{aligned} \quad (3.11)$$

The resulting expression for desired signal part $S_{0,0}$ is therefore the same as in (3.6) and the interference part $I_{0,0}$ should be modified accordingly: replace n by $n+pm$ in (3.7) where appropriate. As a consequence, the expression for E_S remains the same and meanwhile the corresponding expression for E_I becomes

$$E_I = \sum_{(m,n)\neq(0,0)} \iint S_h(\tau,\nu)|A_g((n+pm)\tau_0+\tau, m\nu_0+\nu)|^2 d\nu d\tau \quad (3.12)$$

When a hexagonal lattice $\Lambda = \begin{bmatrix} \tau_0 & 0 \\ p\nu_0 & \nu_0 \end{bmatrix}$, $0 < p < 1$ is used with

$$g_{m,n} = g(t-n\tau_0)e^{j2\pi(m+pn)\nu_0 t}$$

the expression for E_I becomes

$$E_I = \sum_{(m,n)\neq(0,0)} \iint S_h(\tau,\nu)|A_g(n\tau_0+\tau, (m+pn)\nu_0+\nu)|^2 d\nu d\tau \quad (3.13)$$

and the expression for E_S remains unchanged. For more general case when the analysis and synthesis prototype functions are not identical, just replace $A_g(\tau,\nu)$ by $A_{g,q}(\tau,\nu)$ where appropriate.

Obviously expressions for E_S and E_I for the rectangular lattice and the hexagonal lattices, which are the same as the energy expressions derived for pulse shaped multicarrier systems [34] and similar to the interference expression for hexagonal multicarrier systems [15] respectively, have the same format and therefore optimisation methods proposed for one case can be directly applied to another without difficulties.

Simple adaptation strategy

Different optimisation methods regarding maximising desired signal energy E_S [9], or minimising interference E_I [15,34], or maximising the signal to interference ratio E_S/E_I [34] are considered. However, as discussed in the Section 3.2, closed form solutions only exist for some special cases. By using power series expansion with proper truncation, one can find analytically some sub-optimal solutions. Therefore numerical solutions are in general needed to find the optimal solution. Without any additional constraint, however, exhaustive searching itself is an "impossible mission" in the context of finding the optimal pulse shape as well as the lattice structure with respect to each channel realisation. Given the good TFL properties of the EGF functions, it will be applied to the objective function for exhaustive searching with a variable quadruplet (α, τ_0, ν_0, p).

As shown in Fig. 3.2, the value of ξ and κ changes continuously and smoothly with increasing α, where a sharp slope for small values of α and relatively small slope for large α is observed. This observation indicates that searching through selected samples rather than the range of α will be sufficient to achieve satisfactory performance, with dense samples picked up for small α and sparse samples for large α according to the relationship revealed in (3.1). The value of τ_0, ν_0 and p can be selected according the rule stated in (2.25) or as stated in [15] to fit the channel dispersion. The resulting optimal choice of the variables (α, τ_0, ν_0, p) for a specific type of channels can then be stored for use in later stages. These optimised quadruplets form a code book for pulse shape adaptation in GFDM systems and the best fitted quadruplet will be selected for transmission and reception as long as the channel information is known.

The performance of a simple pulse shape adaptation strategy based on the selection of α will be demonstrated in Chapter 4 under the context of OFDM/OQAM with a rectangular lattice.

Performance and complexity trade-off

The channel scattering function $S_h(\tau, \nu)$ is not easy to model. Even if the information of a dispersive channel is well observed, any simple expression of $S_h(\tau, \nu)$ will not be good enough to approximate the shape of the channel and therefore introduce ambiguity and uncertainty in the exhaustive searching process. Hence it is worthless to spend too much effort on finding the exact optimal value of the quadruplet (either analytically or numerically) based on the assumption of a certain channel model.

It is therefore a wise choice to build up a code book for adaptation based on certain channel models and then train and verify it with real measured channel data. Since this code book is constructed based on the statistic information $S_h(\tau, \nu)$ of the channel rather than the instantaneous channel impulse response $h(\tau, t)$, such adaptation is robust to channel variations and feedback delay. The larger the code book is, the more suitable quadruplet and therefore better performance will be

achieved. However, too large code book requires large number of feedback bits to the transmitter in order to correctly pick up the corresponding quadruplet for transmission, which will decrease the spectral and power efficiency.

3.4 Appendix

A. Proof of TFL parameters ξ and κ for EGF

Recall the close-form expression of EGF in (2.51) where $d_{k,\alpha,\nu_0} = \sum_{l=0}^{\infty} a_{k,l} e^{\frac{l\pi}{2\nu_0^2}\alpha}$ are real coefficients, and $g_\alpha(t)$ is the Gaussian function. It is easy to figure out the following relationships

$$\begin{aligned} d_{k,\alpha,\nu_0} &\triangleq d_k(\frac{\alpha}{\nu_0^2}) = d_k(\frac{\alpha/\lambda^2}{\nu_0^2/\lambda^2}) = d_{k,\frac{\alpha}{\lambda^2},\nu_0/\lambda} \\ d_{l,1/\alpha,\tau_0} &= d_k(\frac{1/\alpha}{2\tau_0^2}) = d_k(\frac{\lambda^2/\alpha}{2\lambda^2\tau_0^2}) = d_{l,\frac{\lambda^2}{\alpha},\lambda\tau_0} \\ g_\alpha(t) &= (\lambda^2)^{1/4}(2\frac{\alpha}{\lambda^2})^{1/4} e^{-\pi\frac{\alpha}{\lambda^2}(\lambda t)^2} = \sqrt{\lambda} g_{\frac{\alpha}{\lambda^2}}(\lambda t) \\ g_\alpha(t + k/\nu_0) &= \sqrt{\lambda} g_{\frac{\alpha}{\lambda^2}}(\lambda t + \frac{k}{\nu_0/\lambda}) \end{aligned} \tag{3.14}$$

where $\lambda > 0$ is a constant scaling factor. Substitute (3.14) into (2.51), we get

$$z_{\alpha,\nu_0,\tau_0}(t) = \sqrt{\lambda} z_{\frac{\alpha}{\lambda^2},\frac{\nu_0}{\lambda},\lambda\tau_0}(\lambda t) \tag{3.15}$$

For EGF and Gaussian functions, as shown in [6], their Fourier transforms have the same shape as themselves

$$\mathcal{F}\{z_{\alpha,\nu_0,\tau_0}(t)\} = z_{\frac{1}{\alpha},\tau_0,\nu_0}(f), \quad \mathcal{F}\{g_\alpha(f)\} = g_{1/\alpha}(f) \tag{3.16}$$

where $\mathcal{F}$ is the Fourier Transform operator.

In the following, we will normalise τ_0 and ν_0 by T and F respectively to simplify calculation and system integration. Set $\frac{\tau_0}{T} = \sqrt{\frac{1}{2\lambda}}$, $\frac{\nu_0}{F} = \sqrt{\frac{\lambda}{2}}$, then the notation of the pulse shaping prototype function can be written as

$$x_\alpha(t) = z_{\alpha,\frac{\nu_0}{F},\frac{\tau_0}{T}}(t) = z_{\alpha,\sqrt{\frac{\lambda}{2}},\sqrt{\frac{1}{2\lambda}}}(t) \tag{3.17}$$

Apply (3.15) into (3.17), we get

$$x_\alpha(t) = \sqrt{\lambda} z_{\frac{\alpha}{\lambda^2},\sqrt{\frac{1}{2\lambda}},\sqrt{\frac{\lambda}{2}}}(\lambda t) \tag{3.18}$$

and its Fourier transform

$$\begin{aligned} X_\alpha(f) &= \mathcal{F}\{x_\alpha\} = \sqrt{\lambda}\int e^{-j2\pi ft} z_{\frac{\alpha}{\lambda^2},\sqrt{\frac{1}{2\lambda}},\sqrt{\frac{\lambda}{2}}}(\lambda t)dt \\ &= \frac{\sqrt{\lambda}}{\lambda}\int e^{-j2\pi\frac{f}{\lambda}\tau} z_{\frac{\alpha}{\lambda^2},\sqrt{\frac{1}{2\lambda}},\sqrt{\frac{\lambda}{2}}}(\tau)d\tau \\ &= \frac{\sqrt{\lambda}}{\lambda} Z_{\frac{\alpha}{\lambda^2},\sqrt{\frac{1}{2\lambda}},\sqrt{\frac{\lambda}{2}}}(\frac{f}{\lambda}) \\ &= \frac{\sqrt{\lambda}}{\lambda} z_{\frac{\lambda^2}{\alpha},\sqrt{\frac{\lambda}{2}},\sqrt{\frac{1}{2\lambda}}}(\frac{f}{\lambda}) \end{aligned} \tag{3.19}$$

where the third equality comes from variable substitution by $\tau = \lambda t$ and the last equality comes from (3.16). On the other hand, we have

$$\begin{aligned} x_{\frac{\lambda^2}{\alpha}}(t) &= z_{\frac{\lambda^2}{\alpha},\sqrt{\frac{\lambda}{2}},\sqrt{\frac{1}{2\lambda}}}(t) \\ X_{\frac{\lambda^2}{\alpha}}(f) &= \mathcal{F}\left\{x_{\frac{\lambda^2}{\alpha}}(t)\right\} = z_{\frac{\alpha}{\lambda^2},\sqrt{\frac{1}{2\lambda}},\sqrt{\frac{\lambda}{2}}}(f) \end{aligned} \tag{3.20}$$

Compare (3.19) with (3.20), we can conclude that

$$\begin{aligned} x_\alpha(t) &= \sqrt{\lambda} X_{\frac{\lambda^2}{\alpha}}(\lambda t) \\ X_\alpha(f) &= \frac{\sqrt{\lambda}}{\lambda} x_{\frac{\lambda^2}{\alpha}}(\frac{f}{\lambda}) \end{aligned} \tag{3.21}$$

By applying (3.21) into (2.33) and using the fact that $x(t)$ is symmetric around the origin with unitary energy, we get

$$\begin{aligned} (\Delta t)^2(x_\alpha) &= \lambda\int t^2 |X_{\frac{\lambda^2}{\alpha}}(\lambda t)|^2 dt = \frac{1}{\lambda^2}(\Delta f)^2(x_{\frac{\lambda^2}{\alpha}}) \\ (\Delta f)^2(x_\alpha) &= \frac{1}{\lambda}\int f^2 |x_{\frac{\lambda^2}{\alpha}}(\frac{f}{\lambda})|^2 df = \lambda^2(\Delta t)^2(x_{\frac{\lambda^2}{\alpha}}) \end{aligned} \tag{3.22}$$

where the last equality in both equations come from variable substitution by $f = \lambda t$ and $t = \frac{f}{\lambda}$, respectively.

Therefore, for $\lambda > 0$ with $\frac{\tau_0}{T} = \sqrt{\frac{1}{2\lambda}}$ and $\frac{\nu_0}{F} = \sqrt{\frac{\lambda}{2}}$, we have

$$\xi(\alpha) = \frac{1}{4\pi\Delta t(x_\alpha)\Delta f(x_\alpha)} = \frac{1}{4\pi\frac{1}{\lambda}\Delta f(x_{\frac{\lambda^2}{\alpha}})\lambda\Delta t(x_{\frac{\lambda^2}{\alpha}})} = \xi(\frac{\lambda^2}{\alpha})$$

$$\kappa(\alpha)\kappa(\frac{\lambda^2}{\alpha}) = \frac{\Delta t(x_\alpha)}{\Delta f(x_\alpha)}\frac{\Delta t(x_{\frac{\lambda^2}{\alpha}})}{\Delta f(x_{\frac{\lambda^2}{\alpha}})} = \frac{\frac{1}{\lambda}\Delta f(x_{\frac{\lambda^2}{\alpha}})\Delta t(x_{\frac{\lambda^2}{\alpha}})}{\lambda\Delta t(x_{\frac{\lambda^2}{\alpha}})\Delta f(x_{\frac{\lambda^2}{\alpha}})} = \frac{1}{\lambda^2}$$

Chapter 4

OFDM/OQAM System Design and Performance Evaluation

4.1 Introduction

In order to achieve better spectral efficiency and meanwhile reducing combined ISI/ICI, another OFDM scheme using *offset* QAM for each sub-carrier, denoted OFDM/OQAM, is of increasing importance as it has already illustrated profound advantage [10, 12, 13] over CP-OFDM in time and frequency dispersive channels. Contrary to CP-OFDM which modulates each sub-carrier with a complex-valued symbol, OFDM/OQAM modulates sub-carriers with a real-valued symbol and consequently allows time-frequency well localized pulse shape under denser system TFL requirement. The well designed IOTA pulse has already been introduced in the TIA's Digital Radio Technical Standards [36] and has been considered in WRAN(IEEE 802.22) [37].

By adopting various pulse shaping prototype functions, OFDM/OQAM can efficiently reduce both ISI and ICI without employing any guard interval. This enables a very efficient packing of time-frequency symbols maximizing e.g. the throughput or the interference robustness in the communication link.

4.2 Principles of OFDM/OQAM

Instead of using complex baseband symbols in an OFDM scheme, real valued symbols modulated by *offset* QAM are transmitted on each sub-carrier with the synthesis basis functions obtained by the time-frequency translated version of this prototype function in the following way

$$g_{m,n}(t) = e^{\phi_0 + j(m+n)\pi/2} e^{j2\pi m\nu_0 t} g(t - n\tau_0), \quad \nu_0\tau_0 = 1/2 \tag{4.1}$$

where ϕ_0 is an additional phase shift and $g(t)$ is the well designed pulse shape prototype. To maintain the orthogonality among the synthesis and analysis basis,

modified inner product is defined as follows

$$\langle x, y\rangle_{\mathbb{R}} = \Re\left\{\int_{\mathbb{R}} x^*(t)y(t)dt\right\}$$

where $\Re\{\bullet\}$ is the real part operator. That is, only the real part of the correlation function is taken into consideration. Consequently, the inner product (cross correlation) between $g_{m,n}(t)$ and $g_{m',n'}(t)$ becomes

$$\begin{aligned}
&\langle g_{m,n}, g_{m',n'}\rangle_{\mathbb{R}} = \Re\left\{\int_{\mathbb{R}} e^{j(m'+n'-m-n)\pi/2} e^{j2\pi(m'-m)\nu_0 t} g(t-n'\tau_0)g^*(t-n\tau_0)dt\right\} \\
&= \Re\left\{(j)^{m'-m+n'-n+(m'-m)(n+n')}\int_{\mathbb{R}} e^{-j2\pi(m-m')\nu_0 x} g(x+\frac{n-n'}{2}\tau_0)g^*(x-\frac{n-n'}{2}\tau_0)dx\right\} \\
&= \Re\left\{(j)^{m'-m+n'-n+(m'-m)(n+n')} A_g((n-n')\tau_0,(m-m')\nu_0)\right\} \qquad (4.2)
\end{aligned}$$

where the second equality comes from variable substitution $t = x + \frac{(n+n')\tau_0}{2}$ and the fact that $\nu_0\tau_0 = \frac{1}{2}$. For an even $g(t)$, $A_g(\tau,\nu)$ is a real valued function and (4.2) can be rewritten as

$$\langle g_{m,n}, g_{m',n'}\rangle_{\mathbb{R}} = \begin{cases} \pm A_g((n-n')\tau_0,(m-m')\nu_0) & ,(m,n) = (m',n') \bmod 2 \\ 0 & ,(m,n) \neq (m',n') \bmod 2 \end{cases} \qquad (4.3)$$

By grouping the basis $g_{m,n}(t)$ which satisfies $(m,n) = (m',n') \bmod 2$ into the same subset, the corresponding system lattice $g_{m,n}$ in the time-frequency plane can be decomposed into four sub-lattices: **EE**=$\{m$ even, n even$\}$, **EO**=$\{m$ even, n odd$\}$, **OE**=$\{m$ odd, n even$\}$ and **OO**=$\{m$ odd, n odd$\}$ [5], as shown in Fig. 4.1.

Whenever $g_{m,n}(t)$ and $g_{m',n'}(t)$ belong to different sub-lattices, the orthogonality is automatically maintained and is independent of the prototype function as long as this function is even. While inside the same sub-lattice, the orthogonality only depends on the ambiguity function $A_g(\tau,\nu)$ and hence can be ensured by just finding an even prototype function whose ambiguity function satisfies

$$A_g(2p\tau_0, 2q\nu_0) = \begin{cases} 1, & \text{when } (p,q) = (0,0) \\ 0, & \text{when } (p,q) \neq (0,0) \end{cases} \quad \text{where } p,q \in \mathbb{Z} \qquad (4.4)$$

At the receiver side

$$\begin{aligned}
\tilde{a}_n(l) = \langle g_{l,n}, r\rangle_{\mathbb{R}} &= \sum_{k=-\infty}^{+\infty}\sum_{m=0}^{N-1} h_{m,k}a_{m,k}\langle g_{l,n}, g_{m,k}\rangle_{\mathbb{R}} + \langle g_{l,n}, n\rangle_{\mathbb{R}} \\
&= \sum_{m=0}^{N-1} h_{m,n}a_{m,n}\langle g_{l,n}, g_{m,n}\rangle_{\mathbb{R}} + n_n(l) \\
&= h_{l,n}a_{l,n} + n_n(l)
\end{aligned}$$

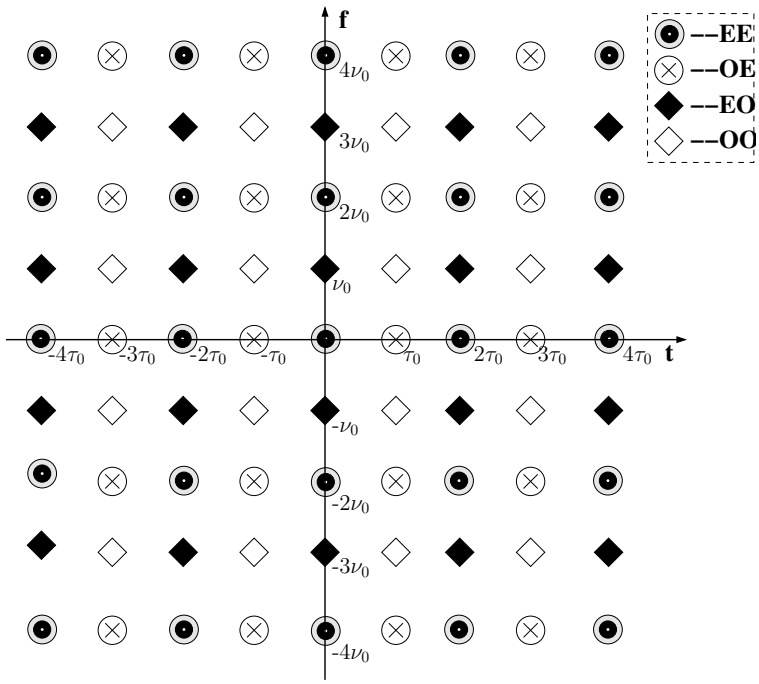

Figure 4.1: OFDM/OQAM lattice.

where $h_{l,n}$ is the amplitude of the channel realization which is assumed known by the receiver.

Fig. 4.1 can also be used for comparison of spectral density between OFDM ($TF = 1$) and OFDM/OQAM ($\tau_0\nu_0 = \frac{1}{2}$) systems. Assuming in the OFDM/OQAM system $\nu_0 = F$, $\tau_0 = \frac{T}{2}$ for convenience, then the OFDM system transmits complex symbols on these black solid lattice points (**EE**, **EO**) while the OFDM/OQAM system transmit the real parts of complex symbols on these black solid lattice points and the imaginary parts on these white hollow lattice points (**OE**, **OO**). Therefore the OFDM/OQAM system has double symbol rate but half coding rate compared with the OFDM system, which results in the same data rate per frequency usage and per time unit (spectral efficiency).

So far, two things have to be noted:

- On system level, OFDM/OQAM has twice the system lattice density (for $g_{m,n}$, $\frac{1}{\tau_0\nu_0} = 2$) but half the coding rate (only transmit real-valued symbols) compared to OFDM without cyclic prefix, therefore it has the same spectral efficiency ($\eta = \frac{1/2\log_2 M}{\tau_0\nu_0} = \log_2 M$ [bit/s/Hz]), as OFDM without cyclic prefix, cf. (2.17).

- For prototype function design, OFDM/OQAM has less lattice density requirement ($A_g(\tau,\nu)=0 \Rightarrow \frac{1}{2\tau_0 2\nu_0}=\frac{1}{2}$) compared to OFDM ($\frac{1}{TF}=1$).

The above two features make it possible for OFDM/OQAM system to find a well-localized prototype function while maintaining (bi-)orthogonality and therefore makes pulse shaping OFDM/OQAM an attractive candidate for a time and frequency dispersive channel.

4.3 Efficient implementation

As shown in Sec. 2.2, the OFDM system can be efficiently implemented by FFT/IFFT modules, whereas in an OFDM/OQAM system extra filters are needed to do pulse shaping. A direct implementation of the OFDM/OQAM system with finite impulse response (FIR) filters on each sub-carrier branch will be time consuming and cause a large delay. As the duration of the even prototype function can be very long (e.g. IOTA and EGF is theoretically infinite), a large delay has to be introduced to make the system causal (i.e., realizable[1]). Alternatively, another approach which utilizes uniform DFT filter banks [6, 30] provides a very efficient implementation and preserves the orthogonality of the prototype functions. Two kinds of realizations of pulse shaping OFDM/OQAM systems are of practical interest as they are very easy to be implemented in a classic OFDM system. Assume T is the OFDM symbol duration and F is the inter-carrier frequency spacing, we have $TF=1$ when no CP is added. One can either set $\nu_0=F$ and shorten symbol duration [30,38], or set $\tau_0=T$ and double the number of sub-carriers [39]. We use the former approach.

The filter banks for OFDM/OQAM which are designed to satisfy the perfect reconstruction (PR) condition face difficulties when the signal is passed through time varying channels. However the wireless channel is in nature doubly dispersive (hence time varying) and the PR property designed under perfect channel condition turns out not be PR anymore, resulting considerable amount of ISI/ICI. Therefore as long as the joint ISI/ICI can be reduced to a satified level (according to the system requirements), it is not a good idea to confine oneself to the PR condition when designing the wireless communication systems. Rather than deriving the implementation structure from filter bank theory, like in [6,30,39], we try to find the implementation method by directly discretising the continuous time model without considering the PR condition.

Let $s(t)$ be the output signal of OFDM/OQAM modulator ($\phi_0=0$ is assumed in the following for simplicity)

$$\begin{aligned} s(t) &= \sum_{n=-\infty}^{\infty}\sum_{m=0}^{N-1}\left[a_{m,n}^{\Re}g_{m,2n}(t)+a_{m,n}^{\Im}g_{m,2n+1}(t)\right] \\ &= \sum_{n=-\infty}^{\infty}\sum_{m=0}^{N-1}\left[a_{m,n}^{\Re}g(t-2n\tau_0)+ja_{m,n}^{\Im}g(t-2n\tau_0)\right]e^{j\frac{\pi}{2}(m+2n)}e^{j2\pi m\nu_0 t} \end{aligned} \tag{4.5}$$

[1] A system is realizable only if it is causal.

and the demodulated signal at branch k during symbol duration n can be written as

$$\tilde{a}^{\Re}_{m,n} = \Re\left\{\int_{\mathbb{R}} s(t) g^*_{m,2n}(t)dt\right\} \qquad \tilde{a}^{\Im}_{m,n} = \Re\left\{\int_{\mathbb{R}} s(t) g^*_{m,2n+1}(t)dt\right\} \tag{4.6}$$

where $\Re$ and $\Im$ indicate the real and imaginary part respectively.

By sampling $s(t)$ at rate $1/T_s$ during time interval $[nT - \tau_0, nT + \tau_0)$, as shown in Appendix 4.5 A, the transmitted signal can be written as

$$s_k[n] \triangleq s(nT + kT_s) = g_k[n] * A^k_N(a^{\Re}_{m,n}) + g_{k-N/2}[n] * A^k_N(ja^{\Im}_{m,n}) \tag{4.7}$$

where

$$A^k_N(x_{m,n}) \triangleq \sum_{m=0}^{N-1} x_{m,n} e^{j\frac{\pi}{2}(m+2n)} e^{j2\pi\frac{mk}{N}},\ k = -\frac{N}{2}, ..., \frac{N}{2} - 1 \tag{4.8}$$

$$g_k[p] \triangleq g[pN + k] = g(pT + kT_s), \quad p \in \mathbb{Z} \tag{4.9}$$

Therefore the OFDM/OQAM modulator can be easily implemented by a IFFT[2] block defined in (4.8) followed by a pulse shaping filter bank defined in (4.9).

At the receiver side, we sample the received signal $r(t)$ at rate $1/T_s$, and rewrite (4.6) as follows

$$\tilde{a}^{\Re}_{m,n} \approx \Re\left\{T_s j^{(m+2n)} \sum_{k=-\frac{N}{2}}^{\frac{N}{2}-1} r_k[n] * g_k[-n] e^{-j2\pi\frac{m(k+N/2)}{N}}\right\} \tag{4.10}$$

$$\tilde{a}^{\Im}_{m,n} \approx \Im\left\{T_s j^{-(m+2n)} \sum_{k=0}^{N-1} r_k[n] * g_{k-\frac{N}{2}}[-n] e^{-j2\pi\frac{mk}{N}}\right\} \tag{4.11}$$

where

$$g_k[-n] = g[-nN+k] = g(kT_s - NT) g_{k-\frac{N}{2}}[-n] = g[-nN+k-\frac{N}{2}] = g(kT_s - NT - T/2)$$

Therefore, if we use (4.10) and (4.11), the OFDM/OQAM demodulator can be implemented by filter banks $g_k[n]$ and $g_{k-\frac{N}{2}}[n]$ followed by a FFT block. The implementation diagram is shown in Fig. 4.2, which looks similar as the system diagram presented in [40].

Assume the pulse shape prototype function $g(t)$ (or its truncation) has finite duration in $-M\tau_0 \le t < M\tau_0$, its discrete version $g[n]$ is not empty when $n = -MN/2, ..., MN/2 - 1$. Therefore the length of each branch filter equals to M.

[2] A $N/2$ rotation of IFFT output is needed here to shift the zero frequency sub-carrier to middle position.

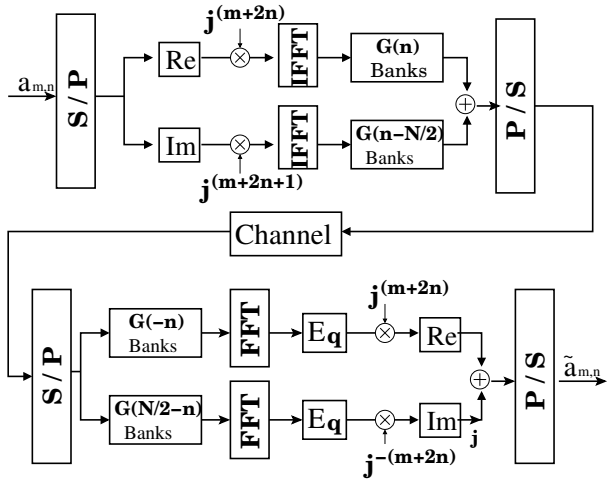

Figure 4.2: OFDM/OQAM implementation diagram.

4.4 Performance evaluation

In this section we present various simulation results for OFDM/OQAM systems with different system parameters, with CP-OFDM as the benchmark. All the results reported in this section are obtained from the Matlab/Octave simulation workbench [18, 19], with a one-tap zero-forcing frequency domain equaliser (FDE) implemented at the receiver side. Unless mentioned otherwise, both CP-OFDM and OFDM/OQAM utilise the same channel estimation results which are obtained through perfect OFDM channel estimation.

TFL analysis

To illustrate how the demodulation gain varies with respect to the time and frequency spread, we plot the ambiguity function of the output of one demodulation branch, i.e.

$$\sum_{m,n} |A(\tau - 2n\tau_0, \nu - 2m\nu_0)|^2$$

A three dimensional plot is presented in Fig. 4.3 by utilizing the IOTA prototype function. Axes are normalized by τ_0 and ν_0 respectively. Here the data transmitted on each basis function is ignored for simplicity, and only the neighboring lattice points in the same subset are considered. Fig. 4.4 shows two-dimensional contour plots in which the EGF prototype functions are used. When the channel is ideal, as shown in Fig. 4.4, EGF ($\alpha = 2$) will introduce smaller distortion compared to EGF ($\alpha = 1$) since the ISI is significantly decreased although the ICI increases a little.

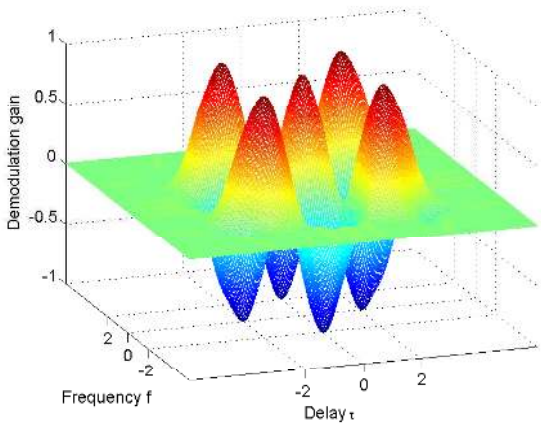

Figure 4.3: Demodulation gain for IOTA prototype in OFDM/OQAM.

Orthogonality over an ideal channel

Define the orthogonality parameter for different pulse shapes as

$$\gamma^2 = E\{|\tilde{a}_{m,n} - a_{m,n}|^2\} \tag{4.12}$$

where $a_{m,n}$ is the transmitted symbol, $\tilde{a}_{m,n}$ is the reconstructed signal. γ^2 can also be used to indicate the distortion power introduced by non-perfect reconstruction through an ideal channel ($r(t) = s(t)$), see below.

Pulse	OFDM	Half-cosine	RRC	Gaussian α=1|α=2	EGF $\alpha = 1$	EGF $\alpha = 2$
γ^2 [dB]	-314	-309	-69	-11 |-22	-96	-178

CP-OFDM and OFDM/OQAM with the half cosine function can achieve perfect reconstruction in the absence of a channel as the level of distortion power reaches the resolution limit of a double precision number ($\approx 10^{-15}$). OFDM/OQAM with the EGF pulse shape introduce limited distortion due to pulse shape truncation, and the distortion introduced by the Gaussian pulse is very significant due to lack of orthogonality.

Fig. 4.5 presents the reconstructed signal constellation at the OFDM/OQAM demodulator output for an ideal channel with a 16QAM modulation. With the length of component filters $M = 12$, EGF, Half Cosine and Root Raised Cosine prototypes can achieve almost perfect reconstruction (see Fig. 4.5 a, b, d) while the Rectangular prototype will result in some distortion (see Fig. 4.5 c).

For the EGF prototype function, the influence of three parameters α, τ_0 and the length of filter taps M is shown in Fig. 4.6. It shows that when the number of

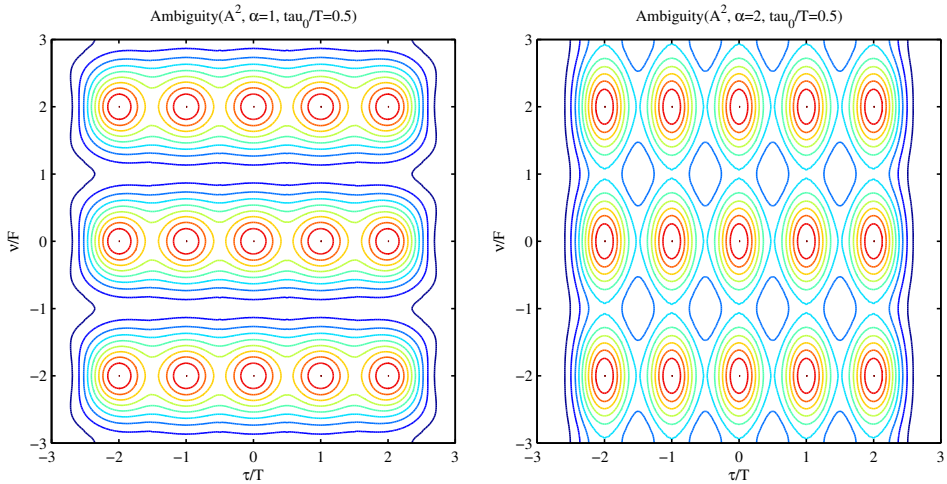

EGF ($\alpha = 1$) EGF ($\alpha = 2$)

Figure 4.4: Contour plots for demodulation output with EGF prototypes in OFDM/OQAM.

filter taps is large enough (e.g. $M = 6$), the performance of EGF prototypes with different α is pretty good. However, when the number of filter taps is insufficient (e.g. $M = 2$), the most centralized prototype (with highest α) will be least affected by truncation (cf. Fig. 4.6 (1)b vs. Fig. 4.6 (1)d). Fig. 4.6 (2) displays the influence of the symbol length τ_0 on reconstruction performance with fixed $\alpha = 2$ and M. Obviously even a slight variation of τ_0 affects the performance significantly.

Frequency offset sensitivity

In [41] it was shown that in OFDM systems the power of interference brought in by frequency offset can be written as

$$E_I = 1 - \mathrm{sinc}^2(\frac{f_\Delta}{F}) \approx \frac{\pi^2}{3}(\frac{f_\Delta}{F})^2 \tag{4.13}$$

where f_Δ is the carrier frequency offset, $F = F_s/N$ is the frequency separation. The rotation effect of the symbol is assumed to be compensated perfectly and the number of carriers N is assumed to be large.

In this part we will evaluate the total distortion brought in by the frequency offset and therefore the rotation effect will also be taken into consideration when calculating the average distortion power γ^2 as defined in (4.12). The phase noise is omitted. Assume each data frame consists of N_r OFDM symbols and each symbols contains N samples in OFDM/OQAM and $N + N_{cp}$ samples in CP-OFDM respectively, where N_{cp} denotes the number of cyclic prefix symbols inserted. The

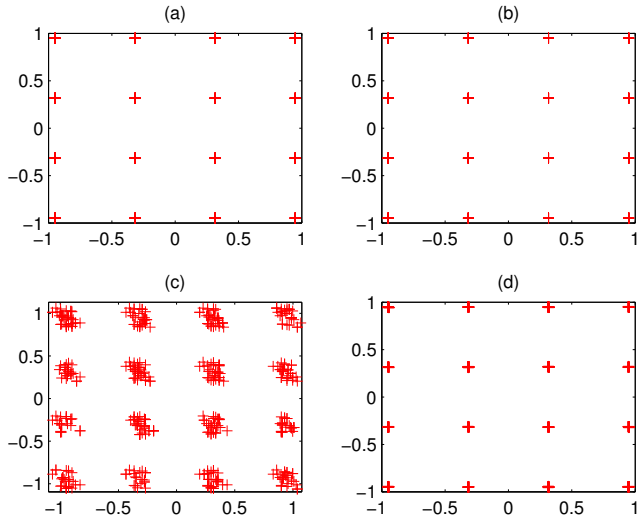

Figure 4.5: Signal constellation with a 16QAM modulation for (a) EGF (b) Half Cosine (c) Rectangular (d) Root Raised Cosine with $\rho = 0.2$.

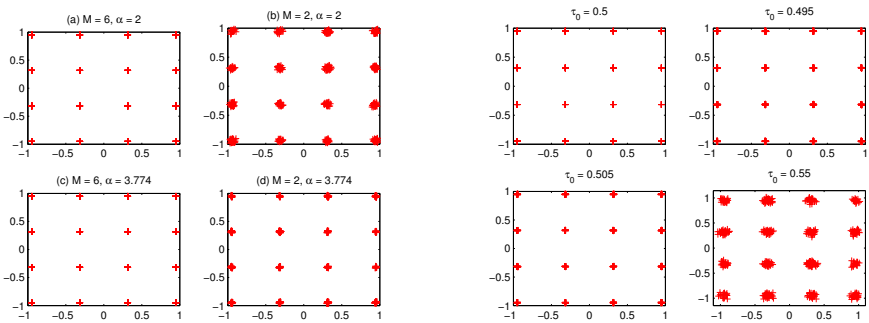

(1) EGF with $\tau_0 = 0.5$ (2) EGF ($M = 6$, $\alpha = 2$)

Figure 4.6: Signal constellation of EGF with a 16QAM modulation.

distortion power γ^2 in CP-OFDM systems introduced by carrier frequency offset f_Δ through an ideal channel (with only frequency offset added), shown in Appendix 4.5 B, is rewritten as

$$\gamma^2_{OFDM} = \frac{4}{3}\left(\pi N N_r \frac{f_\Delta}{F_s}\right)^2 \left(1 + \frac{N_{cp}}{N}\right)^2 \tag{4.14}$$

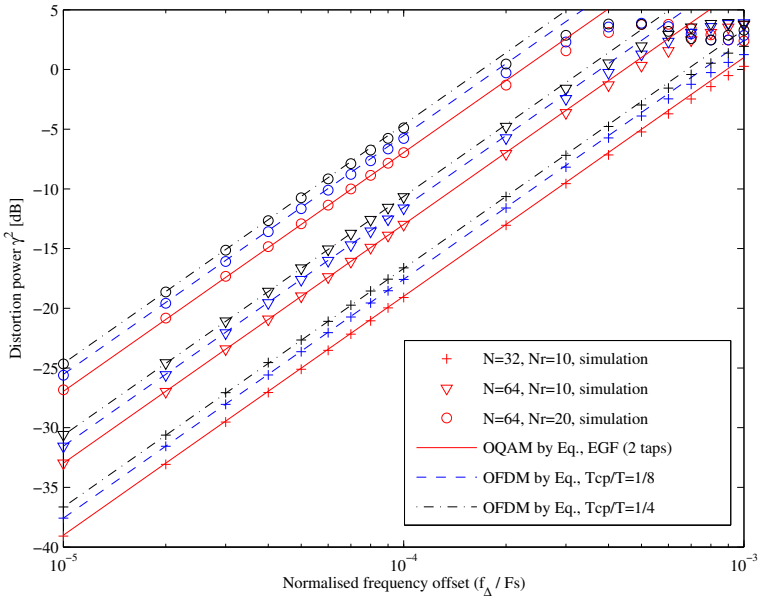

Figure 4.7: Frequency offset robustness for CP-OFDM and OFDM/OQAM (2-tap EGF) systems with a QPSK modulation.

The number of symbols N_r per data frame appears since the phase shift caused by carrier frequency offset f_Δ accumulates as the length of data frame increases, and therefore increase the distortion power. The general expression for OFDM/OQAM with different pulse shapes has a similar form as for CP-OFDM

$$\gamma^2_{OQAM} = \frac{4}{3}\left(\pi N N_r \frac{f_\Delta}{F_s}\right)^2 \epsilon_g \tag{4.15}$$

where $\epsilon_g > 0$ is a scaling factor related to the pulse shape $g(t)$ and can be determined by numerical methods. The number of taps in the pulse shape filter bank will affect the value of ϵ_g since it will increase the length of the data block and therefore the phase shift, if the number of taps used is larger than 1. Therefore a trade off between orthogonality and frequency offset sensitivity has to be made to achieve small ϵ_g. In practice a preamble or a pilot sequence will be used for synchronisation and frequency offset estimation, then the number of taps will not be a problem anymore. In such cases the value of ϵ_g will always be smaller than 1. This should be contrasted with the factor $(1 + N_{cp}/N)^2$ for OFDM.

Both simulation results (markers only) and curves by (4.14) and (4.15) are shown in Fig. 4.7. When the same system parameters are used, OFDM/OQAM always outperforms CP-OFDM by 0.9dB to 2.3dB, in which about 0.5dB ($T_{cp}/T = 1/16$)

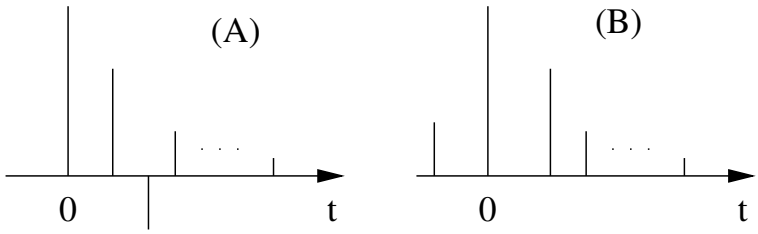

Figure 4.8: Illustration of impulse response for channel A and B.

to 1.9dB ($T_{cp}/T = 1/4$) comes from not using the cyclic prefix and another 0.4dB gain from the pulse shape itself with $\epsilon_g \approx 0.92$.

Immunity to time and frequency dispersion

Two kinds of channels are used in this part, with the channel parameters listed in the table below and the illustration of channel impulse response in Fig. 4.8.

	paths	1	2	3	4	5	6	B_d/F_s
A	Delay [T_s]	0	2	4	7	11	14	
	Power [dB]	0	-7	-15	-22	-24	-19	10^{-5}
B	Delay [T_s]	-3	0	2	4	7	11	
	Power [dB]	-6	0	-7	-22	-16	-20	10^{-5}

The channel parameters for channel A and B are motivated by the reference channel profiles in WRAN standard proposal [37] where channel A is the typical rural area channel model and channel B is the typical urban channel model. In both of the two channels the delay spread $T_d = 14T_s$ and the Doppler spread $B_D = 10^{-5}F_s$. For a carrier frequency $f_c = 2GHz$ and sampling frequency $F_s = 7.68MHz$, the normalized Doppler spread $B_D/F_s = 10^{-5}$ is equivalent to a moving speed of 41.5km/h. Noise is not introduced so that all the distortion comes either from time spread or frequency spread. A cyclic prefix with length $T_{cp} = 16T_s$ is used in the CP-OFDM system, unless mentioned otherwise. Each component filter in the OFDM/OQAM system has maximum 12 taps.

Fig. 4.9 presents the reconstructed signal constellation in OFDM/OQAM and CP-OFDM systems over channel A and B. In Fig. 4.9 (1) a and (1) b channel B is used with $B_D = 0$, increased FFT size N decreases the distortion power. In Fig. 4.9 (1) c and (1) d channel A is used with $T_{cp} > T_d$, and hence only the frequency dispersion introduces distortion. In this case the increased FFT size N significantly enlarges distortion as the ratio $B_D/F = N * B_D/F_s$ increases accordingly. This confirms our previous analysis. In Fig. 4.9 (2) only channel A is used. With the FFT size equals to 32, the one-tap FDE is far from perfect and therefore causes large distortion which is dominated by multipath fading. When N

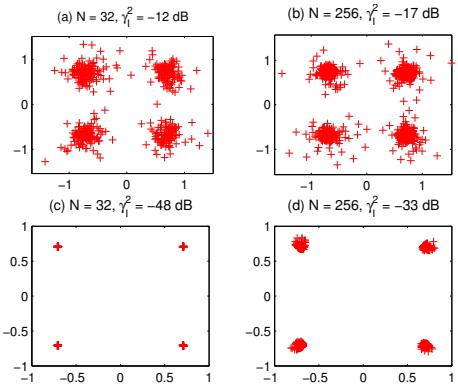

(1) CP-OFDM, channel A used in (a, b), and channel B used in (c, d).

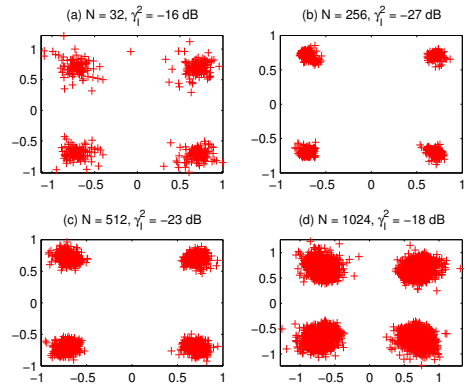

(2) EGF with $M = 6$, $\alpha = 2$, channel B.

Figure 4.9: Signal constellation over channel A and B with a QPSK modulation.

becomes large enough, the performance loss of one-tap FDE tends to be negligible while the distortion from frequency dispersion becomes large as $\frac{B_D}{F}$ increases. The system finally becomes frequency dispersion dominated where increasing the FFT size will only degrade the system performance.

Fig. 4.10 illustrates the Bit Error Rate (BER) performance of uncoded transmission over doubly dispersive channels A and B with FFT size $N = 256$ and 4000 channel realizations. $T_{cp} = 16T_s$ are used in CP-OFDM and maximum 12 taps for each pulse shaping component filter are used in OFDM/OQAM systems. In channel A where all the multipath interference can be fully removed by CP, CP-OFDM performs a little better than OFDM/OQAM systems (about 0.2 dB in high SNR region). However, when channel B is used, cyclic prefix alone cannot combat interference from "early" arrived paths, and therefore significantly degrades the performance, while OFDM/OQAM systems with different pulse shapes shows much stronger immunity and better performance. Besides, a considerable power and spectral efficiency gain is achieved in OFDM/OQAM by not using CP. For OFDM with CP of length T_cp, we have $E_s = E_b \log M$ where E_s is the symbol energy and E_b is the effective energy per bit, with M equals to the modulation order. On the other hand, we have $E_s = (T + T_{cp})P$ where P is the average signal power. Since SNR $\triangleq \frac{P}{N_0 F}$, the relation between E_b/N_0 and SNR is as follows

$$E_b/N_0 = \frac{E_b}{N_0} = \frac{E_s/\log M}{N_0} = \frac{T + T_{cp}}{T \log M} \frac{P}{N_0 F} = \left(1 + \frac{T_{cp}}{T}\right) \frac{\text{SNR}}{\log M} \tag{4.16}$$

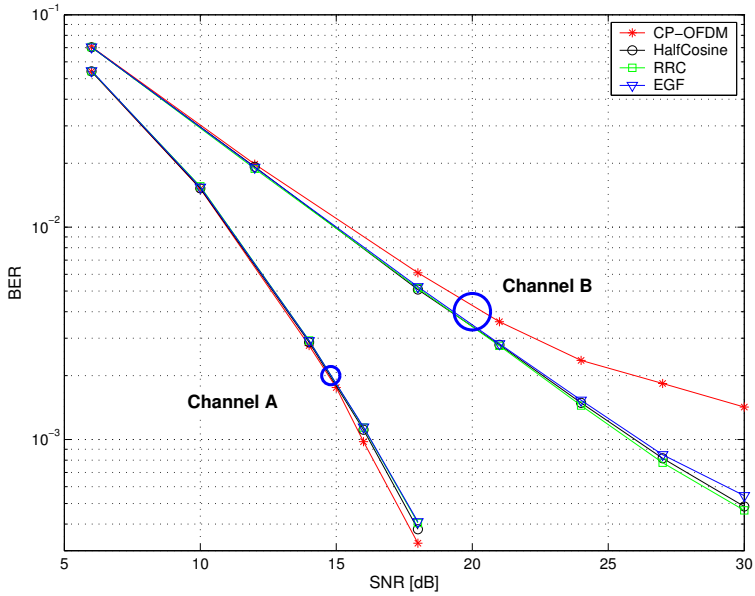

Figure 4.10: Uncoded BER versus SNR with a QPSK modulation over channel A and B.

Performance of pulse shape adaptation

Apart from the two specific channels A and B like above, some more general channel models will be of great interest. An extended Monte Carlo-based WSSUS channel model [21] for doubly dispersive channels is used, with the assumption of an exponential delay power profile and a U-shaped Doppler power spectrum as defined in (2.9). Two time dispersive channels and one doubly dispersive channel are used in the following simulation, with the channel parameters listed in the table below. For a carrier frequency $f_c = 2.5GHz$, Doppler spread $B_d = 2f_D = 700Hz$ is equivalent to a moving speed of 157.5km/h.

channel	$\tau \in [\mu s]$	τ_d $[\mu s]$	τ_{RMS} $[\mu s]$	$B_d[Hz]$	#taps
C	[0, 4.167]	4.167	1.042	0	< 10
D	[-1.042, 3.125]	4.167	1.042	0	< 10
E	[0, 4.167]	4.167	1.042	700	< 10

In OFDM/OQAM systems each component filter has maximum 4 taps and a cyclic prefix with length $\frac{T_{cp}}{T} = \frac{1}{8}$ is used in the CP-OFDM system, unless mentioned otherwise. Frequency separation $F = 15kHz$ is used for both CP-OFDM and OFDM/OQAM, and $N_r = 10$ OFDM symbols (i.e. 20 OQAM symbols) are packaged in one data frame and transmitted through channels implemented via the

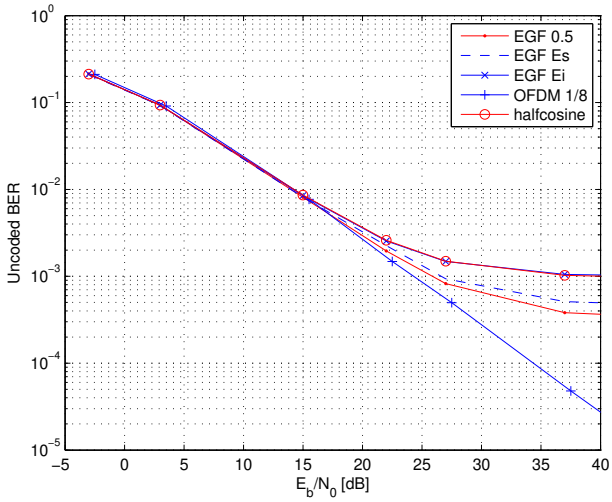

Figure 4.11: Uncoded BER for CP-OFDM ($N_{cp}/N = 1/8$), OFDM/OQAM with EGF (4 taps), and OFDM/OQAM with half-cosine (1-tap) over channel C, using a QPSK modulation.

tapped delay line model [23]. Each data frame contains one preamble symbol for channel estimation followed by N_r data symbols. An one-tap zero-forcing frequency domain equaliser (FDE) is used together with a normal AWGN symbol detector. In OFDM/OQAM systems, EGF with a 4-tap filter bank and half-cosine with a 1-tap filter bank are used. The Gaussian parameter α in EGF is chosen via numerical solution according to Sec. 3.3 by maximising the signal power E_S, or by minimising the interference power E_I. The lower bound[3] $\alpha = 0.5$ in EGF functions is chosen for reference.

Fig. 4.11 and Fig. 4.12 illustrates the BER performance of uncoded transmission for OFDM/OQAM through time dispersive channels. When channel C is used, the distortion caused by time dispersion is fully removed by the cyclic prefix in CP-OFDM and partially reduced by pulse shapes in OFDM/OQAM systems. When channel D is used, OFDM/OQAM outperforms CP-OFDM as the interference from "early" arrived paths cannot be removed by the cyclic prefix. In the high SNR region, an error floor always shows up for OFDM/OQAM systems as a result of imperfect reconstruction due to the multipath and noise distortion. In the low SNR region there is moderate gain of OFDM/OQAM compared with CP-OFDM, which mainly comes from the energy saved by not using the cyclic prefix (0.51dB for $N_{cp}/N = 1/8$). It is a little bit surprising that the performance of EGF with minimised interference power (E_I) performs worse than EGF with maximised signal

[3]Empirical observation shows that $\alpha \in [0.5, 7]$ for EGF functions will give a good trade off between time frequency localisation and orthogonality.

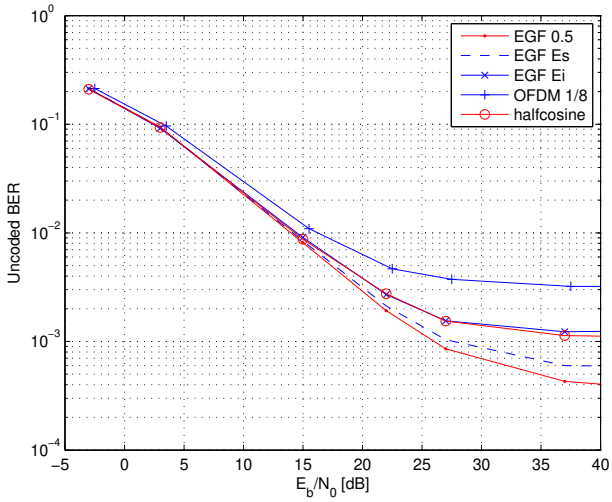

Figure 4.12: Uncoded BER for CP-OFDM ($N_{cp}/N = 1/8$), OFDM/OQAM with EGF (4 taps), and OFDM/OQAM with half-cosine (1-tap) over channel D, using a QPSK modulation.

power (E_S), as can be seen in Fig. 4.11 and Fig. 4.12. One possible reason is that the minimisation of interference power is based on the assumption of perfect equalisation. This is not the case in our implementation with a one-tap FDE. Since channel C and channel D are purely time dispersive, a pulse with larger support in time domain will satisfy the requirement stated in (3.2),

$$\kappa(\alpha) = \frac{\Delta t}{\Delta f} \propto \frac{\tau_{\mathrm{RMS}}/T}{f_D/F} = \frac{\tau_{\mathrm{RMS}}}{f_D} \left(\frac{F_s}{N}\right)^2$$

which means a smaller value of α for EGF functions. Therefore EGF with $\alpha = 0.5$ performs the best among different pulse shapes in OFDM/OQAM.

The uncoded BER performance over doubly dispersive channels is shown in Fig. 4.13. The performance degradation due to channel variation is very significant in all the systems, while OFDM/OQAM with different pulse shapes all outperform CP-OFDM. However, the difference between different pulse shapes is not resolvable. A more powerful detector, such as minimum mean square error (MMSE) detector with successive interference cancellation [15], is needed to exploit the benefit of higher signal to interference ratio.

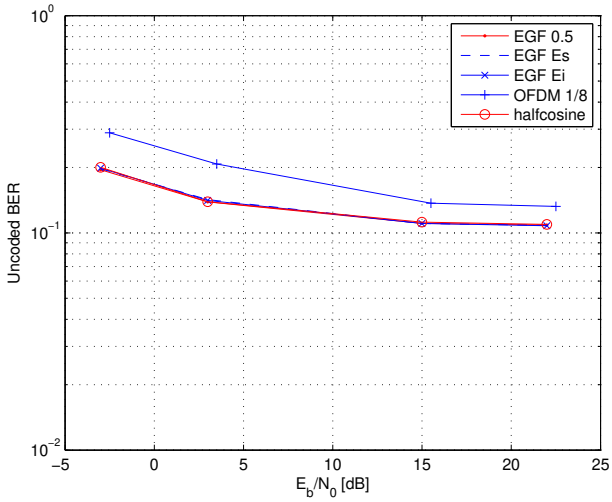

Figure 4.13: Uncoded BER for CP-OFDM ($N_{cp}/N = 1/8$), OFDM/OQAM with EGF (4 taps), and OFDM/OQAM with half-cosine (1-tap) over channel E, using a QPSK modulation.

4.5 Appendix

A. Implementation of OFDM/OQAM

By sampling $s(t)$ at rate $1/T_s$ during time interval $[nT - \tau_0, nT + \tau_0)$, we get

$$\begin{aligned} s(nT + kT_s) = \sum_{l=-\infty}^{\infty} \sum_{m=0}^{N-1} \Big[& a_{m,l}^{\Re} g(nT + kT_s - lT) \\ & + j a_{m,l}^{\Im} g(nT + kT_s - lT - \frac{T}{2}) \Big] e^{j\frac{\pi}{2}(m+2l)} e^{j2\pi\frac{mk}{N}} \end{aligned} \tag{4.17}$$

where $n \in \mathbb{Z}$ and $k = -\frac{N}{2}, ..., \frac{N}{2} - 1$.

Let $s_k[n] = s[nN + k] = s(nT + kT_s)$ and take variable substitution $p = n - l$,

(4.17) can be rewritten as

$$\begin{aligned} s_k[n] \triangleq s[nN+k] &= \sum_{p=-\infty}^{\infty} g(pT+kT_s)\left[\sum_{m=0}^{N-1} a^{\Re}_{m,n-p} e^{j\frac{\pi}{2}(m+2n-2p)} e^{j2\pi\frac{mk}{N}}\right] \\ &\quad + \sum_{p=-\infty}^{\infty} g(pT+kT_s-\frac{T}{2})\left[\sum_{m=0}^{N-1} j a^{\Im}_{m,n-p} e^{j\frac{\pi}{2}(m+2n-2p)} e^{j2\pi\frac{mk}{N}}\right] \quad (4.18) \\ &= \sum_{p=-\infty}^{\infty} \left[g[pN+k]A^k_N(a^{\Re}_{m,n-p}) + g[pN+k-N/2]A^k_N(ja^{\Im}_{m,n-p})\right] \\ &= g_k[n] * A^k_N(a^{\Re}_{m,n}) + g_{k-N/2}[n] * A^k_N(ja^{\Im}_{m,n}) \end{aligned}$$

in which

$$A^k_N(x_{m,n}) \triangleq \sum_{m=0}^{N-1} x_{m,n} e^{j\frac{\pi}{2}(m+2n)} e^{j2\pi\frac{mk}{N}},\ k = -\frac{N}{2}, ..., \frac{N}{2}-1$$

$$g_k[p] \triangleq g[pN+k] = g(pT+kT_s), \quad p \in \mathbb{Z}$$

At the receiver side, by sampling the received signal $r(t)$ at rate $1/T_s$ and approximating the integration with summation, (4.6) can be rewritten as follows

$$\begin{aligned} \tilde{a}^{\Re}_{m,n} &\approx \Re\left\{T_s \sum_{l=-\infty}^{\infty} \sum_{k=-\frac{N}{2}}^{\frac{N}{2}-1} r(lT+kT_s) g^*_{m,2n}(lT+kT_s)\right\} \\ &= \Re\left\{T_s \sum_{l=-\infty}^{\infty} \sum_{k=-\frac{N}{2}}^{\frac{N}{2}-1} r(lT+kT_s) g(lT+kT_s-nT) e^{-j\frac{\pi}{2}(m+2n)} e^{-j2\pi\frac{mk}{N}}\right\} \\ &= \Re\left\{T_s e^{-j\frac{\pi}{2}(m+2n)} \sum_{k=-\frac{N}{2}}^{\frac{N}{2}-1} \sum_{l=-\infty}^{\infty} r_k[l] g_k[-(n-l)] e^{-j2\pi\frac{mk}{N}}\right\} \\ &= \Re\left\{T_s e^{-j\frac{\pi}{2}(m+2n)} \sum_{k=-\frac{N}{2}}^{\frac{N}{2}-1} r_k[n] * g_k[-n] e^{-j2\pi\frac{mk}{N}}\right\} \quad (4.19) \\ &= \Re\left\{T_s j^{(m-2n)} \sum_{k=-\frac{N}{2}}^{\frac{N}{2}-1} r_k[n] * g_k[-n] e^{-j2\pi\frac{m(k+N/2)}{N}}\right\} \\ &= \Re\left\{T_s j^{(m+2n)} \sum_{k=-\frac{N}{2}}^{\frac{N}{2}-1} r_k[n] * g_k[-n] e^{-j2\pi\frac{m(k+N/2)}{N}}\right\} \end{aligned}$$

where the second equality comes from the definition $g_k[-n] = g[-nN+k] = g(kT_s - NT)$, the third equality comes from the definition of convolution, and the last equality comes from the fact that $j^{(m+2n)} = j^{(m-2n)}$.

By repeating the above process for the imaginary branch, we have

$$\tilde{a}_{m,n}^{\Im} \approx \Re\left\{ T_s \sum_{l=-\infty}^{\infty} \sum_{k=-\frac{N}{2}}^{\frac{N}{2}-1} r(lT + \frac{T}{2} + kT_s) g_{m,2n+1}^{*}(lT + \frac{T}{2} + kT_s) \right\} \tag{4.20}$$

$$= \Re\left\{ T_s \sum_{l=-\infty}^{\infty} \sum_{k=-\frac{N}{2}}^{\frac{N}{2}-1} r(lT + \frac{T}{2} + kT_s) g(lT + kT_s - nT) e^{-j\frac{\pi}{2}(m+2n+1)} e^{-j2\pi\frac{m(k+N/2)}{N}} \right\}$$

$$= \Im\left\{ T_s e^{-j\frac{\pi}{2}(m+2n)} \sum_{k=-\frac{N}{2}}^{\frac{N}{2}-1} \sum_{l=-\infty}^{\infty} r_{k+\frac{N}{2}}[l] g_k[-(n-l)] e^{-j2\pi\frac{m(k+N/2)}{N}} \right\}$$

$$= \Im\left\{ T_s j^{-(m+2n)} \sum_{k=-\frac{N}{2}}^{\frac{N}{2}-1} r_{k+\frac{N}{2}}[n] * g_k[-n] e^{-j2\pi\frac{m(k+N/2)}{N}} \right\}$$

$$= \Im\left\{ T_s j^{-(m+2n)} \sum_{k=0}^{N-1} r_k[n] * g_{k-\frac{N}{2}}[-n] e^{-j2\pi\frac{mk}{N}} \right\}$$

where the last equality comes from variable substitution.

B. Distortion caused by frequency offset in OFDM systems

For the nth symbol in the OFDM data frame,

$$\hat{s}_k(n) = \frac{s_k}{T} \int_{nT_0}^{nT_0+T} e^{-j2\pi f_\Delta t} dt = s_k \frac{\sin \pi f_\Delta T}{\pi f_\Delta T} e^{-j2\pi f_\Delta (nT_0 + T/2)} \tag{4.21}$$

where $T = NT_s$ is the symbol duration, $T_{cp} = N_{cp}T_s$ is the length of CP, and $T_0 = T + T_{cp} = (N + N_{cp})T_s$ is the OFDM symbol length with CP added. Then the distortion power γ^2 can be written as

$$\gamma_k^2(n) = |s_k(n) - \hat{s}_k(n)|^2 + \sum_{m \neq k} |I_m|^2 \tag{4.22}$$

where the first term on the right side the distortion brought in by constellation rotation and the second term indicates the total ICI by the offset. According to [41] we have

$$\sum_{m \neq k} |I_m|^2 = E_I$$

where E_I is described in (4.13).

Assume the transmitted data symbol have unit energy, i.e. $|s_k(n)|^2 = 1$, by substituting (4.13) and (4.21) into (4.22), we have

$$\begin{aligned}\gamma_k^2(n) &= |1 - \text{sinc}(f_\Delta T) e^{-j2\pi f_\Delta (nT_0 + T/2)}|^2 + 1 - \text{sinc}^2\left(\frac{f_\Delta}{F}\right) \\ &= 1 + \text{sinc}^2(f_\Delta T) - 2\text{sinc}(f_\Delta T)\cos 2\pi f_\Delta (nT_0 + T/2) + 1 - \text{sinc}^2(f_\Delta T) \\ &= 2 - 2\text{sinc}(f_\Delta T)\cos 2\pi f_\Delta (nT_0 + T/2)\end{aligned} \tag{4.23}$$

Since this distortion is independent of the carrier index k, the average distortion power among the whole OFDM data frame can be written as

$$\begin{aligned}\gamma_{OFDM}^2 &= \frac{1}{N_r}\sum_{n=0}^{N_r-1}\gamma_k^2(n) = 2 - \frac{2}{N_r}\text{sinc}(f_\Delta T)\sum_{n=0}^{N_r-1}\cos 2\pi f_\Delta (nT_0 + T/2) \\ &= 2 - 2\text{sinc}(f_\Delta T)\frac{\sin \pi N_r f_\Delta T_0}{N_r \sin \pi f_\Delta T_0}\cos \pi f_\Delta ((N_r - 1)T_0 + T) \\ &\approx 2 - 2\text{sinc}(f_\Delta T)\text{sinc}(N_r f_\Delta T_0)\cos \pi f_\Delta N_r T_0 \\ &\approx 2 - 2\left(1 - \frac{(\pi f_\Delta T)^2}{6}\right)\left(1 - \frac{(\pi N_r f_\Delta T_0)^2}{6}\right)\left(1 - \frac{(\pi N_r f_\Delta T_0)^2}{2}\right) \\ &\approx \frac{4}{3}(\pi N_r f_\Delta T_0)^2 + \frac{1}{3}(\pi f_\Delta T)^2\end{aligned} \tag{4.24}$$

Normally the number of N_r is relatively large and therefore the last term $\frac{1}{3}(\pi f_\Delta T)^2$ can be omitted for simplicity. By applying $T_0 = (N + N_{cp})T_s = \frac{N+N_{cp}}{F_s}$ into (4.24), the distortion power γ^2 in CP-OFDM systems introduced by carrier frequency offset f_Δ through an ideal channel (with only frequency offset added) can be rewritten as

$$\gamma_{OFDM}^2 = \frac{4}{3}\left(\pi N N_r \frac{f_\Delta}{F_s}\right)^2\left(1 + \frac{N_{cp}}{N}\right)^2$$

Chapter 5

Novel Channel Estimation Methods

5.1 Introduction

Multicarrier communication technologies are promising candidates to realise high data rate transmission in Beyond 3G and further wireless systems where the channel is normally doubly dispersive. Contrary to the classic OFDM system which uses a cyclic prefix (CP) to combat time dispersion, OFDM/OQAM which utilises well designed pulse shapes and/or system lattice can achieve smaller ISI/ICI without using CP, and hence has the advantage of lower power leakage and a theoretically higher spectral efficiency. Performance evaluation of OFDM/OQAM has already illustrated promising advantage [37, 42] and it has already been introduced in the TIA's Digital Radio Technical Standards [36] and been considered in WRAN (IEEE 802.22) [37], but in the latter case it has been recently pulled out to appendices pending further study partially due to its difficulties in channel estimation.

In OFDM/OQAM systems, orthogonality does not hold any more between transmitted signals in the real and imaginary branches. The demodulated real-valued OFDM/OQAM symbol always (even after transmission over an ideal channel) has imaginary-valued intrinsic interference from neighbouring symbols [12], which impedes the conventional channel estimation methods used for OFDM to be directly applied to OFDM/OQAM. Therefore channel estimation has been a big problem for OFDM/OQAM in dispersive channels and attracts numerous research efforts. A subspace based blind channel estimation method is proposed in [43] where very long data records are needed to obtain good channel estimation. In order to reduce the intrinsic interference to a minimum amount, a pilot-based channel estimation scheme has been proposed in [44] and a preamble-based channel estimation method has been proposed in [45], where in both of the two cases a group of neighbouring symbols are carefully selected so that the intrinsic interference at the central symbol position to be greatly reduced. On the contrary, by treating the

intrinsic interference from neighbouring symbols as known information and consequently forming a complex-valued pseudo pilot symbol, a preamble-based channel estimation method – interference approximation method (IAM) – has been proposed recently in [46–49] and verified through purely time dispersive channels. An ideal yet unrealistic estimation method proposed in [46] produces a performance upper bound. A real-valued preamble sequence, denoted IAM-R in the following, has been proposed in [47] which increases the power of the pseudo pilot by making the imaginary interference terms constructively adding [1], and its performance in power line communication is evaluated in [48]. In [49] the real-valued preamble symbol has been replaced by an imaginary one, hence named IAM-I in the following, so that the transmitted symbol and its associated intrinsic interference are both imaginary-valued and positively added. These two heuristic preamble sequences (IAM-R and IAM-I), however, are suboptimal since they were constructed based on tentative observations. Additionally their performance though frequency dispersive channels, which is common in mobile communication, has not been demonstrated.

Motivated by the principle of IAM method and awareness of the suboptimal nature of the two IAM methods in [47, 49], we have formulated in this paper a general theoretical framework for IAM preamble design and as a consequence identified the optimal IAM preamble sequence resulting in higher performance gain. The effectiveness of the theoretical framework and the superiority of proposed methods has thereafter been verified by numerical simulation through time and frequency dispersive channels.

The rest of this chapter is organised as follows. Section 5.2 presents the system model and the general theoretical framework for IAM preamble design. In Section 5.3 we revisit the two heuristic preamble sequences under the framework and then derive an optimal IAM preamble sequence. Simulation results under various doubly dispersive channels are shown in Section 5.5 and conclusions and summaries are shown in Section 5.6.

5.2 System model

The transmitted signal in CP-OFDM and OFDM/OQAM systems can be written in the following analytic form

$$s(t) = \sum_{n=-\infty}^{+\infty} \sum_{m=0}^{N-1} a_{m,n} g_{m,n}(t),$$

where $a_{m,n} (m = 0, 1, ..., N-1, n \in \mathbb{Z},)$ denotes the symbol conveyed by the subcarrier of index m during the symbol time of index n, and $g_{m,n}(t)$ represents the synthesis basis which is obtained by time-frequency translation of the prototype

[1] Here the term 'constructively add' means that all the elements within the summation have the same sign.

function $g(t)$. In CP-OFDM systems

$$g_{m,n}(t) = e^{j2\pi mFt} g(t - n(T + T_{cp})), \quad TF = 1$$

where T and F are the symbol duration and inter-carrier frequency spacing respectively, $a_{m,n}$ are complex valued symbols and $g(t)$ is the rectangular function. In OFDM/OQAM systems

$$g_{m,n}(t) = e^{\phi_0 + j(m+n)\pi/2} e^{j2\pi m\nu_0 t} g(t - n\tau_0), \quad \nu_0\tau_0 = 1/2$$

where ϕ_0 is an additional phase shift and $g(t)$ is the well designed pulse shape prototype. Here the transmitted symbols $a_{m,n}$ are *real-valued* with symbol duration τ_0 and inter-carrier spacing ν_0 respectively. Two kinds of realisations of OFDM/OQAM are of practical interest. One can either set $\nu_0 = F, \tau_0 = T/2$ as in [30, 38] or set $\tau_0 = T, \nu_0 = F/2$ as in [39]. We use the former approach.

After passing through the doubly dispersive channel, the received signal (noise is omitted here for simplicity) can be written as

$$\begin{aligned} r(t) &= \int h(\tau, t) s(t - \tau) d\tau = \iint H(\tau, \nu) s(t - \tau) e^{j2\pi\nu t} d\nu d\tau \\ &= \sum_{m,n} a_{m,n} \iint H(\tau, \nu) g_{m,n}(t - \tau) e^{j2\pi\nu t} d\nu d\tau \end{aligned} \tag{5.1}$$

where $h(\tau, t)$ is the channel impulse response and $H(\tau, \nu)$ is its Fourier transform with respect to t. The integration interval depends on the maximum time spread τ_{max} and the maximum Doppler frequency f_D. Without loss of generality, we assume $a_{k,l}$ is the symbol to be detected, with the corresponding demodulation output

$$\hat{a}_{k,l} =< r(t), g_{k,l}(t) > \triangleq \int r(t) g^*_{k,l}(t) dt \tag{5.2}$$

By applying auto-ambiguity function

$$A_g(\tau, \nu) = \int_{\mathbb{R}} e^{-j2\pi\nu t} g(t + \tau/2) g^*(t - \tau/2) dt$$

and follow the same procedure as in (refeqn:Ag00), the correlation between transmit and receive pulse shapes for OFDM/OQAM can be written as

$$\begin{aligned} \int g_{m,n}(t - \tau) g^*_{k,l}(t) e^{j2\pi\nu t} dt &= j^{m+n-k-l} e^{-j2\pi m\nu_0\tau} \\ &\quad \cdot \int g(t - n\tau_0 - \tau) g^*(t - l\tau_0) e^{j2\pi[(m-k)\nu_0 + \nu]t} dt \\ &= j^{m+n-k-l} e^{-j2\pi m\nu_0\tau} e^{j\pi[(m-k)\nu_0+\nu][(n+l)\tau_0+\tau]} A^*_g((n-l)\tau_0 + \tau, (m-k)\nu_0 + \nu) \end{aligned} \tag{5.3}$$

Note that the additional phase shift ϕ_0 is totally canceled out in this step. Apply (5.3) to (5.2) and do the variable substitution $p = m - k$ and $q = n - l$, we get

$$\hat{a}_{k,l} = \sum_{p,q} a_{k+p,l+q} j^{p+q+p(q+2l)} \iint H(\tau,\nu) \cdot A_g^*(q\tau_0 + \tau, p\nu_0 + \nu) e^{j\pi(q\tau_0\nu - p\nu_0\tau)} e^{j\pi(2l\tau_0\nu - 2k\nu_0\tau + \tau\nu)} d\nu d\tau \tag{5.4}$$

Assume the channel is moderately dispersive ($\tau_{max} \ll \tau_0$ and $f_D \ll \nu_0$), the ambiguity function $A_g(\tau,\nu)$ has relatively low variation around the lattice points $(q\tau_0, p\nu_0)$ over the integration interval, that is

$$A_g^*(q\tau_0 + \tau, p\nu_0 + \nu) e^{j\pi(q\tau_0\nu - p\nu_0\tau)} \approx A_g^*(q\tau_0, p\nu_0) \tag{5.5}$$

for $|\tau| \leq \tau_{max}$, $|\nu| \leq f_D$, $p, q \in \mathbb{Z}$. Therefore (5.4) can be rewritten as

$$\begin{aligned} \hat{a}_{k,l} &= \sum_{p,q} a_{k+p,l+q} j^{p+q+p(q+2l)} A_g^*(q\tau_0, p\nu_0) \\ &\cdot \iint H(\tau,\nu) e^{j\pi(2l\tau_0\nu - 2k\nu_0\tau + \tau\nu)} d\nu d\tau = a_{k,l}^{(c)} \; H_{k,l}^{(c)} \end{aligned} \tag{5.6}$$

where

$$H_{k,l}^{(c)} \triangleq \iint H(\tau,\nu) e^{j\pi(2l\tau_0\nu - 2k\nu_0\tau + \tau\nu)} d\nu d\tau \tag{5.7}$$

represents the channel coefficient at lth symbol and kth sub-carrier frequency, and

$$a_{k,l}^{(c)} \triangleq \sum_{p,q} a_{k+p,l+q} j^{p+q+p(q+2l)} A_g^*(q\tau_0, p\nu_0) \tag{5.8}$$

indicates the superposition of the transmitted symbol $a_{k,l}$ and ISI/ICI components after demodulation at the lattice point $(l\tau_0, k\nu_0)$. Note that $a_{k,l}^{(c)}$ only depends on the pulse shape function $g(t)$ and the transmitted symbols $a_{p,q}$, and therefore can be calculated before transmission. Instead of using $a_{k,l}$ for channel estimation by reducing as much as possible the power of the ISI/ICI terms as in [44, 45], the channel estimation method IAM [47,49] utilises the full knowledge of $a_{k,l}^{(c)}$ and treats the whole as a "pseudo pilot" to do channel estimation, as shown in Fig.fig:CHest.

With noise taken into consideration, the channel estimation becomes

$$\hat{H}_{k,l}^{(c)} = \frac{\hat{a}_{k,l}}{a_{k,l}^{(c)}} = H_{k,l}^{(c)} + \frac{w_{k,l}}{a_{k,l}^{(c)}} \tag{5.9}$$

where $w_{k,l}$ is the noise term in the output of demodulation. Note that the larger the power of $a_{k,l}^{(c)}$ the better the estimation will be. Therefore, we focus on increasing the power of the ISI/ICI rather than reducing it.

This IAM principle, although invented for OFDM/OQAM methods, can be applied to any other GFDM systems as long as there is intrinsic interference which can be predicted by preamble sequences.

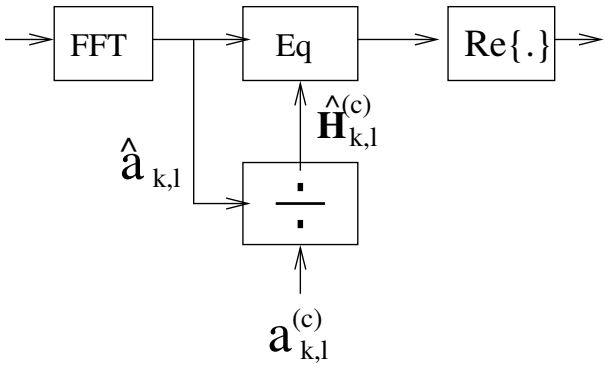

Figure 5.1: Diagram of IAM channel estimation.

5.3 IAM preamble design revisit

The frame structures of the IAM-R preamble [47] and the IAM-I preamble [49] are shown in Fig. 5.2. The frame structure for CP-OFDM is also depicted. Note that the preamble length in OFDM/OQAM is $3\tau_0$ instead of $2\tau_0$ as in CP-OFDM. In an OFDM/OQAM system, the pulse shape $g(t)$ is chosen to have a very good time frequency localisation (TFL) property and therefore the ambiguity function $A_g(\tau, \nu)$ attenuates well both in time and frequency as (τ, ν) outside the origin. Since only the surrounding symbols can introduce notable interference in $a^{(c)}_{k,l}$, the neighbouring two columns of 0 suppress the ISI to a very small amount [47].

For real and even pulse shape $g(t)$ with unit energy, the ambiguity function $A_g(\tau, \nu)$ has very good properties:

$$A_g(\pm\tau, \pm\nu) = A_g(\tau, \nu) = A^*_g(\tau, \nu), \quad A_g(0, 0) = 1 \tag{5.10}$$

This will help to simplify the following derivation.

IAM-R

As proposed in [47], $a_{m,l} = \pm 1$ for $m = 0..N-1$ and $a_{m,l-1} = a_{m,l+1} = 0$, then (5.8) can be rewritten as

$$a^{(c)}_{k,l} = \sum_p a_{k+p,l}(-1)^{pl} j^p A_g(0, p\nu_0) \tag{5.11}$$

For OFDM/OQAM the orthogonality within the real domain is ensured [12], i.e.,

$$A_g(2n\tau_0, 2m\nu_0) = 0 \text{ for } (m, n) \neq (0, 0)$$

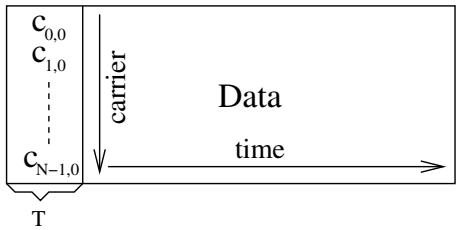

(a) Preamble structure used in CP-OFDM

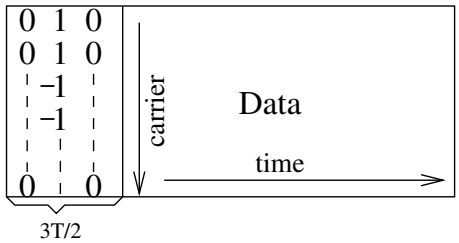

(b) IAM-R used in OFDM/OQAM

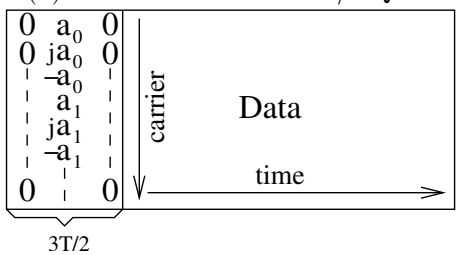

(c) IAM-I used in OFDM/OQAM

Figure 5.2: Preamble structures for CP-OFDM (a) and OFDM/OQAM with (b) IAM-R and (c) IAM-I.

which indicates all the terms with even p (except $p = 0$) are removed from (5.11). Hence we have

$$a_{k,l}^{(c)} = a_{k,l} \pm j \sum_{p>0, p \text{ odd}} (a_{k+p,l} - a_{k-p,l}) A_g(0, p\nu_0) \tag{5.12}$$

where $+$ is retained for even l and $-$ for odd l. To maximise the power of $a_{k,l}^{(c)}$, it is straightforward to figure out that $a_{k+p,l}$ and $a_{k-p,l}$ should have different signs, i.e., $a_{k+p,l} = -a_{k-p,l}$, for $p > 0, p$ odd and for $l = 0..N-1$. Following this rule, one example of the IAM-R preamble is shown in Fig. 5.2(b). The demodulation output in (5.12) becomes

$$a_{k,l}^{(c)} \approx 1 \pm j2A_g(0, \nu_0))$$

where small values $A_g(0, p\nu_0), p > 1$ are omitted for simplicity.

IAM-I

As shown in (5.9), the larger the power of $a_{k,l}^{(c)}$ the better the channel estimation performs. Motivated by IAM-R, a new method named IAM-I was proposed in [49] by allowing elements in the preamble sequence to be imaginary. For example if we set $a_{k,l} = j$ and $a_{k-1,l} = -a_{k+1,l} = 1$ where l is odd, omitting small values $A_g(0, p\nu_0), p > 1$, the demodulation output in (5.12) becomes

$$a_{k,l}^{(c)} \approx j(1 + 2A_g(0, \nu_0))$$

A triplet $[1, j, -1]$ for odd l was proposed to formulated the preamble sequence, as shown in Fig. 5.2(c), where $a_0, a_1, ...a_{N/3} \in \{1, -1\}$ are randomly selected. As a result, the corresponding demodulated symbols triplet will be

$$[(1 + \delta) \pm j\delta,\ j(1 + 2\delta),\ -(1 + \delta) \pm j\delta]$$

where $\delta = A_g(0, \nu_0) > 0$ and values of $A_g(0, p\nu_0)$ for $p > 1$ are omitted. For even l, according to (5.12), we should use $[-1, j, 1]$ instead, which was not discussed or even noticed in [49].

IAM-new

Motivated by IAM-I and observing that with the triplet used $a_{k\pm1,l}^{(c)} \approx (1 + \delta) \pm j\delta$ have smaller power compared with $a_{k,l}^{(c)}$, one may think of finding the optimal complex valued $a_{m,l}$ carefully so that the demodulated symbols $a_{k,l}^{(c)}$ will have the maximum power.

Recall the expression for $a_{k,l}^{(c)}$ in (5.11), with complex valued $a_{k+p,l}$, the optimal sequence will require that all the elements in the summation should be coherently added, that is

$$\text{phase}(a_{k+p,l}(-1)^{pl} j^p A_g(0, p\nu_0)) = \varphi, \text{ for all } k, p$$

where φ is an arbitrary constant within $[0, 2\pi)$. Without loss of generality, we will assume $\varphi = 0$ in the following and the resulting optimal preamble structure will serve as a basis for a family of preamble sequences which differ only by a constant multiplier $e^{j\varphi}$.

Since $A_g(0, p\nu_0))$ is real valued will all the significant terms positive, we have

$$a_{k+p,l} = (-1)^{pl} j^{-p} \cdot \text{sign}(A_g(0, p\nu_0))$$

where function sign(x) equals to 1 for $x \geq 0$ and -1 otherwise. Suppose $A_g(0, p\nu_0) \geq 0$ holds for all p, then it is easy to figure out that the optimal preamble basis should be

$$a_{k,l} = \begin{cases} j^{-k} & \text{, for even } l \\ j^k & \text{, for odd } l \end{cases} \quad k = 0, ..., N-1 \tag{5.13}$$

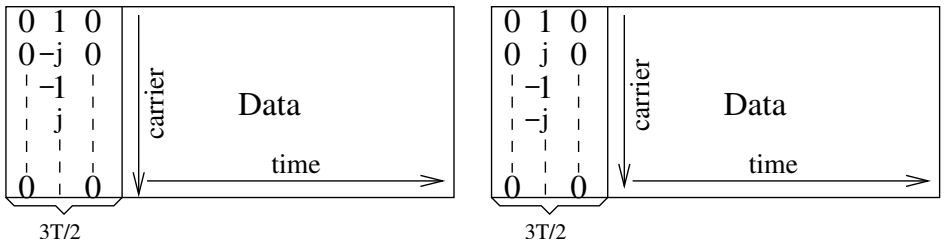

(a) even l (b) odd l

Figure 5.3: IAM-new preamble structure for OFDM/OQAM.

with the resulting demodulated symbol

$$a_{k,l}^{(c)} = (-1)^l j^{-k} \sum_p A_g(0, p\nu_0) \approx (-1)^l j^{-k}(1 + 2A_g(0, \nu_0))$$

This new method was named as IAM-new and the preamble structures are shown in Fig. 5.3, where the quadruplet $[1, -j, -1, j]$ for even l and the quadruplet $[1, j, -1, -j]$ for odd l appears repeatably to formulate the preamble sequence.

5.4 Optimal preamble design

To further increase the power of demodulated preamble symbol $a_{k,l}^{(c)}$, the two neighbouring columns can also be utilised by assigning proper complex valued symbols rather than zeros.

For convenience, the following notations are used to simplify our derivation:

$$A_g(0, \pm\nu_0) = \delta,\ A_g(\pm\tau_0, 0) = \beta,\ A_g(\pm\tau_0, \pm\nu_0) = \gamma,\ A_g(\pm\tau_0, \pm 2\nu_0) = \eta$$

For different pulse shapes $g(t)$ the above parameters are different in general. A heuristic observation shows that $1 > \delta, \beta, \gamma, \eta > 0$ always hold for half-cosine functions, EGF functions and their associated TFL1 functions, as shown in Table 5.1. For well designed pulse shapes, $A_g(n\tau_0, m\nu_0)$ attenuates very fast with increasing m, n and therefore the value for $m > 1, n > 1$ will be omitted in the following analysis.

For the demodulated symbol $a_{k,l}^{(c)}$, a weighting matrix $\boldsymbol{W}$ can be formulated to calculated notable interference elements from neighbouring symbols. As shown in (5.8), the sign of the elements in $\boldsymbol{W}$ will be different for different value of l. Therefore two different realisations are listed as $\boldsymbol{W}_{l_{even}}$ when l is an even number

Table 5.1: Ambiguity function parameters for different pulses

Pulse shapes	$A_g(0,0)$	δ	β	γ	η
5-tap EGF (α=1)	1	0.2261	0.4322	0.2931	0.0418
5-tap EGF (α=2)	1	0.45	0.3648	0.2628	0.071
5-tap EGF (α=7)	1	0.6157	0.1422	0.1298	0.1003
1-tap TFL (α=1)	1	0.502	0.3124	0.2482	0.1102
1-tap TFL (α=2)	1	0.5554	0.2571	0.2131	0.1155
1-tap TFL (α=7)	1	0.6205	0.1233	0.1142	0.0913
1-tap Halfcosine	1	0.5	0.3173	0.25	0.1071

and $\boldsymbol{W}_{l_{odd}}$ when l is odd.

$$\boldsymbol{W}_{l_{even}} = \begin{bmatrix} -j\eta & 0 & j\eta \\ -j\gamma & -j\delta & -j\gamma \\ -j\beta & 1 & j\beta \\ -j\gamma & j\delta & -j\gamma \\ -j\eta & 0 & j\eta \end{bmatrix}, \qquad \boldsymbol{W}_{l_{odd}} = \begin{bmatrix} -j\eta & 0 & j\eta \\ j\gamma & j\delta & j\gamma \\ -j\beta & 1 & j\beta \\ j\gamma & -j\delta & j\gamma \\ -j\eta & 0 & j\eta \end{bmatrix}$$

Obviously, $\boldsymbol{W}_{l_{even}}$ and $\boldsymbol{W}_{l_{odd}}$ only differs from each other by changing the sign of all the elements in the second row and the fourth row. Since the first and the third column of the weighting matrix $\boldsymbol{W}$ also contribute to intrinsic interference, more power will be brought to $a_{k,l}^{(c)}$ by assigning proper complex valued symbols rather than zeros.

Given the symmetric and fast decay nature of the weighting matrix $\boldsymbol{W}$ and the fact that the IAM-new preamble symbols in the central column are repetition of a quadruplet, the symbols in the other two columns should also be grouped into quadruplet. As shown in Appendix 5.7 A, given the weighting matrix $\boldsymbol{W}$, the optimal preamble matrix is

$$\boldsymbol{A}_{l_{even}} = \begin{bmatrix} \vdots & \vdots & \vdots \\ x^* & 1 & -x \\ -jx & -j & jx^* \\ x^* & -1 & -x \\ -jx & j & jx^* \\ \vdots & \vdots & \vdots \end{bmatrix}, \qquad \boldsymbol{A}_{l_{odd}} = \begin{bmatrix} \vdots & \vdots & \vdots \\ -x^* & 1 & x \\ -jx & j & jx^* \\ -x^* & -1 & x \\ -jx & -j & jx^* \\ \vdots & \vdots & \vdots \end{bmatrix} \tag{5.14}$$

where $x = e^{j\theta}$, and one of the optimal value of θ stated in (5.29) is

$$\theta = \operatorname{atan}\frac{2\gamma}{\beta + 2\eta} \tag{5.15}$$

The power of the demodulated symbol becomes

$$|a_{k,l}^{(c)}|^2 = (1+2\delta)^2 + 4[(\beta+2\eta)^2 + 4\gamma^2]$$

Table 5.2: Calculation of $|a_{k,l}^{(c)}|^2$ for different preamble sequences.

	IAM-R	IAM-I	IAM-new	$\theta = \pi/4$	Opt. θ
5-tap EGF ($\alpha = 1$)	1.2045	1.7393	2.1089	4.5377	4.5476
5-tap EGF ($\alpha = 2$)	1.8100	2.7400	3.6100	5.7417	5.7424
5-tap EGF ($\alpha = 7$)	2.5163	3.6528	4.9791	5.7049	5.7188
1-tap TFL1 ($\alpha = 1$)	2.0080	3.0107	4.0160	6.1345	6.1372
1-tap TFL1 ($\alpha = 2$)	2.2339	3.3037	4.4555	6.1274	6.1350
1-tap TFL1 ($\alpha = 7$)	2.5401	3.6814	5.0221	5.5930	5.6050
1-tap halfcosine	2.0000	3.0000	4.0000	6.1280	6.1300

For different pulses, the value of $1 > \delta,\beta,\ \gamma,\ \eta > 0$ are usually different, as shown in Table 5.1. Therefore the optimal preamble sequences are also different, which will provider extra complexity for channel estimation when the pulse shape itself is also subject to adaptation. Hence a suboptimal solution which can provide a uniform preamble sequence for all the pulse shapes at a comparable performance will be of great interest. By taking $\theta = \pi/4$ we can have a pulse shape independent preamble structure which has the demodulated symbol power as

$$|a_{k,l}^{(c)}|^2 = (1 + 2\delta)^2 + 2(\beta + 2\eta + 2\gamma)^2$$

It is simple to show that

$$(\beta + 2\eta)^2 + 4\gamma^2 \geq \frac{1}{2}(\beta + 2\gamma + 2\eta)^2$$

with equality achieved only if $2\gamma = \beta + 2\eta$.

The power of demodulated symbols ($|a_{k,l}^{(c)}|^2$) with different pulse shapes are calculated in Table 5.2 with all the necessary data obtained from Table 5.1.

By using "optimal" here we mean that it is optimal for the given assumption of the weighting matrix $\boldsymbol{W}$, where only the significant elements are taken into consideration. If all the terms are taken into account, shown in Appendix 5.7 A, the optimal solution becomes

$$\theta = \operatorname{atan} \frac{2\sum_{p=1}^{N/4} A_g(\tau_0, (2p-1)\nu_0)}{A_g(\tau_0, 0) + 2\sum_{p=1}^{N/4} A_g(\tau_0, 2p\nu_0)} \tag{5.16}$$

It is obvious that (5.15) is just a special case of (5.16) with only one item taken into account in the summation.

5.5 Simulation results

simulation parameters

All the simulation results in this section were carried out on the Matlab/Octave Simulation Workbench for Software Defined Radio [18], with the following main parameters of the system given below:

- Sampling interval: $T_s = 0.5213\mu$s
- Frequency separation: $F = \nu_0 = 15$ kHz
- OQAM symbol duration: $\tau_0 = 33.3333\mu$s
- CP-OFDM symbol duration: $T_0 = T + T_{cp} = 2\tau_0 + T_{cp}$
- FFT/IFFT size: $N = 128$
- CP used in OFDM: 4 to 32 samples ($T_{cp} = T_d$)
- Number of data frames: $N_r = 10$ OFDM symbols
- Channel type: ideal, time dispersive, doubly dispersive
- Number of multipaths: < 10
- QPSK, 16QAM modulation without channel coding

Unlike in [47, 49] where $N = 2048$ FFT/IFFT was used with a convolutional channel coding at rate 1/2, we simply use a relatively small FFT/IFFT size and no channel coding. The reason for this was two fold. On one hand we are more interested in the relative performance gain among different channel estimation methods rather than exact performance in a specific system configuration. On the other hand, large FFT size and complicated channel coding take too much time for a Matlab/Octave based simulation workbench on a normal PC.

Three kinds of pulse shapes were used in this simulation: the half-cosine function with duration $L = N$, the EGF with length $L = 5N$, and the TFL1 with $L = N$. The TFL1 function was also used in [47, 49]. The first three IAM preambles, namely IAM-R, IAM-I and IAM-new, have the same energy on preamble sequences and share a similar structure (0 x 0) and there will be frequently compared with each other in our following discussion. The last two IAM preambles, namely IAM-Optimal (with optimal θ) and IAM-Subopt (with $\theta = \pi/4$), have the same structure as defined by (5.31) and (5.32) but three times the energy of the other three preambles. The comparison between these two groups will be discussed in a later stage.

As in Chapter 4, a tapped delay line WSSUS doubly dispersive channel is implemented for simulation. An exponential delay power profile and a classic Doppler power spectrum is assumed for the channel scattering function as defined in (2.9),

Table 5.3: Average power of the demodulated preamble symbols for in simulation

	IAM-R	IAM-I	IAM-new	Subopt	Optimal
5-tap EGF ($\alpha = 1$)	1.2475	1.7978	2.2229	4.0829	4.1626
5-tap EGF ($\alpha = 2$)	1.7214	2.6827	3.4149	5.4080	5.4077
5-tap EGF ($\alpha = 7$)	1.9973	3.5207	3.9947	5.9927	5.9550
1-tap TFL1 ($\alpha = 1$)	2	3.1042	4	5.9769	5.9727
1-tap TFL1 ($\alpha = 2$)	2	3.2601	4	5.9633	5.9545
1-tap TFL1 ($\alpha = 7$)	2	3.5826	4	5.7789	5.7421
1-tap halfcosine	2	2.9844	4	5.9982	6.0

with RMS delay spread τ_{RMS} and maximum Doppler frequency shift f_D. We set time spread $T_d = 4\tau_{\text{RMS}}$ in our simulation, which together with the Doppler spread $B_d = 2f_D$ are used in the following to describe the amount of channel dispersion.

Power of the demodulated symbols

The average power of the demodulated preamble symbols via an ideal channel for different preamble sequences are shown in Table 5.3. Compared with the data in Table 5.2 which is from theoretical calculation, the average power of the demodulated signal in reality varies more smoothly with the change of pulse shapes.

It is clear that the IAM-new preamble always produce twice the output power as IAM-R, and the optimal and suboptimal methods produce three times higher power. The most surprising observation comes from the fact that the suboptimal preamble structure sometimes produces slightly larger power than the optimal preamble does. One possible explanation is that the terms $A_g(n\tau_0, m\nu_0)$ with $m > 1, n > 1$ is not very small in some cases and the term $A_g((2n-1)\tau_0, 0)$ for $n > 1$ might be negative for some pulse shapes, both of which will cause a bias in the optimal solution.

The possible influence of the Gaussian parameter α on the performance of different IAM methods is interesting but not easy to quantify, since the pulse shape will affect both the performance of demodulation and the performance of channel estimation and therefore hard to clarify each contribution. Therefore, unless mentioned otherwise, we will use $\alpha = 1$ for the 5-tap EGF pulse and the 1-tap TFL1 pulse in OFDM/OQAM systems in the following simulations, the same as in [47, 49].

Uncoded BER performance over doubly dispersive channels

Uncoded BER simulation versus E_b/N_0, with E_b the useful bit energy and N_0 the mono-lateral noise density, has been carried out for different preamble sequence under dispersive channels, as shown in Fig. 5.4, where two dispersive channels with delay spread $T_d = 4.167\mu$s and $T_d = 12.5\mu$s, and different Doppler spread

($0Hz$ and $300Hz$) are used. With carrier frequency $f_c = 2GHz$, a Doppler spread $B_d = 300Hz$ is equivalent to a moving speed of 81km/h. In both cases, the length of CP always equal the length of the channel delay spread, i.e., $T_{cp} = T_d$. The IAM-new method (marker o) can always outperform CP-OFDM (marker $\diamond$) by at least 2.4 dB. The gain will increase a little bit when there is Doppler shift added. A moderate gain of 0.4 dB was always achieved by IAM-new against IAM-I (marker $\times$).

Robustness against channel delay spread

In this part we carry simulations to check the robustness of the IAM preambles against channel delay spread. The channel delay spread percentage is defined by T_d/T, where T_d is the delay spread of the channel and $T = 2\tau_0$ is the OFDM symbol duration without adding the CP.

Fig. 5.5 shows the uncoded BER performance with IAM-R (marker $\bullet$), IAM-I (marker $\times$) and IAM-new (marker o) versus the percentage of channel delay spread, at a given E_b/N_0 with a QPSK modulation. CP-OFDM with different length of CP ($T_{cp} = T_d$) at some constant E_b/N_0 are also plotted as benchmark. When the channel is purely time dispersive, as shown in Fig. 5.5 a, IAM-new can outperform CP-OFDM by 2.4 dB and IAM-I by 0.4 dB up to 25% delay spread with QPSK modulation. The gain decreases a little bit when the delay spread percentage is extremely small ($< 6\%$), where the benefit of pulse shaping cannot be fully exploited. When there is Doppler spread present, as shown in Fig. 5.5 b, the same gains hold up to 16% delay spread. The curves for 5-tap EGF, lying between TFL1 and CP-OFDM, have somewhat similar changing trend as CP-OFDM and therefore omitted to make the figures readable.

When a 16-QAM modulation was used, as shown in Fig. 5.6, a notable gain degradation happened for all the IAM based methods regardless what kind of pulse shapes were used in OFDM/OQAM. The benefit of IAM-new compared to IAM-R and IAM-I is somehow retained. Besides, when TFL1 (solid line) was used the gain over CP-OFDM was quickly diminishing when the time spread percentage is increased. It was however relatively slowly for 5-taps EGF (dashed line), which as a consequence always outperforms CP-OFDM in time dispersive (up to 25%) with or without Doppler spread. The results here also indicate the necessity of pulse shape adaptation regarding the dispersiveness of the channels. For example, it is better to use TFL1 pulse shapes in less time dispersive channels (up to 14% for $B_d = 0$Hz and up to 10% for $B_d = 100$Hz) and use 5-tap EGF pulse shapes otherwise.

Pulse shape adaptation in channel estimation

The potential gain from pulse shape adaptation on the performance of channel estimation is evaluated through dispersive channel, using the IAM-new estimation method and EGF functions with different α, as shown in Fig. 5.7. The performance of TFL1($\alpha = 1$) and CP-OFDM are also plotted as benchmarks. When the channel

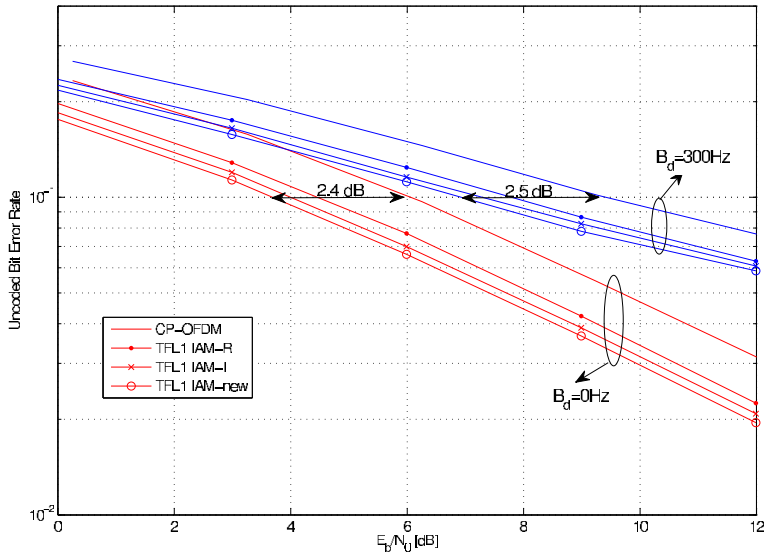

(a) $T_d = 4.167\mu$s

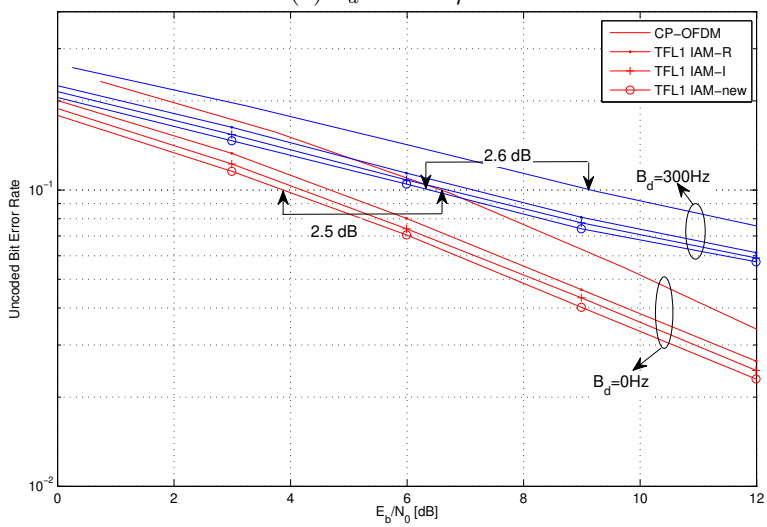

(b) $T_d = 12.5\mu$s

Figure 5.4: Uncoded BER vs. E_b/N_0 with a QPSK modulation over dispersive channels.

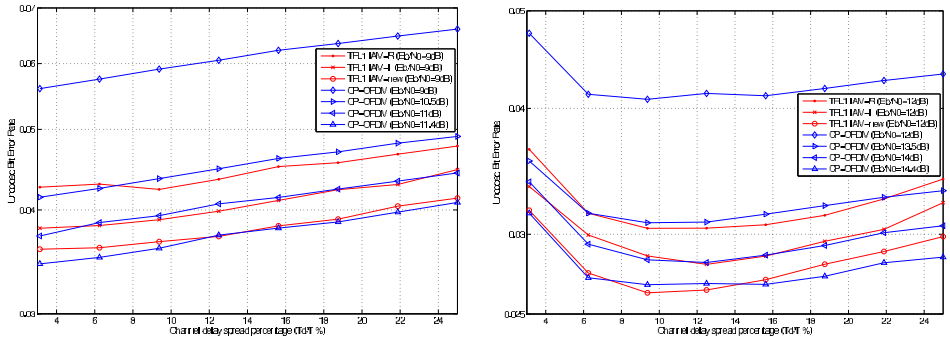

(a) $B_d = 0Hz$ (b) $B_d = 100Hz$

Figure 5.5: Uncoded BER vs. the percentage of channel delay spread $T_d/T[\%]$ at a given E_b/N_0 with a QPSK modulation through dispersive channels.

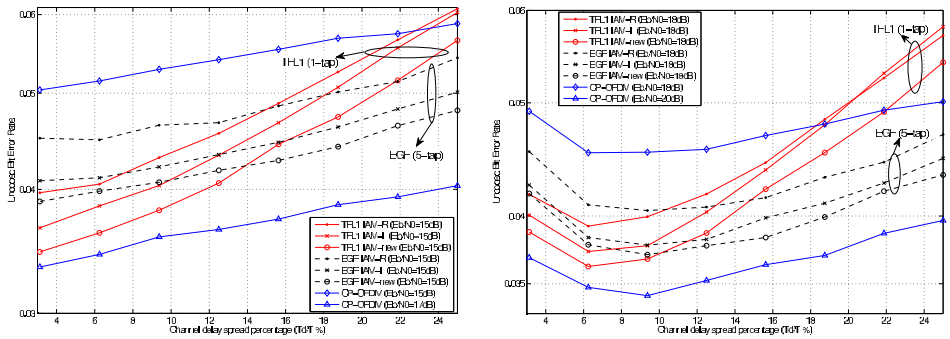

(a) $B_d = 0Hz$ (b) $B_d = 100Hz$

Figure 5.6: Uncoded BER vs. the percentage of channel delay spread $T_d/T[\%]$ at a given E_b/N_0 with a 16QAM modulation through dispersive channels.

is less dispersive, pulse shapes with higher demodulation power (in EGF case $\alpha = 7$ as shown in Table 5.3) give better performance as expected. When the channel has large delay spread and therefore is much more frequency selective, pulse shapes with better TFL properties (in EGF case $\alpha = 1$ as shown in Fig. 3.2) will result in smaller ISI/ICI and therefore better performance. The TFL1 (with $\alpha = 1$) pulse shape always performs the best when using a QPSK modulation where low SNR is required. When a high order modulation (e.g. 16QAM) is used as shown in Fig. 5.7 c, d, higher SNR is required to achieve the same BER or symbol error rate (SER) and therefore a pulse shape with better TFL property is preferred. This must also be taken into consideration when designing the pulse shape adaptation strategy.

When the optimal value of α in EGF functions are determined by maximising the desired signal power E_S stated in (3.9), or by minimising the interference power

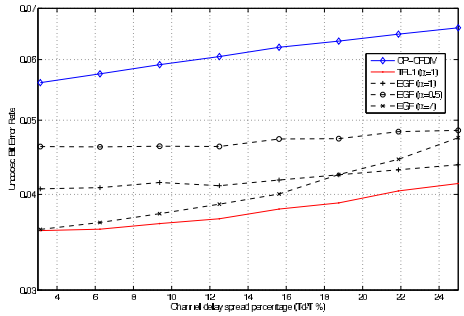

(a) $B_d = 0Hz$, $E_b/N_0 = 9$dB, QPSK

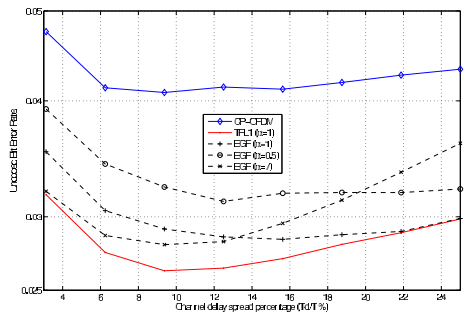

(b) $B_d = 100Hz$, $E_b/N_0 = 12$dB, QPSK

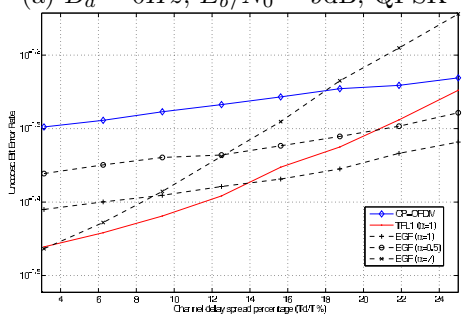

(c) $B_d = 0Hz$, $E_b/N_0 = 15$dB, 16QAM

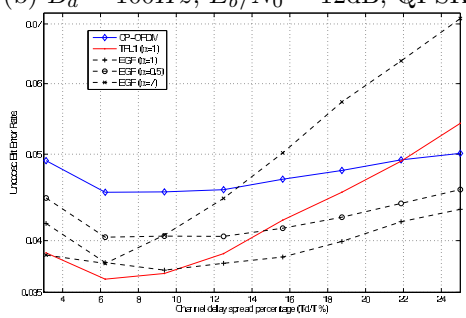

(d) $B_d = 100Hz$, $E_b/N_0 = 18$dB, 16QAM

Figure 5.7: Uncoded BER vs. the percentage of channel delay spread $T_d/T[\%]$ with different pulse shapes.

E_I stated in (3.10), we compare the performance of pulse shape adaptation with CP-OFDM and TFL1, as shown in Fig. 5.8, where EGF with two boundary values $\alpha = 0.5$ and $\alpha = 7$ are also plotted as benchmarks. Obviously the adaptation based on minimisation of the interference power (E_I) gives the best performance in a large range of channel time dispersion. The E_S method, on the other hand, achieves satisfactory performance only when the time dispersion is relatively large.

Evaluation and verification of the optimal preamble structure

To clarify the effects of different preamble sequences on the performance of channel estimation, the same pulse shape (either TFL1 or EGF) is used with different preamble sequences, as shown in Fig. 5.9. For TFL1 pulse shape, the performance of IAM-Optimal and IAM-Subopt is almost identical. When a low order modulation (hence low SNR) is used, the IAM-Optimal and IAM-Subopt preambles provide better performance. The relative gain decreases as the channel time dispersion increases. Therefore, when TFL1 is used, the two preambles with largest demodulation power are only preferred in less dispersive channels with low modulation order.

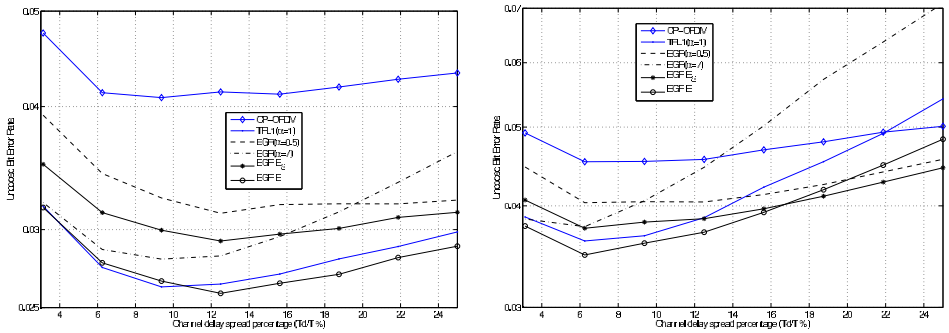

(a) QPSK, $E_b/N_0 = 12$dB (b) 16QAM, $E_b/N_0 = 18$dB

Figure 5.8: Uncoded BER vs. the percentage of channel delay spread $T_d/T[\%]$ through dispersive channels with $B_d = 100Hz$. IAM-new is used for EGF and TFL1.

When 5-tap EGF pulse shape is used, the gain brought by higher demodulation power is significant everywhere over doubly dispersive channels as long as a low order modulation (e.g. QPSK) is used. When a high order modulation is used, this gain diminishes quickly. However, in all cases when 5-tap EGF pulse shape is used, IAM-Optimal preamble always performs better than IAM-Subopt, which differs significantly from the case when TFL1 pulse shape is used.

Another observation from Fig. 5.9 is that the performance of IAM-Optimal and IAM-Subopt preambles is actually worse than IAM-new preamble when the channel is highly dispersive. One possible explanation is that the optimal structure defined in (5.31) and (5.32) is based on the assumption that the channel is moderately dispersive. In highly dispersive channels, the approximation in (5.5) may not hold anymore and therefore degrade the performance of IAM channel estimation methods. The preambles defined by IAM-R, IAM-I and IAM-new, depend only on the two neighouring elements in the same OFDM/OQAM system and therefore have much stronger immunity to channel dispersions. The preambles defined by IAM-Optimal and IAM-Subopt, however, depend on all the neighbouring elements and therefore is more sensitive to channel dispersion.

The gain of the IAM-Optimal/Subopt comes from the fact that more energy has been allocated to their preambles ($x,\ y,\ z$ rather than $0,\ x,\ 0$). For applications where the performance is a crucial factor, it is a good choice to use them. But in cases where power/energy is a crucial factor, it might not be wise to use such preamble structures. To demonstrate its energy efficiency, the uncoded BER performance of the IAM-Subopt with different number of frames within one data frame are compared under the same level of E_b/N_0 with

$$E_b = \frac{(N_r + 3)E_s}{N_r \log_2(M)}$$

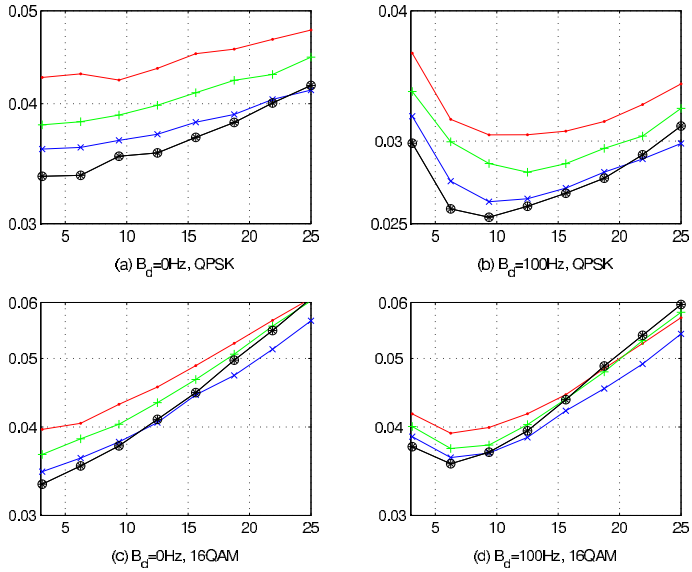

(1) 1-tap TFL1 ($\alpha = 1$)

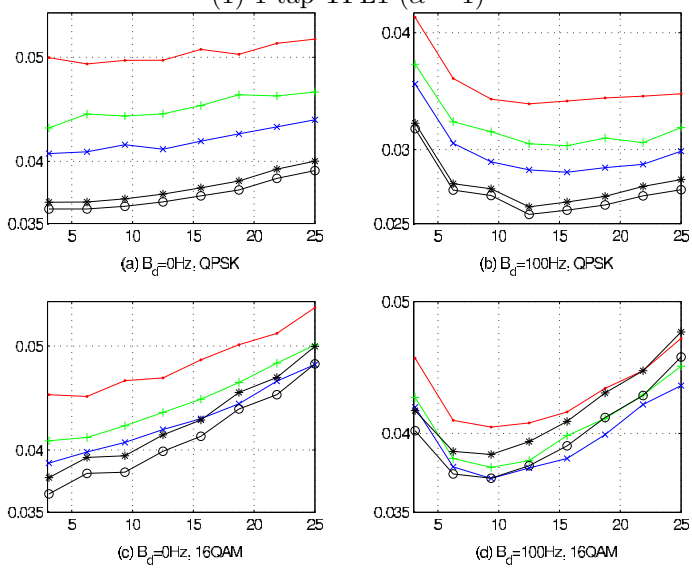

(2) 5-tap EGF ($\alpha = 1$)

Figure 5.9: Uncoded BER vs. the percentage of channel delay spread $T_d/T[\%]$ at a given SNR over dispersive channels for OFDM/OQAM with IAM-R (marker $\cdot$), IAM-I ($+$), IAM-new ($\times$), IAM-Subopt ($*$), and IAM-Optimal (o).

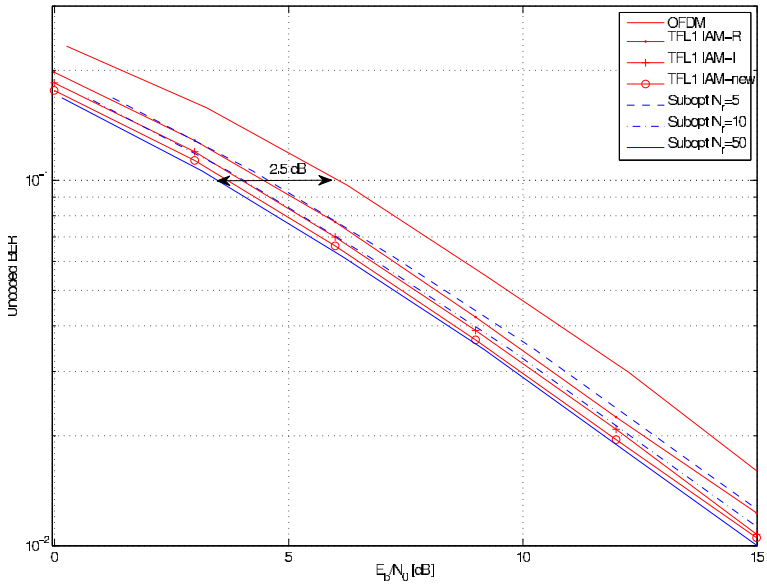

Figure 5.10: Uncoded BER vs. E_b/N_0 with a QPSK modulation

where M is the modulation order. As shown in Fig. 5.10 where the channel is purely time dispersive, the optimal preamble only outperforms IAM-new preamble for a large value of N_r.

5.6 Summary

In this chapter we have presented a general theoretical framework for preamble-based IAM channel estimation methods for OFDM/OQAM systems. We also used this framework to revisit the two heuristic IAM structures and identified the optimal IAM preamble sequence after analytical derivation. It has been shown that, when QPSK was used, the newly proposed optimal structure IAM-new can achieve about 2.4 dB gain over CP-OFDM in doubly dispersive channels up to 25% delay spread when no Doppler spread presented and up to 16% delay spread when Doppler spread $B_d = 100Hz$. Compared to IAM-R and IAM-I, a moderate gain of 0.9 dB and 0.4 dB respectively always maintained. When 16-QAM was used, the gain decreases as the delay spread percentage increases, and these pulse shapes with better time frequency location properties are preferred when channel is largely time dispersive.

The power of demodulated symbols, however, only plays important role in system performance in low SNR region where the distortion brought in by noise is significant. In high SNR region, the power of noise is relatively small compared with the power of the interference and therefore higher demodulated symbol power

may not necessarily mean higher system performance. Depending on the channel characteristics and the SNR level, the importance of better TFL property and higher demodulation power may varies. Therefore a careful investigation of different scenarios is necessary before setting system parameters or making pulse shape adaptation strategies.

All the IAM methods discussed in this paper, however, are still not very attractive for high mobility communications, where the channel estimation sequence has to be inserted into many places within the same data frame. As the IAM preamble structure takes 3 OFDM/OQAM symbol duration, i.e., one and a half OFDM symbol duration, the gain on spectral efficiency by not using CP will diminish when such preamble structures are frequently used for every several data symbols. On the other hand, the framework for IAM preamble design has been verified to be effective. Therefore we will focus on designing more time and energy efficient preambles in future work based on the framework proposed in this chapter. The application of this framework to other GFDM systems is another interesting topic.

5.7 Appendix

A. Derivation of the optimal IAM preamble structure

For odd l, given the preamble matrix

$$\boldsymbol{A}_{l_{odd}} = \begin{bmatrix} \vdots & \vdots & \vdots \\ x_1 & 1 & x_5 \\ x_2 & j & x_6 \\ x_3 & -1 & x_7 \\ x_4 & -j & x_8 \\ \vdots & \vdots & \vdots \end{bmatrix} \tag{5.17}$$

where $|x_i| \leq 1, i = 1, ..., 8$ are complex valued variables, the demodulated symbols at corresponding points are as follows:

$$\begin{aligned} a_1^{(c)} &= 1 + 2\delta + j\underbrace{[\beta(x_5 - x_1) + \gamma(x_2 + x_4 + x_6 + x_8) + 2\eta(x_7 - x_3)]}_{y_1} \\ a_j^{(c)} &= j[1 + 2\delta + \underbrace{\beta(x_6 - x_2) + \gamma(x_1 + x_3 + x_5 + x_7) + 2\eta(x_8 - x_4)}_{y_2}] \\ a_{-1}^{(c)} &= -1 - 2\delta + j\underbrace{[\beta(x_7 - x_3) + \gamma(x_2 + x_4 + x_6 + x_8) + 2\eta(x_5 - x_1)]}_{y_3} \\ a_{-j}^{(c)} &= j[-1 - 2\delta + \underbrace{\beta(x_8 - x_4) + \gamma(x_1 + x_3 + x_5 + x_7) + 2\eta(x_6 - x_2)}_{y_4}] \end{aligned} \tag{5.18}$$

Then the preamble design problem becomes a optimisation process which try to find a realisation of $x_i, i = 1, ..., 8$ that can maximise the minimum power of the demodulated symbols, i.e.,

$$\{x_i, i = 1, ..., 8\} = \arg \max_{x_i, i=1...8} \min\{|a_1^{(c)}|^2, |a_j^{(c)}|^2, |a_{-1}^{(c)}|^2, |a_{-j}^{(c)}|^2\} \tag{5.19}$$

under the constraint that $|x_i| \leq 1, i = 1, ..., 8$.

In order to maximise the power, all the elements in each $a^{(c)}$ in (5.18) should be coherently added, that is,

$$\begin{array}{l} \text{phase}(x_5 - x_1) = \text{phase}(x_2 + x_4 + x_6 + x_8) = \text{phase}(x_7 - x_3) \\ \text{phase}(x_6 - x_2) = \text{phase}(x_1 + x_3 + x_5 + x_7) = \text{phase}(x_8 - x_4) \end{array} \tag{5.20}$$

Given (5.18), it is easy to figure out that the condition that maximise $|a_1^{(c)}|^2$ (e.g. when $jy_1 > 0$) will minimise $|a_{-1}^{(c)}|^2$, and vice versa. The same situation happens for $|a_j^{(c)}|^2$ and $|a_{-j}^{(c)}|^2$. Therefore the optimal solution to maximise the minimum power is to set y_1, y_3 purely real valued and y_2, y_4 purely imaginary, that is,

$$\begin{array}{ll} \text{phase}(y_1) = \text{phase}(y_3) & = 0 \text{ or } \pi \\ \text{phase}(y_2) = \text{phase}(y_4) & = \pi/2 \text{ or } -\pi/2. \end{array}$$

Thereafter the following equations can be formulated

$$\left\{ \begin{array}{ll} \Im(x_5) = \Im(x_1),\ \Im(x_7) = \Im(x_3) & y_1, y_3 \text{ purely real} \\ \Re(x_5)\Re(x_1) < 0,\ \Re(x_7)\Re(x_3) < 0 & \text{coherent addition} \\ \Re(x_1 + x_3 + x_5 + x_7) = 0 & \\ \Re(x_6) = \Re(x_2),\ \Re(x_8) = \Re(x_4) & y_2, y_4 \text{ purely imaginary} \\ \Im(x_6)\Im(x_2) < 0,\ \Im(x_8)\Im(x_4) < 0 & \text{coherent addition} \\ \Im(x_2 + x_4 + x_6 + x_8) = 0 & \end{array} \right. \tag{5.21}$$

where $\Re\{\cdot\}$ denotes the real part operator and $\Im\{\cdot\}$ denotes the imaginary part operator. It is clear from (5.19), (5.20) and (5.21) that the power of y_i, $i = 1, .., 4$ can reach the maximum only if $|x_i| = 1, i = 1, ..., 8$, i.e., each element in the preamble utilises the maximum power available. Hence (5.21) can be rewritten as

$$\left\{ \begin{array}{llll} \Im(x_5) = \Im(x_1), & \Re(x_5) = -\Re(x_1) & \Rightarrow x_1 = -x_5^* \\ \Im(x_7) = \Im(x_3), & \Re(x_7) = -\Re(x_3) & \Rightarrow x_3 = -x_7^* \\ \Re(x_6) = \Re(x_2), & \Im(x_6) = -\Im(x_2) & \Rightarrow x_2 = x_6^* \\ \Re(x_8) = \Re(x_4), & \Im(x_8) = -\Im(x_4) & \Rightarrow x_4 = x_8^* \end{array} \right. \tag{5.22}$$

where $\{\cdot\}^*$ indicates the complex conjugate operator. To simplify the expressions, we introduce some other intermediate variables $\phi_i \in [0, 2\pi), i = 1..4$, so that

$$\begin{array}{ll} x_5 = \cos\phi_1 + j\sin\phi_1, & x_1 = -x_5^* = -\cos\phi_1 + j\sin\phi_1 \\ x_6 = \cos\phi_2 + j\sin\phi_2, & x_2 = x_6^* = \cos\phi_2 - j\sin\phi_2 \\ x_7 = \cos\phi_3 + j\sin\phi_3, & x_3 = -x_7^* = -\cos\phi_3 + j\sin\phi_3 \\ x_8 = \cos\phi_4 + j\sin\phi_4, & x_4 = x_8^* = \cos\phi_4 - j\sin\phi_4 \end{array} \tag{5.23}$$

then $y_i, i = 1..4$ can be written as

$$\begin{array}{lll} y_1 & = 2[\beta\cos\phi_1 + \gamma(\cos\phi_2 + \cos\phi_4) + 2\eta\cos\phi_3] & \triangleq 2f_1 \\ y_2 & = 2j[\beta\sin\phi_2 + \gamma(\sin\phi_1 + \sin\phi_3) + 2\eta\sin\phi_4] & \triangleq 2jf_2 \\ y_3 & = 2[\beta\cos\phi_3 + \gamma(\cos\phi_2 + \cos\phi_4) + 2\eta\cos\phi_1] & \triangleq 2f_3 \\ y_4 & = 2j[\beta\sin\phi_4 + \gamma(\sin\phi_1 + \sin\phi_3) + 2\eta\sin\phi_2] & \triangleq 2jf_4 \end{array} \tag{5.24}$$

Now the optimisation problem (5.19) transfers to

$$\{\phi_i, i = 1..4\} = \arg \max_{\phi_i, i=1..4} \min\{f_1^2, f_2^2, f_3^2, f_4^2\} \tag{5.25}$$

Before we solve this problem, let's look at a maximisation problem first.

$$\max\ \mathcal{C} = f_1^2 + f_2^2 + f_3^2 + f_4^2 \quad \text{w.r.t} \quad \phi_i \in [0, 2\pi),\ i = 1..4 \tag{5.26}$$

Take derivation of $\mathcal{C}$ with respect to $\phi_i, i = 1..4$ and set them equal to 0, we have

$$\begin{array}{l} \frac{\partial\mathcal{C}}{\partial\phi_1} = -2f_1\beta\sin\phi_1 + 2f_2\gamma\cos\phi_1 - 4f_3\eta\sin\phi_1 + 2f_4\gamma\cos\phi_1 = 0 \\ \frac{\partial\mathcal{C}}{\partial\phi_2} = -2f_1\gamma\sin\phi_2 + 2f_2\beta\cos\phi_2 - 2f_3\gamma\sin\phi_2 + 4f_4\eta\cos\phi_2 = 0 \\ \frac{\partial\mathcal{C}}{\partial\phi_3} = -4f_1\eta\sin\phi_3 + 2f_2\gamma\cos\phi_3 - 2f_3\beta\sin\phi_3 + 2f_4\gamma\cos\phi_3 = 0 \\ \frac{\partial\mathcal{C}}{\partial\phi_4} = -2f_1\gamma\sin\phi_4 + 4f_2\eta\cos\phi_4 - 2f_3\gamma\sin\phi_4 + 2f_4\beta\cos\phi_4 = 0 \end{array} \tag{5.27}$$

It is not easy to solve the above equations and find all the possible solutions. After adding some additional conditions, however, it is possible to find just one or two solutions which will also solve the maximisation problem stated in (5.26). Such solutions will then be applied to (5.19) and (5.25) for verification.

Given the symmetric property in (5.24), and let's suppose $\phi_1 = \phi_3$ and $\phi_2 = \phi_4$, then it is straightforward to see that

$$\begin{array}{l} f_1 = f_3 = (\beta + 2\eta)\cos\phi_1 + 2\gamma\cos\phi_2 \\ f_2 = f_4 = (\beta + 2\eta)\sin\phi_2 + 2\gamma\sin\phi_1 \\ f_1(\beta + 2\eta)\sin\phi_1 = 2f_2\gamma\cos\phi_1 \\ f_2(\beta + 2\eta)\cos\phi_2 = 2f_1\gamma\sin\phi_2 \end{array} \tag{5.28}$$

Obviously $\phi_1 = \operatorname{atan}\frac{2\gamma}{\beta+2\eta}$ and $\phi_2 = \operatorname{acot}\frac{2\gamma}{\beta+2\eta}$ is one solution for the above equations. Combined with the hypothesis $\phi_1 = \phi_3$ and $\phi_2 = \phi_4$, it is easy to prove that

$$\left\{\begin{array}{l} \phi_1 = \phi_3 = \operatorname{atan}\frac{2\gamma}{\beta+2\eta} \\ \phi_2 = \phi_4 = \operatorname{acot}\frac{2\gamma}{\beta+2\eta} \end{array}\right. \quad \text{or} \quad \left\{\begin{array}{l} \phi_1 = \phi_3 = \operatorname{atan}\frac{2\gamma}{\beta+2\eta} + \pi \\ \phi_2 = \phi_4 = \operatorname{acot}\frac{2\gamma}{\beta+2\eta} + \pi \end{array}\right. \tag{5.29}$$

satisfy the system of nonlinear equations in (5.27) and therefore a solution for the maximisation problem stated in (5.26).

Now apply (5.29) to (5.19) and (5.25) and check if all the requirements are also satisfied. From (5.29) we have $\cos\phi_1 = \sin\phi_2$ and $\sin\phi_1 = \cos\phi_2$, and apply this into (5.28) we get

$$f_1 = f_2 = f_3 = f_4 = \sqrt{(\beta + 2\eta)^2 + 4\gamma^2}$$

and therefore

$$|a_1^{(c)}|^2 = |a_j^{(c)}|^2 = |a_{-1}^{(c)}|^2 = |a_{-j}^{(c)}|^2$$

$$a_1^{(c)} = 1 + 2\delta + j2\sqrt{(\beta + 2\eta)^2 + 4\gamma^2} \tag{5.30}$$

Hence (5.19) and (5.25) are also satisfied by the solution in (5.29).

Substitute (5.29) into (5.23) and apply the results to the preamble matrix $\boldsymbol{A}_{l_{odd}}$ described in (5.17), we get

$$\boldsymbol{A}_{l_{odd}} = \begin{bmatrix} \vdots & \vdots & \vdots \\ -x^* & 1 & x \\ -jx & j & jx^* \\ -x^* & -1 & x \\ -jx & -j & jx^* \\ \vdots & \vdots & \vdots \end{bmatrix} \tag{5.31}$$

where $x = e^{j\theta}$ is the basic element of the optimal preamble sequence and the value of θ is chosen to be one of the two possible solutions stated in (5.29), say let $\theta = \text{atan}\frac{2\gamma}{\beta+2\eta}$. By using "optimal" here we mean that it is optimal for the given assumption of the weighting matrix $\boldsymbol{W}$.

For even l, following the same rule above one can find the optimal preamble matrix as

$$\boldsymbol{A}_{l_{even}} = \begin{bmatrix} \vdots & \vdots & \vdots \\ x^* & 1 & -x \\ -jx & -j & jx^* \\ x^* & -1 & -x \\ -jx & j & jx^* \\ \vdots & \vdots & \vdots \end{bmatrix} \tag{5.32}$$

For different pulses, the value of $1 > \delta$,β, γ, $\eta > 0$ are usually different, as shown in Table 5.1. Therefore the optimal preamble sequences are also different, which will provider extra complexity for channel estimation when the pulse shape itself is also subject to adaptation. Hence a suboptimal solution which can provide a uniform preamble sequence for all the pulse shapes at a comparable performance will be of great interest. Take a close examination of (5.24) and then it is obvious that

$$\theta = \phi_1 = \phi_2 = \phi_3 = \phi_4 = \pi/4$$

will satisfy this requirement as it will result in

$$f_1 = f_2 = f_3 = f_4 = \frac{\sqrt{2}}{2}(\beta + 2\gamma + 2\eta).$$

It is simply to show that

$$\sqrt{(\beta+2\eta)^2+4\gamma^2} \geq \frac{\sqrt{2}}{2}(\beta+2\gamma+2\eta)$$

with equality achieved only if $2\gamma = \beta + 2\eta$.

Focusing on a preamble symbol $a_{k,l}$ with odd l and regardless of the channel and noise, the demodulated symbol $a^{(c)}_{k,l}$ can be obtained from (5.8) by substituting $a_{k+p,l+q}$ with the corresponding preamble symbols defined by (5.31). Without loss of generality, assume $a_{k,l} = 1$ with l odd, then

$$\begin{aligned} a^{(c)}_{k,l} = &\sum_{q=0,p} j^p \cdot j^{p+p\cdot 2l} A^*_g(0, p\nu_0) + x \sum_{q=1,p} j^{2p+q+2p(q+2l)} A^*_g(\tau_0, 2p\nu_0) \\ &+ jx^* \sum_{q=1,p} j^{2p-1+q+(2p-1)(q+2l)} A^*_g(\tau_0, (2p-1)\nu_0) \\ &- x^* \sum_{q=-1,p} j^{2p+q+2p(2l+q)} A^*_g(-\tau_0, 2p\nu_0) \\ &- jx \sum_{q=-1,p} j^{2p-1+q+(2p-1)(2l+q)} A^*_g(-\tau_0, (2p-1)\nu_0) \end{aligned}$$

Apply $l = 2n-1$ and the property of $A_g(\tau,\nu)$ stated in (5.10), we can get

$$\begin{aligned} a^{(c)}_{k,l=2n-1} &= \textstyle\sum_p A_g(0, 2p\nu_0) + (jx + jx^*) \sum_p A_g(\tau_0, 2p\nu_0) \\ &\quad + (x - x^*) \textstyle\sum_p A_g(\tau_0, (2p-1)\nu_0) \\ &= \textstyle\sum_p A_g(0, p\nu_0) + j2 \left[\cos\theta \sum_p A_g(\tau_0, 2p\nu_0) + \sin\theta \sum_p A_g(\tau_0, (2p-1)\nu_0)\right] \end{aligned} \tag{5.33}$$

where the second equality comes from $x = \cos\theta + j\sin\theta$. To find the optimal θ that maximises the power of $a^{(c)}_{k,l=2n-1}$, we take the derivation of $|a^{(c)}_{k,l=2n-1}|^2$ with respect to θ and set it to zero. The resulting solutions are as follows:

$$\tan\theta = \frac{\sum_p A_g(\tau_0, 2p\nu_0)}{\sum_p A_g(\tau_0, (2p-1)\nu_0)} \text{ or } \cot\theta = -\frac{\sum_p A_g(\tau_0, 2p\nu_0)}{\sum_p A_g(\tau_0, (2p-1)\nu_0)}$$

Therefore, for the power of $a^{(c)}_{k,l=2n-1}$, we have

$$\begin{aligned} |a^{(c)}_{k,l=2n-1}|^2 \leq &\left(\sum_p A_g(0, p\nu_0)\right)^2 + 4\left(\sum_p A_g(\tau_0, 2p\nu_0)\right)^2 \\ &+4\left(\sum_p A_g(\tau_0, (2p-1)\nu_0)\right)^2 \end{aligned} \tag{5.34}$$

where the equality achieves when

$$\theta = \operatorname{atan}\frac{\sum_p A_g(\tau_0, 2p\nu_0)}{\sum_p A_g(\tau_0, (2p-1)\nu_0)} = \operatorname{atan}\frac{2\sum_{p=1}^{N/4} A_g(\tau_0, (2p-1)\nu_0)}{A_g(\tau_0, 0) + 2\sum_{p=1}^{N/4} A_g(\tau_0, 2p\nu_0)}$$

$$\text{or} \qquad \theta = \operatorname{acot}\frac{\sum_p A_g(\tau_0, 2p\nu_0)}{\sum_p A_g(\tau_0, (2p-1)\nu_0)} + \pi \tag{5.35}$$

It is obvious that (5.29) is therefore just a special case of (5.35) with only one item taken into account in the summation.

Following the same procedure, it is easy to verify that the same result in (5.34) and (5.35) will also hold for even l, which finishes our derivation.

Chapter 6

Conclusions and Future Work

6.1 Conclusions

In this thesis, we investigated the pulse shape adaptation and channel estimation methods in GFDM systems over doubly dispersive channels for future wireless communication applications. General frameworks for pulse shape adaptation and channel estimation preamble design were proposed and verified in the context of OFDM/OQAM systems. Simulation results indicated that a potential gain could be achieved by using the frameworks for system design and analysis.

We began our investigation with a comparative study of OFDM and GFDM systems with state-of-the-are technologies. Various TFL functions and parameters were introduced to ease the task of system analysis. Many prototype functions, including half-cosine, RRC, Gaussian, EGF, TFL1, etc., were discussed and analyzed by TFL functions and parameters. The special property of the EGF functions was derived and shown to be a good candidate for pulse shape adaptation.

A framework for pulse shape optimisation over doubly dispersive channels was proposed targeting at maximisation the desired signal energy or minimising the combined ISI/ICI. A practical adaptation strategy with focus on the EGF function was proposed and the trade-off between performance and complexity was also discussed.

The OFDM/OQAM system, which is already adopted by or considered in wireless communications standards, was intensively reviewed and evaluated with different pulse shapes. Efficient implementation methods were proposed and perfectness of reconstruction was investigated. Inspired by previous work, novel preamble based channel estimation methods were proposed for OFDM/OQAM systems with the help of the proposed framework. Under the framework, an optimal pulse shape dependent preamble structure was derived and a suboptimal but pulse shape independent preamble structure was proposed which resulted in the same or similar performance as the optimal one.

6.2 Future work

As stated in Chapter 5, more time and energy efficient preambles are of great interest and importance in wireless communication. For example, a two-symbol long preamble structure might be used for channel estimation, with unknown interference from neighbouring data symbols. This unknown interference will of course degrade the performance to some extent. As long as the interference can be controlled under a certain level, satisfactory performance is still possible to be achieved. How to control the uncertainty of the unknown interference and how to make the decision of channel estimation with presence of the unknown interference is still not clear.

Another important issue needs to be considered is the pulse shape adaptation strategy when the effect of ISI/ICI and channel estimation have to be taken into consideration. It is still not clear how the demodulation power will relate to the pulse shape itself, let alone its relationship with the TFL parameters. Once again the EGF function can be a good starting point.

As shown in [50, 51], filter bank spectral estimator (FBSE) can provide high spectrum estimation accuracy with very large dynamic range and relatively low complexity, and therefore is a very promising candidate for spectrum sensing for cognitive radios. A systematic approach of selecting proper pulse shapes in GFDM system taking into consideration the requirement of minimising joint ISI/ICI as well as efficient channel estimation and spectrum estimation will be of great interest, since it will enable dynamic spectrum access (DSA) in a more efficient way and therefore significantly promote the efficiency of spectrum usage.

Bibliography

[1] Y. Zhao and S.G. Häggman, "Intercarrier Interference Self-Cancellation Scheme for OFDM Mobile Communication Systems," IEEE Transactions on Communications, Jul. 2001.

[2] C. Tepedelenlioglu and R. Challagulla, "Low-Complexity Multipath Diversity Through Fractional Sampling in OFDM," IEEE Transactions on Signal Processing, Nov. 2004.

[3] A. Vahlin and N. Holte, "Optimal finite duration pulse for OFDM," *IEEE Transactions on Communications*, vol. 44, pp. 10–14, Jan. 1996.

[4] R. Haas and J.-C. Belfiore, "A time-frequency well-localized pulse for multiple carrier transmission," *Wireless Personal Communications*, vol. 5, pp. 1–18, Jan. 1997.

[5] M. Alard, C. Roche, and P. Siohan, "A new family of function with a nearly optimal time-frequency localization," *Technical Report of the RNRT Project Modyr*, 1999.

[6] P. Siohan and C. Roche, "Cosine-Modulated Filterbanks Based on Extended Gaussian Function," *IEEE Transactions on Signal Processing*, vol. 48, no. 11, pp. 3052–3061, Nov. 2000.

[7] N.J. Baas and D.P. Taylor, "Pulse shaping for wireless communication over time- or frequency-selective channels", *IEEE Transactions on Communications*, vol 52, pp. 1477–1479, Sep. 2004.

[8] T. Kurt, "Signal Shapes for Multi-Carrier Communication Systems," Ph.D thesis, University of Ottawa, Canada, 2006.

[9] W. Kozek, A.F. Molisch, "Nonorthogonal pulse shapes for multicarrier communications in doubly dispersive channels," *IEEE Journal on Selected Areas in Communications*, vol. 16, no. 8, pp. 1579–1589, Oct. 1998.

[10] D. Schafhuber, G. Matz, and F. Hlawatsch, "Pulse-shaping OFDM/BFDM systems for time-varying channels: ISI/ICI analysis, optimal pulse design,

and efficient implementation," in Proc. of *IEEE International Symposium on Personal, Indoor and Mobile Radion Communications*, Lisbon, Portugal, Sep. 2002, pp. 1012–1016.

[11] P. Schniter, "On the design of non-(bi)orthogonal pulse-shaped FDM for doubly-dispersive channels," in Proc. of *IEEE International Conference on Acoustics, Speech, and Signal Processing (ICASSP)*, Montreal, Quebec, Canada, May 2004, vol. 3, pp. 817–820.

[12] B. le Floch, M. Alard and C. Berrou, "Coded Orthogonal Frequency Division Multiplex," *Proceedings of the IEEE*, vol. 83, pp. 982–996, June 1995.

[13] H. Bölcskei, P. Duhamel, and R. Hleiss, "Design of pulse shaping OFDM/OQAM systems for high data-rate transmission over wireless channels," in Proc. of *IEEE International Conference on Communications (ICC)*, Vancouver, BC, Canada, June 1999, vol. 1, pp. 559–564.

[14] T. Strohmer and S. Beaver, "Optimal OFDM Design for Time-Frequency Dispersive Channels," *IEEE Transactions on Communications*, vol. 51, pp. 1111–1123, Jul. 2003.

[15] F.-M. Han and X.-D. Zhang, "Hexagonal Multicarrier Modulation: A Robust Transmission Scheme for Time-Frequency Dispersive Channels," IEEE Transactions on Signal Processing, 2007.

[16] E. Dahlman, S. Parkvall, J. Sköld and P. Beming, *3G Evolution: HSPA and LTE for Mobile Broadband*, Academic Press, 2007.

[17] H. Arslan (Ed.), *Cognitive Radio, Software Defined Radio, and Adaptive Wireless Systems*, Springer, 2007.

[18] S. Signell and J.L. Huang, "A Matlab/Octave Simulation Workbench for Multi-Antenna Software Defined Radio", in Proc. of *24th Norchip Conference*, Linköping, Sweden, November 2006, pp. 145–148.

[19] S. Signell and J. Huang. "A Simulation Environment for Multi-Antenna Software Defined Radio", ICICS 2007, December 2007, Singapore.

[20] P.A. Bello, "Characterization of randomly time-variant linear channels," *IEEE Transactions on Communication Systems*, vol. 11, pp. 360–393, Dec. 1963.

[21] P. Hoeher, "A Statistical Discrete-Time Model for the WSSUS Multipath Channel," *IEEE Transactions on Vehicular Technology*, vol. 41, no. 4, pp. 461–468, Nov. 1992.

[22] L. Ahlin, J. Zander and B. Slimane, *Principles of Wireless Communications* Studentlitteratur, 2006.

[23] J.G. Proakis, *Digital Communications*, fourth edition, McGram-Hill, 2000.

[24] S. Mallat, *A Wavelet Tour of Signal Processing, Second Edition*, Academic Press, 1999.

[25] R. W. Chang, "Synthesis of Band-Limited Orthogonal Signals for Multi-carrier Data Transmission," *Bell System Technical Journal*, vol. 45, pp. 1775–1796, Dec. 1966.

[26] B.R. Saltzberg, "Performance of an efficient parallel data transmission system", *IEEE Transactions on Communications Technology*, vol. 15, no. 6, pp. 805–811, Dec. 1967.

[27] S.B. Weinstein and P.M. Ebert, "Data transmission by frequency division multiplexing using the discrete Fourier transform", *IEEE Transactions on Communications Technology*, vol. COM-19, no. 5, pp. 628-634, Oct. 1971.

[28] A. Peled and A. Ruiz, "Frequency domain data transmission using reduced computational complexity algorithms", in Proc. of *IEEE International Conference on Acoustics, Speech, and Signal Processing (ICASSP)*, vol. 5, pp. 964–967, Apr. 1980.

[29] P. Siohan and C. Roche, "Derivation of Extended Gaussian Functions Based on the Zak Transform," *IEEE Signal Processing Letters*, vol. 11, no. 3, pp. 401–403, Mar. 2004.

[30] P. Siohan, C. Siclet and N. Lacaille, "Analysis and design of OFDM/OQAM systems based on filterbank theory," *IEEE Transactions on Signal Processing*, vol. 50, no. 5, pp. 1170–1183, May 2002.

[31] D. Pinchon, P. Siohan and C. Siclet, "Design Techniques for Orthogonal Modulated Filterbanks Based on a Compact Representation," *IEEE Transactions on Signal Processing*, vol. 52, no. 6, pp. 1682–1692, Jun. 2004.

[32] P.P. Vaidyanathan, *Multirate Systems and Filter Banks*, Prentice-Hall Press, 1993.

[33] L. Råde and B. Westergren, *Mathematics Handbook for Science and Engineering*, Studentlitteratur, 2004.

[34] G. Matz, D. Schafhuber, K. Gröchenig, M. Hartmann, and F. Hlawatsch, "Analysis, optimization, and implementation of low-interference wireless multicarrier systems," *IEEE Transactions on Wireless Communications*, vol. 6, no. 5, pp. 1921–1931, May 2007.

[35] P. Jung, "Weighted Norms of Ambiguity functions and Wigner Distributions," in Proc. of *IEEE International Symposium on Information Theory (ISIT)*, Seattle, USA, July 2006, pp. 1519–1523.

[36] TIA Committee TR-8.5, "Wideband Air Interface Isotropic Orthogonal Transform Algorithm (IOTA) –Public Safety Wideband Data Standards Project – Digital Radio Technical Standards," TIA-902.BBAB (Physical Layer Specification, Mar. 2003) and TIA-902.BBAD (Radio Channel Coding (CHC) Specification, Aug. 2003) http://www.tiaonline.org/standards/

[37] M. Bellec and P. Pirat, "OQAM performances and complexity," *IEEE P802.22 Wireless Regional Area Network (WRAN)*, Jan. 2006. http://www.ieee802.org/22/Meeting_documents/2006_Jan/22-06-0018-01-0000_OQAM_performances_and_complexity.ppt

[38] H. Bölcskei, "Orthogonal Frequency Division Multiplexing Based on Offset-QAM", *Advances in Gabor Analysis*, Birkhäuser, 2003.

[39] L. Vangelista and N. Laurenti, "Efficient Implementations and Alternative Architectures for OFDM-OQAM Systems," *IEEE Transactions on Communications*, vol. 49, no. 4, pp. 664–675, Apr. 2001.

[40] B. Hirosaki, "An Orthogonally Multiplexed QAM System Using the Discrete Fourier Transform", *IEEE Transactions on Communications*, vol. 29, no. 7, pp. 982–989, Jul. 1981.

[41] T. Pollet, M. van Bladel, and M. Moeneclaey, "BER Sensitivity of OFDM Systems to Carrier Frequency Offset and Wiener Phase Noise," *IEEE Transactions on Communications*, vol. 43, no. 2/3/4, pp. 191–193, Apr. 1995.

[42] P. Jung, G. Wunder and C. S. Wang, "OQAM/IOTA Downlink Air Interface for UMTS HSDPA Evolution," in Proc. of *9th International OFDM-Workshop*, Hamburg, pp. 153–157, 2004.

[43] H. Bölcskei, P. Duhamel, and R. Hleiss, "A subspace-based approach to blind channel identification in pulse shaping OFDM/OQAM systems," *IEEE Transactions on Signal Processing*, vol. 49, no. 7, pp. 1594–1598, Jul. 2001.

[44] J.P. Javaudin, D. Lacroix and A. Rouxel, "Pilot-aided channel estimation for OFDM/OQAM," in Proc. of *VTC'03 Spring*, pp. 1581–1585, Apr. 2003.

[45] S.W. Kang and K.H. Chang, "A novel channel estimation scheme for OFDM/OQAM-IOTA system," *ETRI Journal*, vol. 29, pp. 430–436, Aug. 2007.

[46] D. Lacroix and J.P. Javaudin, "A new channel estimation method for OFDM/OQAM," in Proc. of *7th International OFDM-Workshop*, Hamburg, Sep. 2002.

[47] C. Lélé, J.P. Javaudin, R. Legouable, A. Skrzypczak and P. Siohan, "Channel estimation methods for preamble-based OFDM/OQAM modulations," in Proc. of *European Wireless Conference*, Paris, France, Apr. 2007.

[48] C. Lélé, P. Siohan, R. Legouable and J.P. Javaudin, "Preamble-based channel estimation techniques for OFDM/OQAM over the powerline," in Proc. of *IEEE International Symposium on Power Line Communications and its Applications (ISPLC)*, Pisa, Italy Mar. 2007.

[49] C. Lélé, P. Siohan and R. Legouable, "2 dB better than CP-OFDM with OFDM/OQAM for preamble-based channel estimation," in Proc. of *IEEE International Communication Conference (ICC)*, Beijing, China, Apr. 2008.

[50] B. Farhang-Boroujeny and R. Kempter, "Multicarrier Communication Techniques for Spectrum Sensing and Communication in Cognitive Radios," *IEEE Communications Magazine*, pp. 80–85, Apr. 2008.

[51] B. Farhang-Boroujeny, "Filter Bank Spectrum Sensing for Cognitive Radios," *IEEE Transactions on Signal Processing*, vol. 56, no. 5, pp. 1801–1811, May 2008.